Title
Biophysical Investigation of Kinesin-based Transport In Vitro

Author
Li, Qiaochu

Publication Date
2018

Peer reviewed|Thesis/dissertation

UNIVERSITY OF CALIFORNIA, MERCED

Biophysical Investigation of Kinesin-based Transport In Vitro

A dissertation submitted in partial satisfaction of the requirements
for the degree Doctor of Philosophy

in

Physics

by

Qiaochu Li

Committee in charge:

Professor Jay E. Sharping, Chair
Professor Ajay Gopinathan
Professor Jing Xu, Advisor

2018

The Dissertation of Qiaochu Li is approved, and it is acceptable in quality and form for publication on microfilm and electronically:

Professor Ajay Gopinathan Date

Professor Jing Xu Date

Professor Jay Sharping, Chair Date

University of California, Merced

2018

Table of Contents

Lists of Figures

Acknowledgments

First and foremost, I would like to express my most sincere appreciation and gratitude to my advisor professor Jing Xu. She has not only the attitude and the substance of a genius, but also the patience to teach and guide anyone who is willing to learn. Without her help and guidance, this thesis would not have been possible. I would also like to express my sincere gratitude to my thesis committee members: professor Jay Sharping and professor Ajay Gopinathan for their insightful comments and suggestions.

I would also like to express my gratitude to my colleagues, Joseph Lopes, Amanda Tan for their willingness to help me whenever I need assistance. I would like to thank John Wilson in the Xu lab for help with microtubule length analysis using FIESTA for one of my project.

I would also like to thank my parents and my wife Erica. I am particularly proud because I am a first-generation college in my family and I am the first person in my family to reach this level of scholastic achievement. I am truly lucky to have such a supportive and loving family.

Curriculum Vitae

Education

University of California, Merced	PhD, Physics	2014-2018
California State University, Chico	MBA, College of Business	2011-2013
Beijing U of Posts and Telecom.	BS, Physics	2007-2011

Research Experience

Research assistant	Advisor: Prof. Jing Xu	Physics, UC Merced	Spring 2014-
Research assistant	Advisor: Prof. Anna Mayor	Physics, CSU Chico	2011-2013
Research assistant	Advisor: Prof. Hujiang Yang	Physics, BUPT	2010-2011

Publications

1. Q. Li, M. Vershinin, S.J. King, J. Xu. "**Cholesterol influences the effect of tau on membrane-coupled kinesins**", in preparation.
2. Q. Li, K.F. Tseng, S.J. King, W.H. Qiu, J. Xu. "**A fluid membrane enhances the velocity of cargo transport by small teams of kinesin-1**", *The Journal of Chemical Physics*, 148, 123318 (2018)
3. Q. Li, S.J. King, J. Xu. "**Native kinesin-1 does not preferentially bind to GTP-rich microtubules in vitro**", *Cytoskeleton,* 74, 356 (2017)
4. Q. Li, S.J. King, A. Gopinathan, J. Xu. "**Quantitative Determination of the Probability of Multiple-Motor Transport in Bead-Based Assays**", *Biophysical Journal,* 111, 2720 (2016)
5. W. Liang, Q. Li, K.M. Faysal, S.J. King, A. Gopinathan, J. Xu. "**Impact of Microtubule Defect on Kinesin-Based Transport**", *Biophysical Journal,* 110, 2229 *(2016)*
6. S. Gimbal, Q. Li, A. Petrova-Mayor. "**Polarization Effects Induced by A Two-Mirror Lidar Beam Steering Unit**", *Proceedings of the 26th International Laser Radar Conference, 1, 81* (2012)
7. S. Gimbal, Q. Li, A. Petrova-Mayor. "**Polarization Effects Induced by A Two-Mirror Laser Beam Scanner**", *Proceedings of SPIE Remote Sensing System Engineering, Section IV, 85160F* (2012)

Presentations

Biophysical Society Annual Meeting	2016-2017

The American Society for Cell Biology Annual Meeting	2015-2017
CCBM External Advisory Board Meeting	2017
CCBM Open House	2017
American Physics Society Far West Section	2016
UC Merced QSB Graduate Recruiting Weekend	2016
UC Merced Physics Annual Research event	2015
Conference on Lasers and Electro-Optics	2012
26th International Laser Radar Conference	2012
SPIE Remote Sensing Conference	2012

Fellowships, Awards, and Honors

CCBM Fellowship	NSF CREST Center, UC Merced	Summer 2017
CCBM scholar	NSF CREST Center, UC Merced	2016-2017
Physics Travel Award	Physics, UC Merced	Fall 2016
Physics Travel Award	Physics, UC Merced	Spring 2016
Physics Travel Award	Physics, UC Merced	Fall 2015

Professional Membership

Biophysical Society	2016-2017
American Society for Cell Biology	2015-2017
Society of Photo-Optical Instrumentation Engineers	2011-2013
Optical Society of America	2011-2013

Abstract

Biophysical Investigation of Kinesin-based Transport
In Vitro

by

Qiaochu Li

Doctor of Philosophy in Physics

University of California, Merced

Jay Sharping, Chair

Dynamical spatial organization in living cells provides the framework underlying the fundamental genetic and biochemical processes essential to biological life. Importantly, dysfunctions in this process are linked to diseases including neurodegeneration. The dynamic spatial organization cannot be accomplished by passive diffusion alone. Instead, Nature employs molecular motors that are protein machines to actively shuttle materials along biopolymer-based molecular "roads" in cells. Significant advances in single- molecule biophysics have revealed a great deal about how motors function individually in minimal, cell-free environments. Building on these important previous advances, my thesis study aimed at dissecting the physical principles of transport under complex conditions such as those that occur in living cells. With this goal in mind, I tackled three distinct aspects of intracellular transport that are not being considered in single-motor investigations: the number of motors involved (Chapter 2), the condition of the molecular highways that the motors step along (Chapters 3-4), and the physical properties of the lipid membrane that couple the motors to their cargo (Chapters 5-6). My studies to-date have revealed exciting new biophysical mechanisms for potentially correcting the aberrant motor transport that underlies several human pathologies, and established a new, biologically-relevant framework to drive future developments in molecular-motor theory and experiments in cell-free studies.

Chapter 1. Introduction

1A. Background

1A-i. The open problem of transport control in cells

Molecular motors are a class of protein machines that is fundamental to life [1], dysfunctions are linked to diseases including neurodegeneragtion [2, 3]. All cells that are large enough to contain a nucleolus must rely on molecular motors to transport cellular materials across its spatial extent. Molecular motors accomplish this long-range transport process by actively stepping along their biopolymer tracks, with each step fueled by breaking of covalent bonds in the chemical compound adenosine tri-phosphate (ATP) [4].

The range of molecular-motor-based transport is remarkable, with the length scale of cargo delivery spanning over five orders of magnitudes across different cell types (Fig. 1.1). How molecular motors can accomplish such a demanding task remains an important

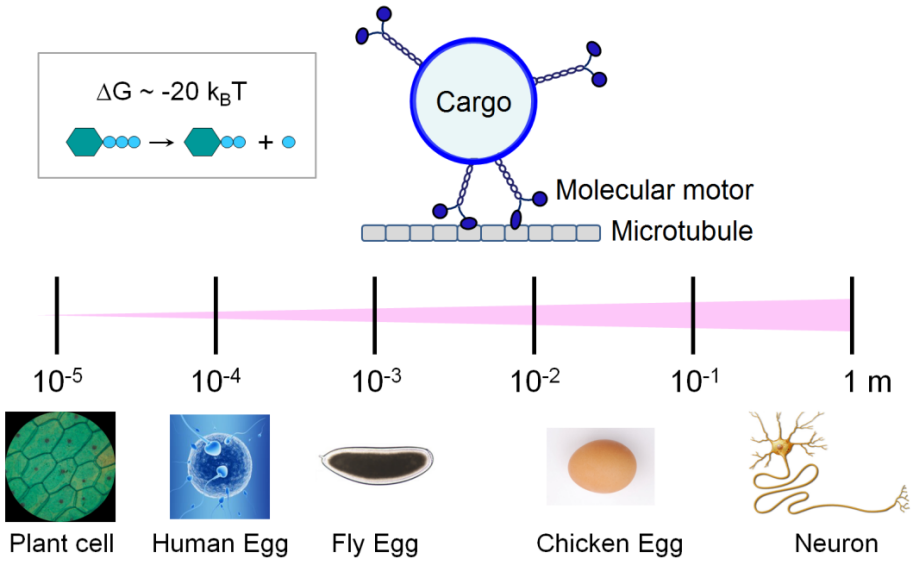

FIGURE 1.1. Overview of my thesis study. Molecular motors are protein machines that convert chemical energies into mechanical motions along their biopolymer tracks. My thesis research seeks to understand an important open question in biology: How do molecular motors accomplish cargo transport across

different length scales? To address this open question, I worked to build up the complexity of our cell-free studies to include considerations of new, biologically relevant factors that are likely to impact cargo transport in live cells.

and open question in biology. Mechanistic understanding is important for hijacking the molecular motors for active, long-range delivery of synthetic cargos (containing genetic or therapeutics materials).

The goal of my thesis is to identify and understand control parameters for key biophysical function of cargo transport: the distance the cargo can travel. My central hypothesis is that the collective function of a small team of motors transporting the same cargo is highly sensitive to biologically relevant factors that are absent in traditional cell-free studies. I focused my thesis studies on the main microtubule-based motor, kinesin-1. The single-molecule functions of kinesin is well-characterized and well-defined [1, 4-7], making it an ideal model motor protein to study their collective function. I examined two key biologically relevant factors: the "roads" condition of the microtubule track and the physical property of their cargo membrane.

1A-ii. Single-beam gradient force optical trap

I used optical trap to characterize cargo transport by kinesin-1 motors (Fig. 1.2). Optical trap has been instrumental in elucidating the biophysical functions of molecular motors including kinesin, and particularly at the single molecule level [5, 6, 8]. The field of laser-based optical trapping was pioneered by Arthur Ashkin in 1970s [9-11], pioneered by Steven Chu for trapping neutral atoms in 1980s [12-14], and pioneered by Steven Block for single-molecule biophysical measurements in 1990s [5, 6, 8, 15]. In my thesis study, I carried out optical trapping studies both to reproduce previous findings in the single-molecule regime and to examine new control parameters in the collective transport regime that was my thesis focus.

The single-beam gradient force optical trap refers to a tightly focused laser spot light formed by an objective lens of high numerical aperture (1.49 used in the Xu lab). The fundamental TEM_{00} or Gaussian mode is used for most optical trapping operations (such as that in the Xu lab), although the more sophisticated TEM_{01}** mode or Laguerre-Gaussian beam has also been used to minimize scattering force along the optical propagation axis in the single-beam optical trap [16, 17]. The wavelength of the trapping laser is chosen as 980 nm in the Xu lab due to its comparative transparency [10] and limited photodamage to biological material [18].

The optical trap acts as a three-dimensional Hookean spring that exert restoring force on a dielectric particle positioned at its focus; the characteristic spring constant of the optical trap is proportional to, and thus tunable by, the intensity of the trapping light. The dielectric particle near the trap focus experiences a force due to the transfer of

momentum from the scattering of incident photons [19]. For a dielectric bead with higher index of refraction than its surrounding media, the net force imparted to the particle points toward the trap center (1.55 for polystyrene or glass vs. 1.33 for water used in my thesis study). In my thesis study, I used polystyrene/glass beads as cell-free cargos for the motor, and spatially manipulated the spatial locations of these motor-decorated cargos in optical-trapping experiments (Fig. 1.2 *B*). Because the presence of molecular motors does not significantly alter the geometry or the dielectric property of the polystyrene/glass beads, I was able to directly apply optical trapping to study cargo transport by a small team of kinesins.

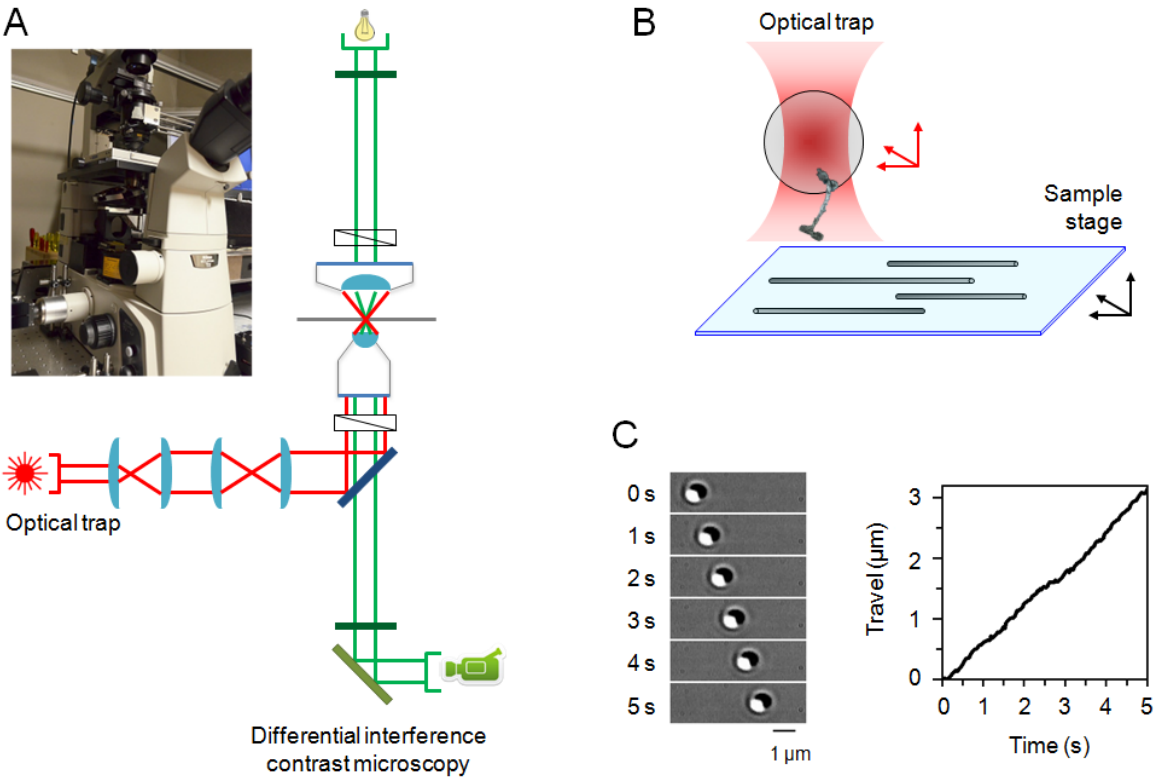

FIGURE 1.2. Optical trap-based measurements of cargo transport used in my thesis study. (*A*) Schematic of a custom-built single-beam optical trap setup in the Xu lab. Differential interference contrast (DIC) microscopy enables real-time imaging of microtubules below optical resolution limit. A near-infrared laser (980 nm) is aligned with the optical train of the microscope to create a tightly focused light spot in the sample plane. Inset, a photo of our setup. (*B*) Illustration of the local confinement of a kinesin-based cargo by the optical trap. The position of the optical trap and the sample stage is manually controlled to reduce the interaction distance between the cargo-associated motor and its microtubule

track. (*C*) Representative DIC-based video recording of a kinesin-based cargo (left) and particle-tracked trajectory (right).

1B. Overview of my thesis study

Single-molecule biophysical studies utilizing optical trapping [5, 6, 19] have uncovered a great deal about the function of individual kinesins in minimal cell-free systems, empowering investigations into the roles of physiologically relevant factors in kinesin-based transport. However, motor proteins do not typically work in isolation in living cells. To model this important biological scenario, my thesis study has focused on understanding key factors that impact cargo transport by a small team of kinesin-1 motors. Fundamental understanding of these factors is necessary for developing future strategies to combat transport malfunctions in cells and to improve human health.

1B-i. Quantitative determination of motor number

I first developed a quantitative guide to understanding the probability of multiple-motor events in standard cell-free studies (detailed in Chapter 2). This is the first of the five projects I carried out during my thesis study in the Xu lab. My efforts here produced one first-author peer-reviewed publication in the *Biophysical Journal* [20] and four poster presentations at society meetings.

A key experimental challenge in bead-based assays is that the number of motors on a bead is not well defined. Particularly for single-molecule investigations, the probability of single- versus multiple-motor events has not been experimentally investigated. This is a difficult task, because molecular motors are significantly below the optical-resolution limit for visual quantifications, their longest dimension is typically shorter than 100 nm. Despite substantial advances in fluorescence-based imaging methodologies, labeling with beads remains critical for optical trapping-based investigations of molecular motors.

I used bead travel distance as an indicator of multiple-motor transport and determined the lower-bound probability of bead transport by two or more motors. I limited the ATP concentration in order to increase our detection sensitivity for multiple- versus single-kinesin transport. Surprisingly, for all but the lowest motor number examined, my measurements exceeded estimations of a previous model by two or more fold. To bridge this apparent gap between theory and experiment and together with our theoretical collaborator Dr. Ajay Gopinathan, we derived a closed-form expression for the probability of bead transport by multiple motors and constrained the only free parameter in this model using our experimental measurements.

Our data indicate that kinesin extends to ~57 nm during bead transport, suggesting that kinesin exploits its conformational flexibility to interact with microtubules at highly curved interfaces such as those present for vesicle transport in cells. To our knowledge, our findings provide the first experimentally constrained guide for the probability of multiple-motor transport in optical trapping studies.

1B-ii. Effect of microtubule structural defect on kinesin-based transport

I next joined a study where we examined the impact of microtubule defects on kinesin-based transport (detailed in Chapter 3). This is the second of the five projects I carried out during my thesis study in the Xu lab. It was led by my advisor Jing Xu and an undergraduate research student Winnie Liang, my main role was to help carrying out revision experiments suggested during the manuscript review process. My efforts here produced one co-author peer-reviewed publication in the *Biophysical Journal* [21].

Microtubules are protein polymers that form “molecular highways” for long-range transport within living cells. Molecular motors actively step along microtubules to shuttle cellular materials between the nucleus and the cell periphery; this transport is critical for the survival and health of all eukaryotic cells. Structural defects in microtubules exist, but whether these defects impact molecular-motor based transport remains unknown. To address this challenge, we developed a modified optical trapping assay to repeatedly sample a single microtubule segment, thereby inferring the presence of a defect based on the functional readout of cargo motility.

We found that microtubule defects influence kinesin-based transport in vitro. The effects depend on motor number: cargos driven by a few motors tended to unbind prematurely from the microtubule, whereas cargos driven by more motors tended to pause. The trajectories of cargos during pausing reflected force-based interactions between paused and moving motors. Our data further demonstrate that the probability of pausing in the many-kinesin system is directly tuned by the frequency of microtubule defects. To our knowledge, our study provides the first direct link between microtubule defects and kinesin function. The effects uncovered in our study may have physiological relevance in vivo.

1B-iii. Effect of microtubule biochemical state on kinesin-based transport

I next examined the potential regulatory role of a particular biochemical state of the microtubule, the nucleotide state of its tubulin subunits, on kinesin-based transport (detailed in Chapter 4). This is the third of the five projects I carried out during my thesis

study in the Xu lab. My efforts here produced one first-author peer-reviewed publication in the *Cytoskeleton* [22] and two poster presentations at society meetings.

Molecular motors such as kinesin-1 work in small teams to actively shuttle cargos in cells, for example in polarized transport in axons. Excitingly, previous studies have reported that single kinesin has a 3-fold higher binding affinity for microtubules in one type of nucleotide state (rich in GTP-tubulin) than another type of nucleotide state (rich in GDP-tubulin). Because the motor's binding rate is a key parameter for multiple-motor transport, we hypothesized that, with increasing motor number, cargo run length will grow faster on GTP-rich-microtubules, where the motor's binding affinity is higher, than on GDP-microtubules, where the motor's binding affinity is lower. Such regulation may further contribute to polarized transport in axons. To test this hypothesis, I carried out optical trapping experiments to quantify kinesin-based run length between GTP-rich microtubule and GDP-microtubules.

Surprisingly, I did not uncover any significant differences in run length between microtubule types. Comparison with previous theory and additional biochemical experiments further revealed that native kinesin-1 does not bind preferentially to GTP-rich microtubules. We note that, the apparent discrepancy between our observations and the previous report likely reflects differences in post-translational modifications between the native motors used here and the recombinant motors examined previously. Future investigations will help shed light on the interplay between the motor's post-translational modification and the microtubule's nucleotide-binding state for transport regulation in vivo.

1B-iv. Effect of a fluid cargo membrane on kinesin-based transport

I next examined the impact of a fluid membrane on cargo transport by a small team of kinesin-1 motors (detailed in Chapter 5). This is the fourth of the five projects I carried out during my thesis study in the Xu lab. This work corresponds to Aim 1a in my advancement proposal. My efforts here produced one first-author peer-reviewed publication in the *Journal of Chemical Physics* [23] and two poster presentations at society meetings.

While the single-molecule functions of kinesin are well characterized, the physiologically relevant transport of membranous cargos by small teams of kinesins remains poorly understood. A key experimental challenge remains in the quantitative control of the number of motors driving transport. I used my quantitative guide for motor number [24] to overcome this challenge, and experimentally accessed transport by a single kinesin through the physiologically relevant transport by a small team of kinesins. I used a fluid lipid bilayer to model the cellular membrane in vitro, and employed optical trapping to quantify transport of membrane-enclosed cargos versus traditional membrane-free cargos under otherwise identical conditions.

I found that coupling motors via a fluid membrane significantly enhances the velocity of cargo transport by small teams of kinesins. Importantly, enclosing a cargo in a fluid lipid membrane did not impact single-kinesin transport, indicating that membrane-dependent velocity enhancement for team-based transport arises from altered interactions between kinesins. The increased velocity of membrane-enclosed cargos supports a model in which a lipid membrane delays force-based interactions between kinesins, allowing this cargo to tumble forward to a further location than a membrane-free cargo. Our study highlights the fluid cargo membrane as an important determinant of the fundamental biological process of transport by a group of kinesins. An enhanced velocity is likely important for the timely delivery of cargos in cells.

1B-v. Effect of membrane cholesterol on kinesin-based transport

I next built up the complexity of my membrane-enclosed cargos [23] examined the impact of membrane composition on kinesin-based transport (detailed in Chapter 6). This is the fifth of the five projects I carried out during my thesis study in the Xu lab. This work corresponds to Aim 1c and Aim 2 in my advancement proposal. My efforts here produced one manuscript in preparation [25].

Recent studies report an intriguing correlation between the motility of the cellular cargo "phagosome" and its membrane cholesterol. Phagosomal motility is initially bidirectional, but switches to minus-ended motion upon maturation; a significant, two-fold increase in membrane cholesterol is associated with this motility switch. Because plus-ended motion is driven by kinesins, we hypothesized that membrane cholesterol impairs kinesin-based transport. To test his hypothesis, I used a fluid, DOPC-based lipid membrane to model the cellular membrane without cholesterol, and I tuned membrane cholesterol to range between 0-50%. To mimic the crowded “road” conditions along microtubules in cells, I also used tau as our model microtubule-associated protein.

Our data demonstrate that, in the absence of tau, membrane cholesterol did not significantly alter the probability of cargo binding to microtubules. In contrast, in the presence of tau (1:5.5 tau:tubulin), coupling via a fluid membrane significantly promoted cargo binding to the microtubule; this effect was countered by membrane cholesterol. Our data suggest that the kinesin’s ability to search and to avoid local roadblocks on the microtubule is strongly determined by the mobility of the motor’s attachment point to the cargo surface; this mobility is impaired with increased membrane cholesterol. Our study highlights an exciting, novel role of the cargo membrane in the regulation of kinesin-based transport.

Chapter 2. Quantitative Determination of Motor Number [26]

2A. Introduction

Optical trapping, the research tool in the Xu lab, has been instrumental in elucidating the mechanochemical functions of molecular motors, particularly at the single-molecule level [5, 6, 8]. Perhaps paradoxically, the single-molecule range in optical trapping experiments has yet to be defined in quantitative terms.

Uncertainty arises because optical trapping studies use dielectric beads to label molecular motors. Each bead is typically decorated by a Poisson-distributed number of motors, rather than by a well-defined number of motors. The three-dimensional nature of the bead further complicates the problem, since not all motors on the bead can reach the microtubule at the same time. While a reduction in the ratio of motors to beads can lower the probability of cargo transport by two or more motors, this reduction also limits the fraction of motor/bead complexes capable of interacting with the microtubule and in turn significantly reduces experimental throughput. Although force measurements can shed light on the number of motors engaged in transport, work by Furuta et al. [27] revealed that, depending on motor type, the force generated by multiple motors is not necessarily sensitive to motor number. Previously, Beeg et al. [28] determined the average number of simultaneously engaged motors on a bead for a range of motor concentrations, making it possible to evaluate the probability of multiple-motor events measured under the same experimental conditions. However, Beeg et al. [28] used a bead size (100 nm diameter) substantially smaller than that optimized for optical trapping (~500 nm diameter, [8]). Because a 5-fold increase in bead size can impact both the density of motors on the bead surface and the fraction of bead surface available to the microtubule, it is non-trivial to translate the experimental conditions from [28] to those suitable for optical trapping.

To date, only one theory model has provided a general guide for estimating the probability of multiple-motor transport at a given motor number in bead-based assays [6]. However, the assumptions of this previous model have not been experimentally verified. Importantly, the motors are assumed to be fully extended and their motor domains effectively in contact with each other (Fig. 2.1 *A*). There is increasing consensus that motors should be able to bind different locations along the length of the microtubule [29, 30] (Fig. 2.1 *B*). However, this updated geometry does not readily lend itself to theory predictions, since there is limited information on a key parameter in this updated geometry (how far the motor can extend during bead transport, Fig. 2.1 *B*). As a result, predictions from the previous model [6] have remained the only guide for estimating the probability of multiple-motor transport in optical trapping studies [31-35].

Here we developed a quantitative guide for understanding the probability of multiple-motor events in the dilute motor range. We focused on experimental details that

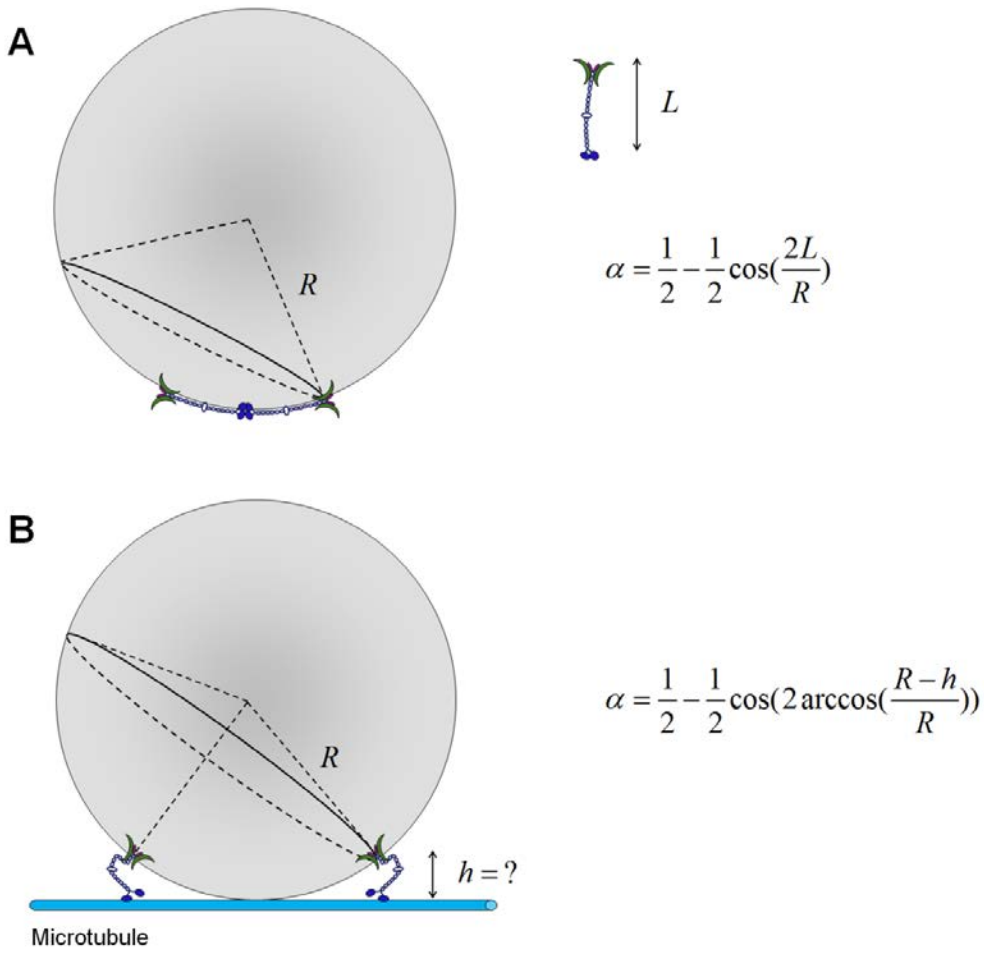

FIGURE 2.1. Geometries for two-motor transport (not to scale) and associated probability that two randomly attached motors are within simultaneous reach of the microtubule (α). Here we considered the condition in which the bead radius (R) is larger than the motor's contour length (L), and the motors are randomly distributed on the bead surface. Under this condition, although all motors on the bead can contribute to bead transport, not all motors can reach the microtubule at the same time. When any one motor on the bead binds the microtubule, there is a limited area surrounding this motor (a spherical cap) in which a second motor may be located and be within reach of the same microtubule. The value of α is determined as the area ratio of this spherical cap to the entire bead surface. (*A*) Geometry for two-motor transport in a previous model [6]. The motors are assumed to be fully extended, and their motor domains effectively in contact with each other. The area of the spherical cap enclosing a second motor available for transport has a radius twice the motor's contour length. R = 250 nm in the current study (and in typical optical trapping studies). This geometry yields α = 0.099 for kinesin (L = 80 nm [36, 37]) and α = 0.039 for dynein (L = 50 nm [38, 39]). (*B*) An updated geometry for two-motor transport [29, 30]. Here, the motors can bind different locations along the length

of the microtubule, and the motors are no longer assumed to be fully extended. The area of the spherical cap enclosing a second motor available for transport is determined by *h*, the extension of the motor during active transport. There is limited information about *h* for flexible motors such as kinesin.

are typically used in optical trapping studies (500 nm diameter spherical beads and randomly distributed motors on the bead surface) and carried out our experiments using the major microtubule-based motor, kinesin-1 (conventional kinesin). We used motile fraction, the probability of beads exhibiting motility along microtubules, as an experimental readout for the average number of active motors on the bead [5, 6]. We used bead travel distance to identify bead transport by multiple kinesins for a range of motile fractions, and used a limiting ATP concentration to increase our detection sensitivity for these multiple-motor events [40-44]. Surprisingly, for all but the lowest motile fractions examined, we detected substantially higher probabilities of multiple-motor transport than that predicted by the previous theory model [6]. We therefore applied both theory and simulation to unravel this discrepancy.

2B. Materials and methods

2B-i. Proteins and reagents

Bovine brain tubulin was purified over a phosphocellulose column as previously described [45]. Conventional kinesin was purified from bovine brain as previously described [46], except that 9S kinesin was eluted from the Mono-Q resin using customized salt gradients to separate kinesin from other polypeptides in the 9S sucrose fractions [47]. Chemicals were purchased from Sigma Aldrich (St. Louis, MO, USA).

2B-ii. Microtubule preparation

To assemble taxol-stabilized microtubules, purified tubulin (40 μM) was supplemented with 0.5 mM GTP and incubated for 20 min at 37 °C. Assembled microtubules were mixed with an equal volume of PM buffer (100 mM PIPES, 1 mM $MgSO_4$, 2 mM EGTA, pH 6.9) supplemented with 40 μM taxol and incubated for 20 min at 37 °C. Microtubules were then kept at room temperature in a dark box and used within four days of preparation.

2B-iii. Motor/bead complex preparation

Kinesin was incubated with carboxylated polystyrene beads (500 nm diameter, Polysciences, Warrington, PA, USA) in motility buffer (67 mM PIPES, 50 mM CH_3CO_2K, 3 mM $MgSO_4$, 1 mM dithiothreitol, 0.84 mM EGTA, 10 μM taxol, pH 6.9) for 10 min at room temperature; this solution was supplemented with an oxygen-scavenging solution (250 μg/mL glucose oxidase, 30 μg/mL catalase, 4.6 mg/mL glucose) and ATP (1 mM or 0.01 mM, as indicated) prior to motility measurements. Bead concentration was kept constant at 3.6×10^5 particles/μL and the concentration of kinesin was varied to give rise to a range of motile fractions (Fig. 2.2).

2B-iv. In vitro optical trapping

Optical trapping was carried out in flow cells, imaged via differential interference microscopy, and video-recorded at 30 Hz as previously described [42]. For all studies here, we limited the trap power to <20 mW (at fiber output), such that the trap positioned individual beads but was not sufficient to stall beads carried by a single kinesin (stall force ~4.5 pN, [48]). To measure motile fraction, we used the optical trap to position individual beads in the vicinity of the microtubule; a motile event was scored if and only if the bead demonstrated directed motion away from the center of the trap. We observed occasional events where the bead appeared to bind (as indicated by reduced Brownian motion of the bead) but did not move processively away from the trap center (data not shown). We did not score these events for our motile fraction measurements, as they constituted neither motile events nor non-motile events. The beads in these events typically detached shortly after we turned off the optical trap, without demonstrating any clear movement along the microtubule (data not shown). For motile beads, upon observation of directed bead motion along the microtubule, we turned off the optical trap in order to enable cargo transport in the absence of external load.

2B-v. Data analysis

Video recordings of bead motion were particle-tracked to 10 nm resolution (1/3 pixel) using a template-matching algorithm as previously described [42, 47]. Travel distance for each bead was determined as the net displacement of the bead along the microtubule axis upon the bead's binding to and then detaching from the microtubule. The distribution of travel distances for each experimental condition (motile fraction and ATP concentration) was fitted to a single-exponential decay [5]. Mean travel distance and the associated standard error of the mean for each distribution were determined from the fitted decay constant and uncertainty, respectively. To account for human reaction time to

manually shut off the optical trap, only trajectories >0.3 μm were used to determine the distribution of travel distances at each motile fraction.

Best-fit of motile fraction measurements to a one-motor Poisson curve was carried out in OriginPro9.1 (OriginLab Corp., Northampton, MA, USA). Least χ^2 fitting was used to constrain our theory model using our experimental measurements, via a custom routine in MatLab (The MathWorks, Inc., Natick, MA, USA).

2B-vi. Simulation

Our simulation randomly distributes a mean number of active motors (*n*) on a 51x51 lattice with periodic boundaries (a torus lattice), identifies the location of a lattice site that is occupied by one motor, and evaluates the number of motors in a closed patch surrounding this particular lattice site. The size of the closed path is determined as the area of the square lattice multiplied by α, the probability that any two randomly distributed motors on the bead are in close enough proximity to be in simultaneous reach of the microtubule. We repeated the simulation 10,000 times to determine the probability of counting two or more motors for each set of *n* and α tested. We evaluated the motile fraction corresponding to each *n* using the relationship $\textit{motile fraction} = 1 - e^{-n}$ (Fig. 2.2 and [5, 6]).

2B-vii. Statistical analysis

Standard errors for binomially distributed data were calculated as $\sqrt{P(1-P)/N}$, where *P* is the measured fraction and *N* is the sample size. We did not observe a substantial difference between this error calculation and that using a 68.3% confidence interval for a binomial distribution (data not shown). In case of a zero-fraction measurement (at motile fraction = 0.2, Fig. 2.3 *B*), the standard error was estimated as the upper level of the 68.3% confidence interval for a binomial distribution.

2C. Results

2C-i. Lower-bound measurements of the probability of multiple-motor transport

We used motile fraction as a direct readout for the average number of active motors on a bead [5, 6] (Fig. 2.2). Motile fraction refers to the probability of beads

exhibiting motility along microtubules. While motile-fraction measurements do not require optical trapping, trap-free readout can be difficult to interpret due to the potential presence of dead motors that lack enzymatic activity but can still bind microtubules. When an optical trap is used to confine individual beads to the vicinity of the microtubule (as we did in the current study), the bead must move against the optical trap to demonstrate directed motion along the microtubule. A dead motor may bind the microtubule, but it cannot exert force to drive bead movement against the optical trap, and thus it cannot contribute to a motile event. The resulting motile fraction measurements are therefore not sensitive to the potential effect of dead motors, providing a direct readout for the average number of active motors on the bead.

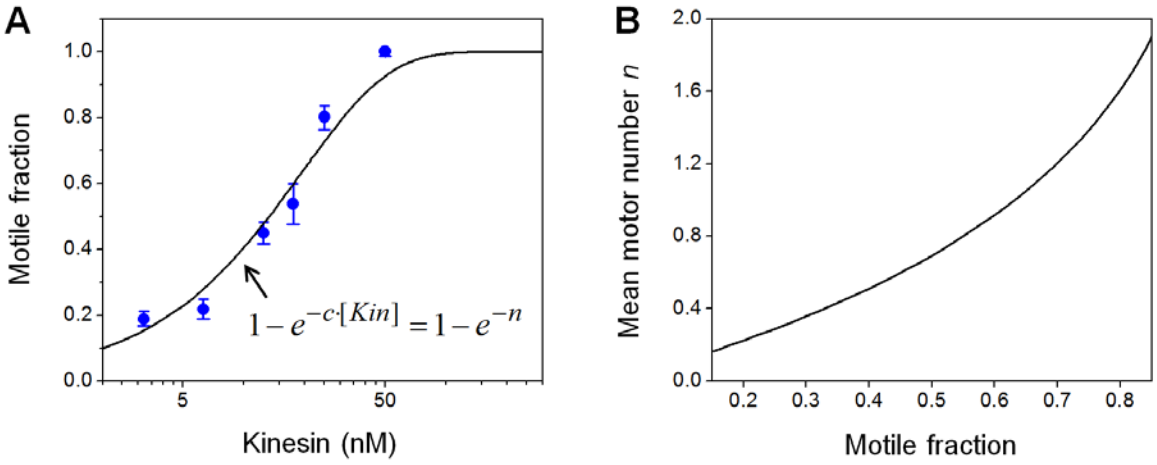

FIGURE 2.2. Motile fraction provides a direct experimental readout for the average number of active motors on the bead (*n*). (*A*) Fraction of beads exhibiting motility along microtubules ("motile fraction") as a function of kinesin motor concentration, measured using an optical trap and at 1 mM ATP. The concentration of beads was kept constant and the concentration of kinesin was varied. Individual beads were confined to the vicinity of microtubules with an optical trap (80-330 beads trapped for each motor concentration). Error bars represent standard error of the mean. Since motile fraction represents the probability that a bead is carried by at least one active motor, it is well described by the single-motor Poisson curve [5, 6] $P(\geq 1)=1-e^{-c\cdot[Kin]}=1-e^{-n}$ (solid line), where *c* represents a fitting parameter and [*Kin*] indicates kinesin concentration. Note that, we carried out our measurements as a function of motile fraction rather than motor concentration ([*Kin*]), because each motile fraction corresponds to a unique *n* value. In contrast, for any particular motor concentration ([*Kin*]), the average number of active motors on a bead (*n*) is not unique and depends sensitively on the concentration of beads used during motor/bead incubation (this

dependence is reflected in the fitting parameter *c*). (*B*) Relationship between *n* and motile fraction using $\textit{motile fraction} = 1 - e^{-n}$ (panel *A* and [5, 6]).

We used bead travel distance to identify multiple-motor events versus single-motor events. The average travel distance for a single kinesin is ~1 μm [5, 49]. When a bead is transported by a single kinesin, there is a <0.1% probability that the travel distance will be >6.9 μm. This is because, when a bead is transported by a single motor, the probability of measuring a travel distance of x μm is described by the single exponential decay $P(x) = e^{-x/d}$, where d is the mean travel distance of a single motor. For the kinesin motor, d = 1 μm [5, 49], and the likelihood that single-kinesin travel persists for less than x_o is $1 - e^{-x_0/d}$. We thus expect that 99.9% of beads transported by a single kinesin travel ≤6.9 μm. Thus, when we observed a motile event longer than our travel threshold, we excluded it from the set of single-motor events with high confidence and identified it as a multiple-motor event. Since not all multiple-motor events exceed this 6.9 μm threshold, our measurements of long-travel events represent lower-bound values for the probability of multiple-motor transport.

We used ATP as an experimental handle to increase the likelihood that a multiple-motor event travels >6.9 μm (blue bars, Fig. 2.3 *A*). Previous studies demonstrated that the distance traveled by multiple kinesins is inversely tuned by ATP concentration (0.01-1 mM) [40-44]. Importantly, the single-kinesin travel distance remains constant over the same ATP range [41, 49]. We thus anticipated that a limiting ATP concentration (0.01 mM) would increase our detection sensitivity for multiple-motor events.

We varied the input kinesin concentration to experimentally access a range of motile fractions (or motor numbers) (Fig. 2.2 *A*). For each motile fraction, we measured 50-150 motile trajectories and determined the corresponding distribution of travel distances (Fig. 2.3 *A*). For both ATP concentrations examined, we found that the fraction of long-travel events increased with increasing motile fraction (blue bars, Fig. 2.3 *A*). At the lowest motile fraction tested (0.2), we did not observe any long-travel events for either ATP concentration. At the highest motile fraction tested (0.8), the fraction of long-travel events was substantially larger than zero for both 0.01 mM and 1 mM ATP. This observation is consistent with the increased presence of motors on the bead for the higher motile fractions (Fig. 2.2 *B*).

Importantly, for the higher motile fractions (>0.2), we observed substantially higher fractions of long-travel events at the lower ATP concentration ($F_{>6.9\mu m}$, Fig. 2.3 *A*). For example, at a motile fraction of 0.8, the fraction of long-travel events was 23% at 0.01 mM ATP, approximately 4-fold larger than the 6% at 1 mM ATP. Since we used the same trap power for measurements at both ATP concentrations, the increase in the fraction of long-travel events was due to the change in ATP concentration, not experiment artifacts from optical trapping. Further, for measurements below our travel

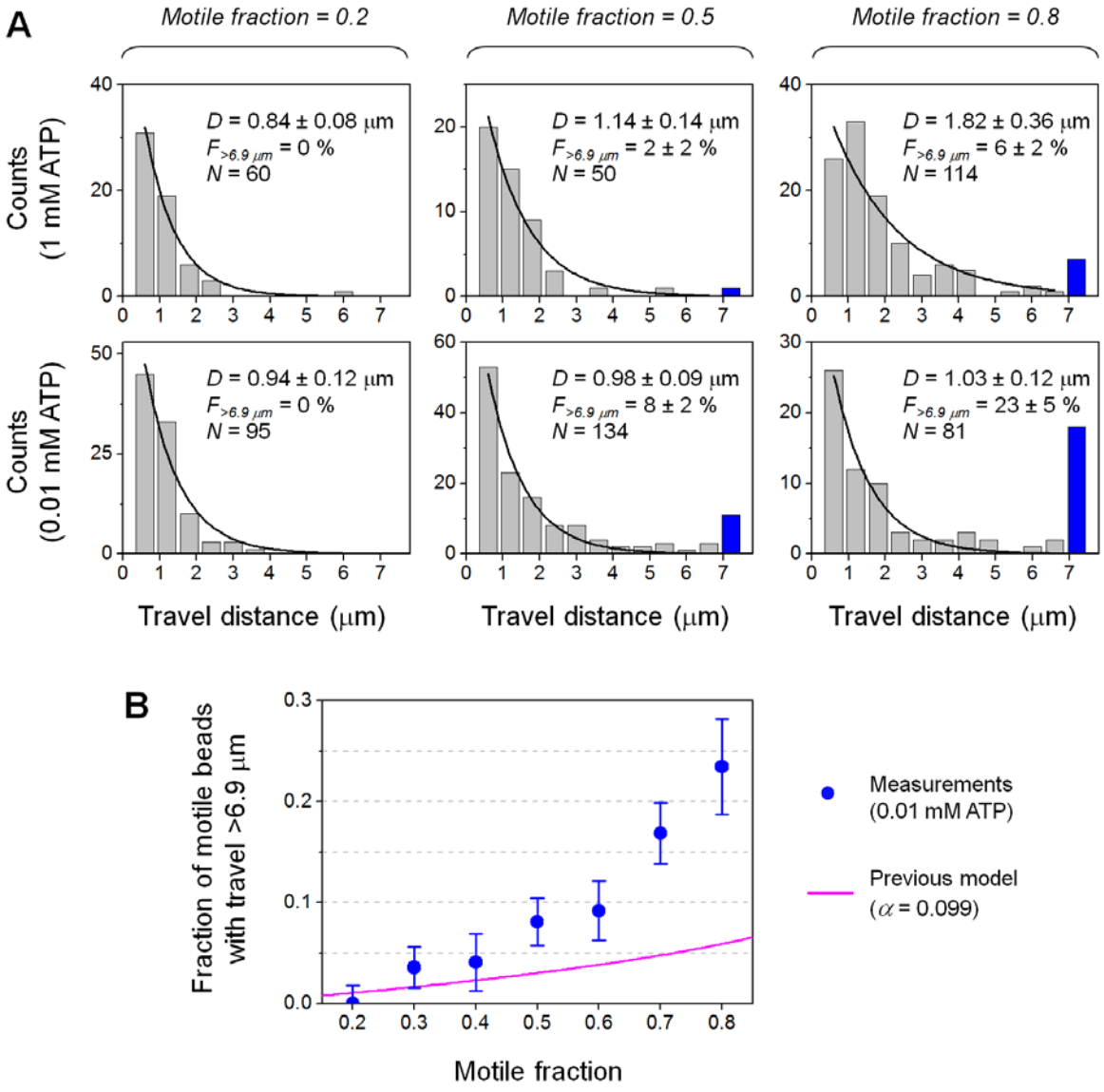

FIGURE 2.3. Measurements of bead travel distances for different motile fractions. (*A*) Distribution of travel distances for three motile fractions measured at 1 mM ATP (top) and 0.01 mM ATP (bottom). Solid line, best fit to a single exponential decay for travel distances ≤6.9 μm. Blue bar, cumulative counts of events with travel distance >6.9 μm. *D* (± standard error), fitted mean travel distance for measurements shorter than our travel threshold. $F_{>6.9\mu m}$ (± standard error), fraction of motile events longer than our travel threshold. *N*, sample size. (*B*) Fraction of motile beads with travel >6.9 μm, measured at 0.01 mM ATP (blue scatter). Error bars, standard error. Magenta line, predicted fraction of motile events transported by two or more motors, based on a previous theory [6].

threshold (grey shading, Fig. 2.3 *A*), the mean travel distances measured at 1 mM ATP approximately doubled as the motile fraction increased from 0.2 to 0.8, while the mean travel distances measured at 0.01 mM ATP remained approximately constant at the single-kinesin level (~1 μm, [5, 49]) over the same motile fraction range. This observation indicates that only the travel distance, but not the likelihood, of multiple-motor events were amplified by the lower ATP concentration. Given the increase in multiple-motor travel distance at 0.01 mM ATP, multiple-motor events are less likely to influence the distribution of travel distances shorter than 6.9 μm. Together, these data demonstrate that our approach of limiting ATP is effective in uncovering the presence of multiple-motor transport in bead-based assays.

We measured the fraction of long-travel events for a range of motile fractions at 0.01 mM ATP (blue scatters, Fig. 2.3 *B*). A previous study [6] modeled the probability that a bead is transported by two or more motors as $P_{previous}(\geq 2) = \alpha \cdot (1 - e^{-n} - ne^{-n})$, where α is the probability that two randomly attached motors on the bead are within simultaneous reach of the microtubule and n is the mean number of active motors available for bead transport. For kinesin, the previous model estimated that α = 0.099, given the bead size employed in this study and in typical optical trapping studies (500 nm diameter) (Fig. 2.1 *A*), or, $P_{previous}(\geq 2) = 0.099 \cdot (1 - e^{-n} - ne^{-n})$. When we recasted the dependence on the mean motor number (n) as that on motile fraction, which we measured experimentally (Fig. 2.2 and [5, 6]), we arrived at the relationship $P_{previous}(\geq 2) = 0.099 \cdot (mf + (1 - mf) \cdot \ln(1 - mf))$, where mf denotes the motile fraction. Note that this probability considers all beads, including those that did not interact with the microtubule. We then normalized $P_{previous}(\geq 2)$ by the associated motile fraction to determine the probability that a motile event is carried out by two or more motors (magenta line, Fig. 2.3 *B* and Fig. 2.6, left). Surprisingly, we detected a substantial difference between these lower-bound measurements and predictions of a previous model [6] (blue scatters vs. magenta line, Fig. 2.3 *B*). For motile fractions >0.4, our lower-bound measurements were substantially larger than predictions from the previous model. For example, at a motile fraction of 0.5, our lower-bound measurements indicate that at least 8% of motile trajectories are transported by multiple motors, more than twice the 3% predicted previously.

We examined the possibility that our measurements were influenced by application of the optical trap's force to the motors. In order to measure bead travel distance, we used an optical trap to initially confine individual beads to the vicinity of a microtubule. Previous studies reported that the force exerted by an optical trap can promote synergistic cooperation between multiple kinesins [50, 51]. It is therefore possible that our use of an optical trap may have biased multiple-motor travel distance toward higher values by influencing how many motors are engaged in transport at the start of a multiple-motor event (before the trap is turned off). We speculate that the magnitude of this effect in our experiments is small, since the trap's effect is more pronounced when the trap's force is larger than or comparable to the force produced by a

single kinesin [50, 51]. In the current study, we used a trap with substantially lower power; beads carried by ~one motor moved processively away from the trap center without detaching prematurely (for example, motile fraction = 0.2, Fig. 2.3 *A*), which is difficult to achieve when the trap's force is comparable to the motor's force [7, 51, 52]. Importantly, regardless of the magnitude of the trap's effect on multiple-motor travel distance, the trap's force cannot increase the distance traveled by a single motor under any circumstances [7, 51, 52]. Thus, while the trap's force may improve the sensitivity for detecting a multiple-motor event, it cannot lead to false identification of a single-motor event as a multiple-motor event.

To understand the discrepancy between our measurements and the previous model (Fig. 2.3 *B*), we next derived a general theory model for the probability of transport by multiple motors (Eqs. 1 and 2, and Fig. 2.4). We then used our lower-bound measurements to constrain the free parameter in our model and to gain insight into the geometry of multiple-motor transport in bead-based assays (Fig. 2.5).

2C-ii. An exact theory expression for the probability of multiple-motor transport

Using the same framework as developed in the previous model [6], we described the probability of bead transport by two or more motors as the weighted sum $P(\geq 2) = \sum_{k=2}^{\infty} p(k \mid n) \cdot g(2 \mid k)$, where n is the average number of motors on the bead, $p(k \mid n)$ is the Poisson probability that there are exactly k motors on the bead, and $g(2 \mid k)$ is the probability that at least two of the k motors on the bead are available for transport. Whereas the Poisson probability $p(k \mid n) = n^k e^{-n} / k!$ only concerns the total number of motors on the bead and does not differ between experiments, the weighting factor $g(2 \mid k)$ is sensitive to experimental details (bead size) and assumptions of multiple-motor transport geometry (Fig. 2.1). As detailed below, the previous model (magenta line, Fig. 2.3 *B*) used an approximation for this weighting factor. We hypothesized that incorporating the exact expression of $g(2 \mid k)$ would help bridge the gap between experiment and theory in Figure 2.3 *B*.

To arrive at an exact expression for $g(2 \mid k)$, we used α to denote the probability that any two randomly attached motors are within simultaneous reach of the microtubule. The value of α is important, since it critically impacts the probability of multiple-motor transport for a given motor number n. Intuitively, the larger the value of α, the more likely it is for two or more motors to engage in transport at a given motor number. The evaluation of α is difficult, since it depends sensitively bead size, as well as assumptions of two-motor transport geometry (Fig. 2.1). Experimental measurements in the current study (Fig. 2.3 *B*) provided the first opportunity to constrain the value of α for kinesin without any geometry assumptions.

The exact expression for the weighting factor is $g(2\,|\,k) = 1-(1-\alpha)^{k-1}$. For any one motor present on the bead, the probability that none of the remaining $k-1$ motors are within simultaneous reach of the microtubule is $(1-\alpha)^{k-1}$. This exact expression differs from the approximated form, $g(2\,|\,k) = \alpha$, used in a previous model [6]. The previous approximation ($g(2\,|\,k) = \alpha$) underestimates the weighting factor for all k > 2. For example, when there are 20 motors on the bead, the probability that two or more motors are within simultaneous reach of the microtubule is larger than that when only two motors are present on the bead.

Using this exact expression for the weighting factor $g(2\,|\,k) = 1-(1-\alpha)^{k-1}$, we obtain the following infinite sum $P(\geq 2) = 1-e^{-n}-ne^{-n}-e^{-n}\sum_{k=2}^{\infty}\frac{n^k(1-\alpha)^{k-1}}{k!}$. To derive a closed-form expression for P (≥2), we denote the infinite sum in the above expression as $S = \sum_{k=2}^{\infty}\frac{n^k(1-\alpha)^{k-1}}{k!}$. Note that S = 0 when n = 0. The derivative of S with respect to n gives rise to $\frac{dS}{dn} = \frac{d}{dn}(\sum_{k=2}^{\infty}\frac{n^k(1-\alpha)^{k-1}}{k!}) = e^{n(1-\alpha)}-1$. Integrating $\frac{dS}{dn}$ yields $S = \frac{e^{n(1-\alpha)}}{1-\alpha}-n+C$. Since S = 0 when n = 0, $C = -\frac{1}{1-\alpha}$ and $S = \frac{e^{n(1-\alpha)}}{1-\alpha}-n-\frac{1}{1-\alpha}$ .Substituting the closed form for the infinite sum, we arrived at a closed-form description for the probability of multiple-motor transport:

$$P(\geq 2) = 1+e^{-n}\left(\frac{\alpha}{1-\alpha}\right)-\frac{e^{-n\alpha}}{1-\alpha}, \qquad \textbf{Eq. 2.1}$$

where n indicates the average number of active motors present on the bead. Since we absorbed geometry considerations into the probability α, this closed-form expression (Eq. 2.1) is general and does not depend on details of multiple-motor geometry (for example, Fig. 2.1 *A* vs. 2.1 *B*). We then recast the dependence on the mean motor number (n) as that on the experimental measurable, motile fraction, using the relationship *motile fraction* $= 1-e^{-n}$ (Fig. 2.2 and [5, 6]).

We next used a numerical simulation to test the validity of Equation 1 (Fig. 2.4). Our numerical simulation captured the three-dimensional nature of the cargo via the usage of a torus lattice; we also included one free parameter to reflect the probability α (Materials and Methods). Predictions from Equation 1 were in excellent agreement with the results of our numerical simulations for all α values tested (black line vs. scatter, Fig. 2.4). On the other hand, when we approximated the probability of multiple-motor transport using $g(2\,|\,k) = \alpha$ as in the previous model, we consistently obtained a lower value than that returned by our numerical simulation (magenta line vs. black scatter, Fig.

2.4). The extent of underestimation was more pronounced for small values of α and diminished as α approached 1. This scenario is expected, since in the limit of $\alpha = 1$, both the exact and the approximate forms of the weighting factor also converge to 1. These data support our hypothesis that the underestimation in $g(2|k)$ contributes to the gap between experiment and theory in Figure 2.3 *B*.

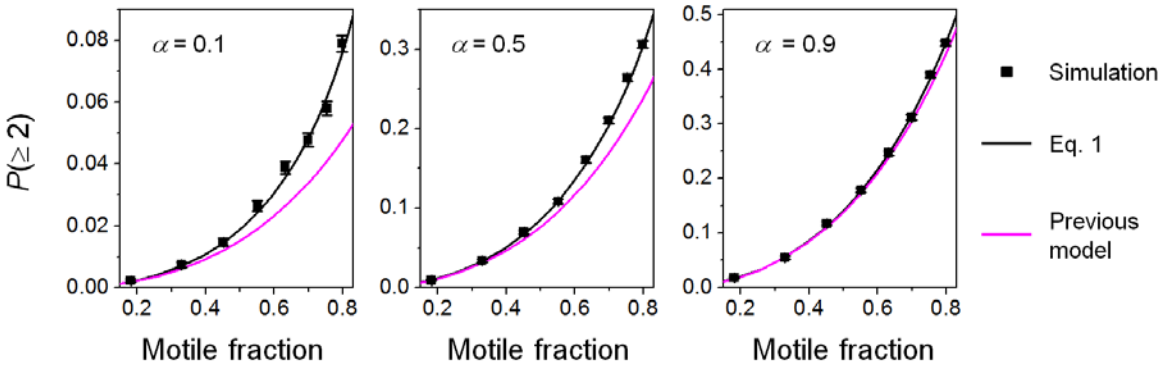

FIGURE 2.4. Probability that a bead is transported by two or more motors, P(≥2), evaluated for three values of α (the probability that two randomly attached motors are within simultaneous reach of the microtubule). Error bars in simulation results indicate standard error (sample size N = 10,000 per simulation condition).

Interestingly, correcting $g(2|k)$ alone was not sufficient to bridge the gap between experiment and theory. When evaluated using the previously estimated value for α (0.099), the probability of multiple-motor transport (as determined by Eq.2.1 and simulation, black line and scatters, Fig. 2.4) remained substantially smaller than our lower-bound measurements (blue scatters, Fig. 2.3 *B*). For example, at a motile fraction of 0.8, we anticipate that ~10% of the motile events are transported by two or more motors (α = 0.1, Fig. 2.4). This value is less than half of the 23% observed experimentally (Fig. 2.3). Thus, our theory study indicates that the value of α is substantially higher than previously anticipated. This finding is perhaps not surprising, since the geometry of two-motor transport used in the previous estimation was itself an approximation (Fig. 2.1 *A*). Importantly, in the updated geometry for two-motor transport, the value of α becomes larger than its previous estimated value (0.099) when kinesin extends beyond 16% of its contour length (80 nm, [36, 37]) (Fig. 2.1 *B*). Since kinesin has been found to extend to at least 28% of its contour length during active transport [53], it is conceivable that α may be larger than previously estimated.

2C-iii. Quantitative comparison between experiment and theory

To enable direct comparison between theory and experiments, we recast Equation 1 to reflect the lower-bound nature of our experimental measurements. Our experimental measurements represent lower-bound values, since our distance threshold excludes the population of multiple-motor transport events that travel ≤6.9 μm (Fig. 2.3). Imposing the same threshold, the expected lower-bound probability of multiple-motor transport is $P_{lower-bound}(\geq 2) = P(\geq 2) - \sum_{i=2}^{\infty} f_i \cdot P(=i)$, where $P(\geq 2)$ is the probability of multiple-motor events without imposing any travel threshold (Eq.2.1), $P(= i)$ is the probability that the bead is transported by exactly i motors, and f_i is the probability that bead travel by exactly i motors exceeds the travel threshold. We previously measured the value of f_2 to be 0.556±0.096 for the experimental condition used in the present investigation (0.01 mM ATP) [41]. Under the same experimental condition, the value of $f_{i>2}$ approaches 1 based on predictions of multiple-motor travel distances by a theory model in [40]. We thus have the following simplification, $P_{lower-bound}(\geq 2) = P(\geq 2) - f \cdot P(=2)$,where $f = f_2 = 0.556$ for simplicity.

The probability that a bead is transported by exactly two motors, $P(= 2)$, is determined by $P(=2) = \sum_{k=2}^{\infty} p(k \mid n) \cdot \alpha \cdot (1-\alpha)^{k-2}$,where n is the average number of motors on the bead, $p(k \mid n)$ is the Poisson probability that there are exactly k motors on the bead, α is the probability that two randomly attached motors are within simultaneous reach of the microtubule, and $\alpha \cdot (1-\alpha)^{k-2}$ is the probability that exactly two of the k motors on the bead are available for transport.

We derived a closed-form expression for $P(= 2)$ as $\frac{\alpha \cdot e^{-n}}{1-\alpha} \sum_{k=2}^{\infty} \frac{n^k (1-\alpha)^{k-1}}{k!}$. Furthering substituting $\sum_{k=2}^{\infty} \frac{n^k (1-\alpha)^{k-1}}{k!} = S = \frac{e^{n(1-\alpha)}}{1-\alpha} - n - \frac{1}{1-\alpha}$, we have $P(=2) = \frac{\alpha \cdot e^{-n\alpha}}{(1-\alpha)^2} - \frac{\alpha \cdot n \cdot e^{-n}}{1-\alpha} - \frac{\alpha \cdot e^{-n}}{(1-\alpha)^2}$ .We thus arrived at the following expression for the expected lower-bound probability of multiple-motor transport

$$P_{lower-bound}(\geq 2) = P(\geq 2) - f \cdot \left(\frac{\alpha \cdot e^{-n\alpha}}{(1-\alpha)^2} - \frac{\alpha \cdot n \cdot e^{-n}}{1-\alpha} - \frac{\alpha \cdot e^{-n}}{(1-\alpha)^2} \right), \quad \textbf{Eq. 2.2}$$

Similar to Eq. 2.1, this description is a function of the experimental measurable motile fraction and the free parameter, α.

Constraining Equation 2 using our experimental measurements, we obtained a best-fit value of α = 0.405 (Fig. 2.5 *A*). Note that since our theory expressions describe the probability of multiple-motor transport for all beads (including those without active motors), we scaled our measurements in Figure 2.3 *B* by their associated motile fractions to obtain the lower-bound measurements on the same probability (blue scatters, Fig. 2.5 *A*). As this best-fit value of α is 4-fold larger than that estimated using the previous model (0.099), our data indicate that the geometry assumed in the previous model (Fig. S1 *A*) is unlikely to occur during bead transport.

Using an updated two-motor geometry [29, 30] (Fig. 2.1 *B*) and our best-fit value of α = 0.405 (Fig. 2.5 *A*), we arrived at a mean extension length of 57 nm for kinesin (Fig. 2.5 *B*). This mean extension length and its associated upper and lower limits (79 nm and 40 nm, respectively) are reasonable as they are within kinesin's contour length (80 nm [36, 37]). These data support the updated geometry and address the question of kinesin's extension length for the typical bead size used in optical trapping (500 nm diameter).

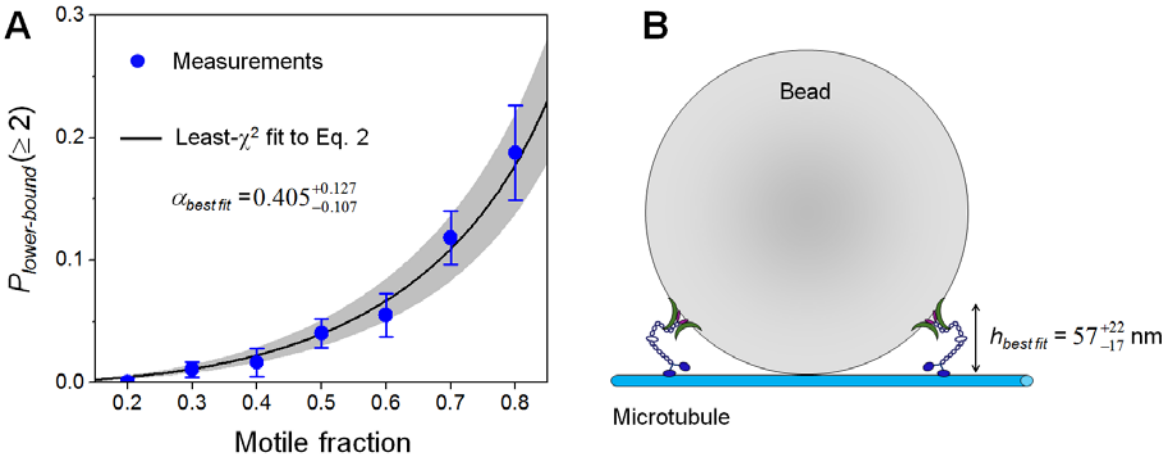

FIGURE 2.5. Quantitative comparison between experiment and theory. (*A*) The lower-bound probability of a bead transported by two or more motors. Scatter, experimental measurements. Error bars, standard error. Solid line and shaded area, least-χ^2 fit and standard error, respectively, for Equation 2. (*B*) An updated geometry for two-motor transport (not to scale). $h_{best\,fit}$, extension length of the kinesin motor, corresponding to the best-fit value of α determined in (*A*).

2C-iv. Estimated fraction of motile beads transported by multiple motors

Based on our findings (Fig. 2.5 and Eq.2.1), we evaluated the probability that a motile bead is transported by two or more motors (Fig. 2.6). To do so, we normalized our expression in Equation 1 by the associated motile fraction. Since only motile events can contribute to transport measurements, the normalized probability directly reflects the impact of multiple-motor events on the measured motility parameters.

Using the best-fit α value for kinesin (Fig. 2.5), we evaluated the fraction of motile beads transported by multiple kinesins (Fig. 2.6, left). For all motile fractions measured, our experimentally constrained estimations were >4-fold larger than previous estimations (black line vs. magenta line, Fig. 2.6, left). We estimate that for motile fractions below 0.387, ≥90% of motile events are due to the action of a single kinesin (Fig. 2.6, left).

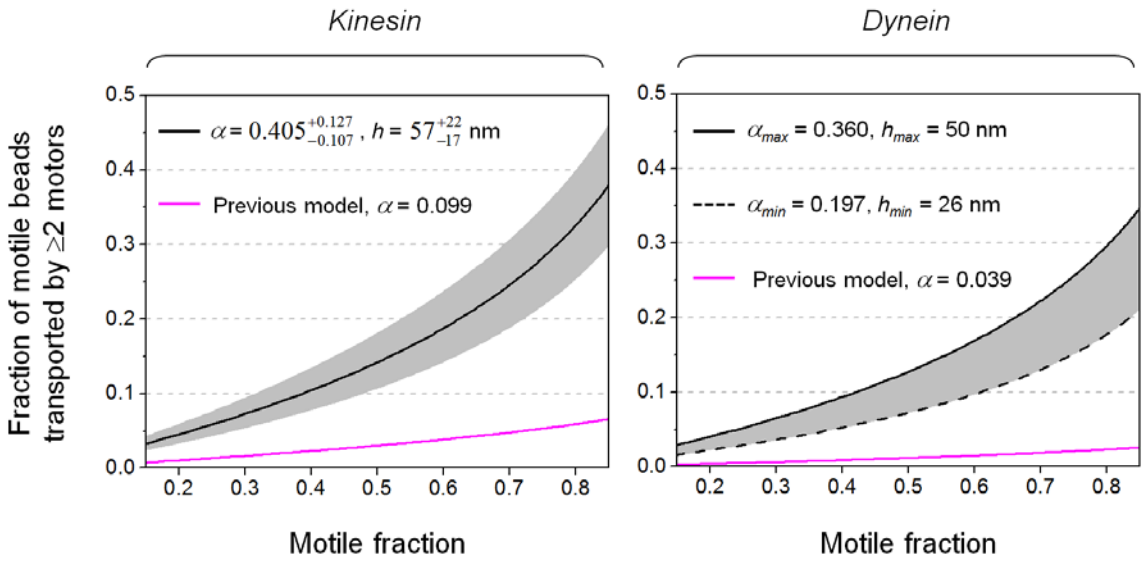

FIGURE 2.6. Fraction of motile beads transported by multiple motors as a function of motile fraction, estimated for two major microtubule-based molecular motors. Magenta lines, a previous model [6]. Black lines and grey area, this study. α, the probability that two randomly attached motors are within simultaneous reach of the microtubule. h, the extension length of the motor while bound to a bead. (Left) Solid black line and grey area, mean ± standard error based on our experimentally constrained α value for kinesin (Fig. 2.5). (Right) Dashed black line and solid black line, minimum and maximum values based on the updated two-motor geometry (Fig. 2.1 *B*) and the motor's extension length, h, supported by previous structural studies of dynein [38, 39, 54].

Using the updated two-motor geometry supported by our study (Fig. 2.5 *B*), we extended our evaluation to another major microtubule-based motor, dynein (Fig. 2.6, right). Here, we could not constrain the extension length of dynein as we did for kinesin, since there is currently no experimental handle to amplify the difference between single- and multiple-dynein travel distances. Instead, we referred to previous structural studies [38, 39, 54] to estimate the range for dynein's motor extension length. This approach is reasonable, since the flexibility of dynein is expected to be substantially more limited than that of kinesin [1].

We used the size of dynein's motor domain to place a lower bound on its extension length (26 nm [54]), and obtained a minimum α value of 0.197 (Fig. 2.1 *B*). This lower limit may be more relevant for studies using minimal dynein constructs containing only the motor domains. Estimations using this lower limit remained >5-fold larger than previous predictions for dynein (black dashed line vs. magenta line, Fig. 2.6, right). We estimate that the motile fraction can be as high as 0.609 while still ensuring that <10% of the motile events are transported by multiple dyneins (dashed black line, Fig. 2.6, right).

We used dynein's contour length as the maximum extension length (50 nm, [38, 39]), corresponding to a maximum α value of 0.36 (Fig. 2.1 *B*). As expected, the probability of multiple-motor transport increased at the higher α value. Using this upper-bound value, we estimate that <10% of motile measurements reflect transport by multiple dyneins for motile fractions below 0.420 (solid black line, Fig. 2.6, right).

2D. Discussion

Here, we combined experiments and theory to determine the probability of multiple-motor transport in bead-based assays. In the experimental portion of our study, we increased our detection sensitivity for multiple- versus single-kinesin transport using ATP concentration as an experimental handle to tune the multiple-kinesin travel distance (Fig. 2.3). We verified that the increased likelihood of long-travel events was directly associated with lower ATP levels (Fig. 2.3 *A*). In our theory work, we derived an exact and closed-form expression for the probability of multiple-motor transport that contains only one free parameter, α (Eq.2.1). Our numerical simulation validated the predictions of our expression for a range of α values (Fig. 2.4). We then recast our expression to reflect the lower-bound nature of our experimental measurements (Eq.2.2). We constrained the one free parameter, α, in our theory model using our experimental measurements (Fig. 2.5 *A*). The resulting predictions constitute a set of quantitative guides for the probability of multiple-motor contributions in single-molecule investigations using optical trapping (Fig. 2.6). To our knowledge, this is the first set of such guides that has been experimentally constrained.

We focused the current study on experimental details used in typical optical trapping studies; specifically, individual motors were uniformly distributed atop spherical beads (500 nm diameter). Under these conditions, we found that it was not necessary to limit single-molecule investigations to motile fractions substantially below 0.2 (such as 0.07 in [31]), where <5% of motile events were due to multiple motors for both kinesin and dynein (Fig. 2.6). Our study also supports the use of a motile fraction of 0.3 for single-molecule investigations [32-35], since we estimated that 7±2% motile events were due to multiple kinesins (<7% for multiple dyneins; Fig. 2.6). Depending on the expected cooperativity of motors functioning in groups and specific requirements for measurement precision, experiments may be carried out at somewhat higher motile fractions to boost experimental throughput.

In general, our results in Figure 2.6 apply only to studies in which the motors are randomly distributed on the bead surface, since we assumed a single parameter, α, across the bead surface. Despite this restriction, our model is appropriate for studies that use intermediate binding sites (antibodies [27, 41] and/or DNA scaffolds [27, 33]) to group motors together locally on the bead surface. In these special cases, the intermediate binding sites are randomly distributed atop the bead surface. Motors bound to individual intermediate sites may be considered to constitute a single "super-motor" complex; evaluation of Equation 1 yields the probability that a bead is transported by multiple super-motor complexes [33, 41].

Further studies are necessary to understand how changing the bead size impacts the predictions in Figure 2.6. Our study supports an updated geometry for two-motor transport in which the motors bind at different locations along the length of the microtubule (Fig. 2.5). In this updated geometry, the value of α depends sensitively on both the bead size and the motor extension length (Fig. 2.1 *B*). For a given extension length, the larger the bead, the less likely it will be for two randomly attached motors to be within simultaneous reach of the same microtubule, thus reducing α. Therefore, if the motor is relatively rigid (as is likely the case for dynein [1]), an increase in bead size (for example, to the ~1 μm-diameter beads used in some optical trapping studies) has the potential to decrease the probability of multiple-motor transport at a particular motile fraction. For flexible kinesin, however, the impact of bead size on α will depend on how the motor's extension length varies with bead size. We are currently investigating the effect(s) of bead size on kinesin's extension length.

For 500 nm-diameter beads, our data indicate that kinesin extends to 57 nm (~71% of its contour length) in bead-based assays (Fig. 2.5 *B*). This finding supports the general assumption that kinesin is in an extended conformation during bead transport (for example [6]). However, an extended conformation for kinesin is also surprising, since kinesin was previously found to adopt a more compact conformation in microtubule-gliding assays, extending to only ~28% of its contour length [53]. The key difference between bead-based assays and microtubule-gliding assays may be that the interface between microtubules and the cargo surface is highly curved in the former but flat in the latter. Our study raises the intriguing possibility that kinesin can exploit its

conformational flexibility to seek and interact with microtubules at highly curved interfaces such as those that occur during vesicle transport in cells.

The experimental approach used here harnesses the increased kinesin/microtubule association time at lower ATP concentrations [40, 41]. Thus, this approach is not limited to specific cargo geometry, motor/cargo recruitment methods, or measurement approach (optical trapping or fluorescence). It is, however, specific to studies of kinesin, for which the inverse correlation between multiple-motor travel and ATP level has been directly demonstrated [40-44]. Future investigations expanding our ability to tune multiple-motor travel distance for other molecular motors (such as dynein) will critically empower this experimental approach. Despite this limitation, when combined with selective small-molecule inhibitors of other motors (such as dynein [55, 56]), the ATP-based strategy may complement current photobleaching- [57] and force-based [58] methods to shed light on the number of kinesin motors involved in the transport of cargos purified from cellular extracts.

Chapter 3. Effect of Microtubule Structural Defect on Kinesin-Based Transport [56]

3A. Introduction

Microtubules are biopolymers that self-assemble from tubulin dimers [24, 57-60]. During self-assembly, tubulin dimers stack longitudinally to form linear protofilaments, with multiple protofilaments associating laterally to form a hollow tubular structure, the microtubule (Fig. 3.1 *A* in the Supporting Material). Each microtubule is not necessarily perfect and can exhibit packing mistakes in the tubulin dimers (defects). The range of defects in microtubules include missing tubulin dimers [61, 62] and changes in the number of assembled protofilaments [62, 63] (Fig. 3.1 *B*). These defects have been observed for microtubules in vitro [59-61] and in cell extracts [61].

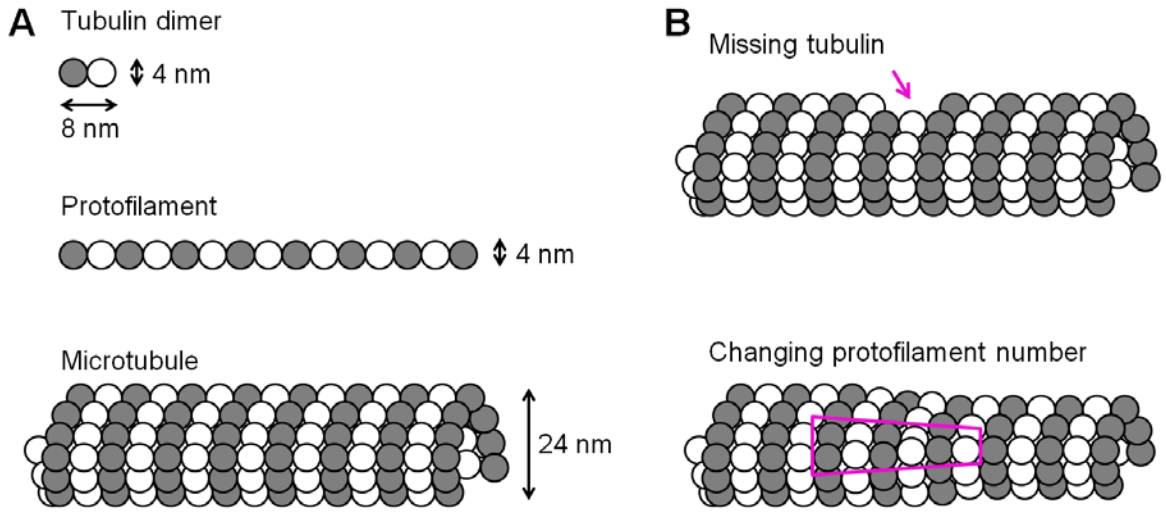

FIGURE 3.1. Schematic of microtubule self-assembly (*A*) and the range of microtubule defects reported by previous studies [59, 62, 63] (*B*). Illustrations are not to scale. (*A*) Microtubules are tubular structures formed via hierarchical self-assembly of tubulin dimers into protofilaments, which then associate to form a hollow tube [59-62]. Tubulin dimers are heterodimers composed of α and β tubulin monomers (~4 nm in diameter), as indicated by grey and white spheres. (*B*) Defects in the microtubule structure were previously uncovered by cryoelectron microscopy [60-62] and scanning force microscopy [59]. These

defects include missing tubulin dimers (top) and changes in the numbers of protofilaments (bottom). The biochemical nature of these defects is not clear. The physical size of these defects is ~1/20th below the optical resolution limit. Direct visualization of these defects during motility assays is not currently possible and is outside of the scope of this study

Molecular motors such as kinesin rely on microtubules as molecular highways to drive mechanical transport in cells [57, 60, 61, 64, 65]. This transport is critical for eukaryotic cell function and survival. Each individual kinesin typically tracks a single protofilament in each microtubule [64]. Since microtubule defects include disruptions within individual microtubule protofilaments (Fig. 3.1 B), we hypothesized that these defects may influence kinesin-based transport.

A key experimental challenge for testing our hypothesis is that microtubule defects cannot be directly observed in current motility experiments using optical microscopes. Label-free imaging is not yet possible because the physical size of microtubule defects is ~1/20th below the optical resolution limit. There are also no known biomarkers for specific and non-invasive labeling/imaging of these structural defects, as the biochemical nature of the tubulin dimer within/surrounding these lattice defects is not yet understood.

To overcome these experimental challenges, we developed a single-microtubule assay to probe the effects of microtubule defects on kinesin-based transport in vitro. Since molecular motors typically work in small groups to transport materials in cells [57, 64, 65], we focused our investigations on cargo transport by more than one kinesin. To address the effects on transport by different motor numbers, we examined two regimes: one in which each bead was carried by a few kinesins and one in which each bead was carried by many motors. We found that microtubule defects influence kinesin-based transport in a manner that depends on the number of motors present on the cargo.

3B. Materials and methods

3B-i. Proteins and reagents

Kinesin and tubulin were purified from bovine brains as previously described [45, 46]. Kinesin, which was microtubule-affinity purified and free of “dead” motors [46], was flash frozen in PMEE buffer (35 mM piperazine-N,N’-bis(2-ethanesulfonic acid) (PIPES), 5 mM $MgSO_4$, 1 mM EGTA, 0.5 mM EDTA, pH 6.8) supplemented with 45% glycerol and 1 mM dithiothreitol. Tubulin, which was free of microtubule-associated proteins [45], was flash frozen in PM buffer (100 mM PIPES, 1 mM $MgSO_4$, 2 mM EGTA, pH 6.9) supplemented with 45% glycerol and 1 mM dithiothreitol. Anti-tubulin

antibody (T7816, clone SAP.4G5), poly-L-lysine (P8920), Pluronic F-127 (P2443), and chemicals (unless otherwise specified) were purchased from Sigma-Aldrich (St. Louis, MO, USA). Dimethyldichlorosilane solution (2% wt/vol, Repel-Silane ES) was purchased from GE Healthcare Bio-Sciences (Marlborough, MA, USA). Guanalyl-(α,β)-methylene diphosphate (GMPCPP) was purchased from Jena Biosciences (Jena, Germany).

3B-ii. Microtubule preparation

Microtubules were assembled in vitro and were free of microtubule-associated proteins. Two assembly conditions (taxol-stabilized and taxol-polymerized) were used to alter the frequency of defects in the assembled microtubules as previously described [45]. Both taxol-stabilized and taxol-polymerized microtubules were kept at room temperature in a dark box and used within 8 days of preparation.

Taxol-stabilized microtubules were prepared as described in Chapter 2B-ii.

Taxol-polymerized microtubules were assembled in one step in the presence of taxol. Due to the increased microtubule-assembly rate in the presence of taxol [46], tubulin solution was diluted to 4 μM in PM buffer supplemented with 10 μM taxol and incubated for 30 min at 37°C for assembly as previously described [45].

A third assembly condition was used to alter the fraction of microtubules displaying supertwist [60]. Tubulin (4 μM) was supplemented with 1 mM GMPCPP and incubated for 3 h at 37°C [60]. The assembled microtubules were diluted to 50 nM in PM buffer supplemented with 10 μM taxol and immediately introduced into flow cells for motility experiments. We refer to this third type of microtubule as “GMPCPP” microtubules.

3B-iii. Flow cell preparation

Motility investigations were carried out in flow cells in vitro. Flow cells were constructed by sandwiching a coverslip (22x40 mm, No. 1.5, Thermo Fisher Scientific Inc., Waltham, MA, USA) and a microscope slide (25x75 mm, Thermo Fisher Scientific Inc.) using double-sided Scotch tape. Both the microscope slide and the coverslip were biologically clean. The coverslip surface was either coated with poly-L-lysine or silanized to immobilize microtubules.

To immobilize microtubules through non-specific interaction with poly-L-lysine, the coverslip surface was plasma cleaned and then incubated with poly-L-lysine

(0.00027% w/v in ethanol, 10 min). The coverslip was then oven dried (85°C, 10 min) prior to flow-cell construction. The microscope slide was not exposed to poly-L-lysine in order to minimize the presence of poly-L-lysine in the flow cell. Microtubules (taxol-stabilized or taxol-polymerized) were diluted to 50 nM in PMEE buffer (pH 7.2) supplemented with 1 mM GTP and 10 μM taxol and introduced into the flow cells. These microtubules underwent non-specific binding to the poly-L-lysine-treated coverslip surface. The flow cell was rinsed with wash buffer (11.7 mM PIPES, 1.6 mM $MgSO_4$, 0.3 mM EGTA, 0.12 mM EDTA, pH 7.2) supplemented with 1 mM GTP and 10 μM taxol and then blocked with 5.55 mg/mL casein solution in PMEE buffer supplemented with 1 mM GTP and 10 μM taxol. The resulting flow cell typically contained one or two isolated microtubules extending across the full width of our field of view. We used the same procedures to make flow cells with GMPCPP microtubules, except that we excluded GTP from the buffers. Unless otherwise indicated, experiments in the current study were carried out using polylysine-based immobilization.

To immobilize microtubules using anti-tubulin antibody, the coverslip surface was plasma cleaned and then treated with a dimethyldichlorosilane solution (2% wt/vol, 5 min). The coverslip was immersed in ethanol twice (5 min each), rinsed in Nanopure water three times, and air dried prior to flow-cell construction [66]. The flow cell was incubated with 20 μg/mL anti-tubulin antibody in PEM80 buffer (80 mM PIPES, 4 mM $MgSO_4$, 1 mM EGTA, pH 6.9) for 5 min, and surface-blocked using 1% Pluronic F-127 in PEM80 buffer [67]. Taxol-stabilized microtubules were diluted to 200 nM in PMEE buffer (pH 7.2) supplemented with 1 mM GTP and 10 μM taxol and introduced into the flow cells for 10 min. Excess microtubule was washed out using PEM80 buffer supplemented with 20 μM taxol and 10 mM dithiothreitol.

3B-iv. Motor/bead preparation

Carboxylated polystyrene beads (0.2 μm, Polysciences Inc., Warrington, PA, USA) were used to facilitate optical trap-based motility measurements as described in Chapter 2B-iii. In experiments using antibody-supported microtubules, kinesin was incubated with beads in motility buffer supplemented with 0.04% Pluronic F-127 [66]. The motor/bead solution was then supplemented with an oxygen-scavenging solution (250 μg/mL glucose oxidase, 30 μg/mL catalase, 4.6 mg/mL glucose, Sigma-Aldrich) and 1 mM ATP prior to motility measurements.

We examined both few-motor transport and many-motor transport in the current study. To reach the few-motor range, we empirically tuned the kinesin-to-bead ratio such that the mean bead travel distance using measurements pooled over multiple microtubules was similar to that previously reported for transport by exactly two kinesins [41, 43, 68, 69]. To reach the many-motor range, we increased the motor-to-bead ratio by ~4-fold from the few-motor range.

For the few-motor system studied using polylysine-supported microtubules, 1.4 nM kinesin was incubated with a solution of 2.8×10^6 beads/μL. We reduced this motor-to-bead ratio to ~1.3 nM kinesin per solution of 2.8×10^6 beads/μL in Figure 3.3 in order to access a somewhat lower motor number in the few-motor range.

For the few-motor system studied using antibody-supported microtubules, we found that the presence of 0.04% Pluronic F-127 in the motility buffer resulted in a somewhat lower level of motor/bead binding (data not shown). We therefore used higher concentrations of motors and beads during incubation while keeping the motor-to-bead ratio the same as that in Figures 1 and S2-S4. Specifically, 3.1 nM kineisn was incubated with a solution of 6.2×10^6 beads/mL for 10 min. The resulting motor/bead solution was diluted to 2.8×10^6 beads/mL to achieve the bead density suitable for optical trapping.

For the many-motor system studied using polylysine-supported microtubules, 4.4 nM kinesin was incubated with 2.3×10^6 beads/μL.

For the many-motor system studied using antibody-supported microtubules, 8.8 nM kinesin was incubated with 4.6×10^6 beads/μL. The resulting motor/bead solution was diluted to 2.3×10^6 beads/μL for optical trapping.

3B-v. In vitro optical trapping

A single-beam optical trap [8] was constructed and integrated with differential interference contrast imaging using an inverted microscope (Ti-E, Nikon, Melville, NY, USA). The optical trap (~20 mW at the laser output) was used to position individual kinesin-coated beads to a unique position on each microtubule under study. Throughout each experiment, we maintained both the optical trap and the microtubule in a static position and allowed Brownian fluctuation to bring the kinesin-coated beads to the optical trap. Upon observation of directed motion, the optical trap was manually shut off to allow bead motility without external load. We enhanced the Brownian motion of the kinesin-coated beads by using beads 0.2 μm in diameter [42], smaller than the usual 0.5-1 μm-diameter beads in optical trapping studies [8]. The density of beads in our flow cell was empirically tuned to further enhance the probability that an individual bead is immobilized by the static optical trap, while minimizing the probability of multiple beads being trapped at the same time.

Bead trajectories were imaged at 250x magnification using differential interference contrast microscopy. Video data were recorded using a Giga-E camera (Basler SCA640-70GM, Basler AG, Ahrensburg, Germany) at 30 Hz. For each microtubule segment, 50-150 trajectories were measured, typically using different beads in the same flow cell.

3B-vi. Data analysis

Bead trajectories were analyzed as described in Chapter 2B-v. with the following exception. Unusual features in single-microtubule travel distributions were identified by comparing each distribution to its best-fitted value assuming the usual single-exponential decay function [5]. An increase in counts was scored if the measurement was (a) greater than three times its best-fitted value and (b) at least 20% of the maximum measurement in the distribution. A decrease in counts was scored if the best-fit count value was (a) greater than three times the measured value and (b) at least 20% of the maximum measurement in the distribution. Note that our selection criteria for these unusual features were strict (in particular criterion (b) for both an increase and a decrease in counts) and did not include all substantial deviations between the measurements and the fitted values detected.

Pausing was defined as the interruption in continuous bead motion along the microtubule axis. A pause event was scored when the instantaneous velocity of a bead (evaluated over 1 s) fell below a threshold of 0.15 μm/s [69]. To account for thermal drift in our sample stage (up to 150 nm in amplitude over the typical 1 h duration of each experiment), we binned the on-axis position of each microtubule into discrete locations (180 nm bin width). Note that this coarse binning is implicit in the distribution of travel distances (650 nm bin). For each microtubule, the mean number and standard deviation of trajectories pausing at each discrete location on a microtubule was calculated using all trajectories measured for that microtubule; a common pause location was identified when the number of pauses at a particular on-axis position was >4 standard deviations above the mean.

Pausing probability for each microtubule was determined as the fraction of trajectories that paused at least once on the microtubule. Standard error for pausing probability was calculated as the 68.3% confidence interval for a binomial distribution. The paired-sample t-test was used to determine the statistical significance of the difference in pausing probability between taxol-stabilized and taxol-polymerized microtubules.

Off-axis positions for each bead trajectory were mean removed and sign corrected such that a positive off-axis value corresponded to the left side of the microtubule axis when facing the direction of kinesin travel. The mean off-axis position for each bead trajectory was calculated as the midpoint between the minimum and maximum off-axis positions measured. The distribution of off-axis positions of beads (during pausing and during motion) was summed over all trajectories for each microtubule; the normalized distribution of off-axis positions for each microtubule was averaged over all microtubules. This approach limited potential bias toward individual microtubules.

The rank-sum test was used to determine the statistical difference between two distributions of travel measurements. A one-way analysis of variance was used to

determine the statistical difference between multiple distributions of travel measurements.

3C. Results

3C-i. A single-microtubule assay to probe the effects of microtubule defects on cargo transport

Here, we developed a simple assay to measure multiple cargo trajectories along the same microtubule segment (Fig. 3.2 *A*). Multiple measurements are necessary to sample defect sites on a microtubule surface: since a defect is small compared to the overall microtubule surface available for cargo transport, the probability that a particular cargo trajectory will encounter a defect site is likely to be small. Using a single-beam optical trap, we defined and maintained a unique interaction site for cargos on each microtubule (Fig. 3.2 *A*). This approach enabled us to repeatedly survey the same microtubule segment, thereby increasing the net number of trajectories encountering and being influenced by microtubule defects. We anticipated that these trajectories would provide a direct, functional readout on the hypothesized impact of microtubule defects on motor function. Since this approach focused on transport along individual microtubules, we refer to it as the "single-microtubule assay."

3C-ii. Common unbinding sites on microtubules for transport by a few motors

We first investigated the potential impact of microtubule defects on beads transported by a few kinesins (Fig. 3.2). We empirically tuned the motor-to-bead ratio such that the resulting mean bead travel distance (pooled over multiple microtubules) was within the range previously reported for transport by exactly two kinesins (assembled using DNA/protein-based structures) [41, 43, 68, 69]. We refer to this range as "few-motor transport" because the number of motors decorating each bead is Poisson-distributed rather than well-defined in bead-based studies [5, 6] and in vesicle transport in vivo [43, 57]. To capture the key characteristics of microtubule assembly in cells [6], we utilized microtubules assembled in the presence of GTP. To halt the dynamic disassembly of microtubules during our motility studies in vitro, we stabilized these assembled microtubules via taxol [70], and refer to them here as "taxol-stabilized microtubules."

We observed significant variations in single-microtubule travel distributions measured under otherwise identical conditions (Fig. 3.2). A total of 33 single-microtubule travel distributions were measured, corresponding to ~70 trajectories along each

microtubule. A one-way analysis of variance revealed significant differences among the 33 single-microtubule travel distributions, $F(32, 2434) = 9.16$, $P < 0.001$. To control for the possibility that these travel variations reflect experimental variations between kinesin/bead preparations, we focused on the subset of measurements for different microtubules in the same flow cell (Figs. 3.2 *B*). Since the same population of kinesin-decorated beads was present in each flow cell, the only variable in our experiments was the microtubule along which the beads traveled. For these side-by-side measurements, we again observed significant travel differences between microtubules for 3/8 triplet sets (Figs. 3.2 *B*).

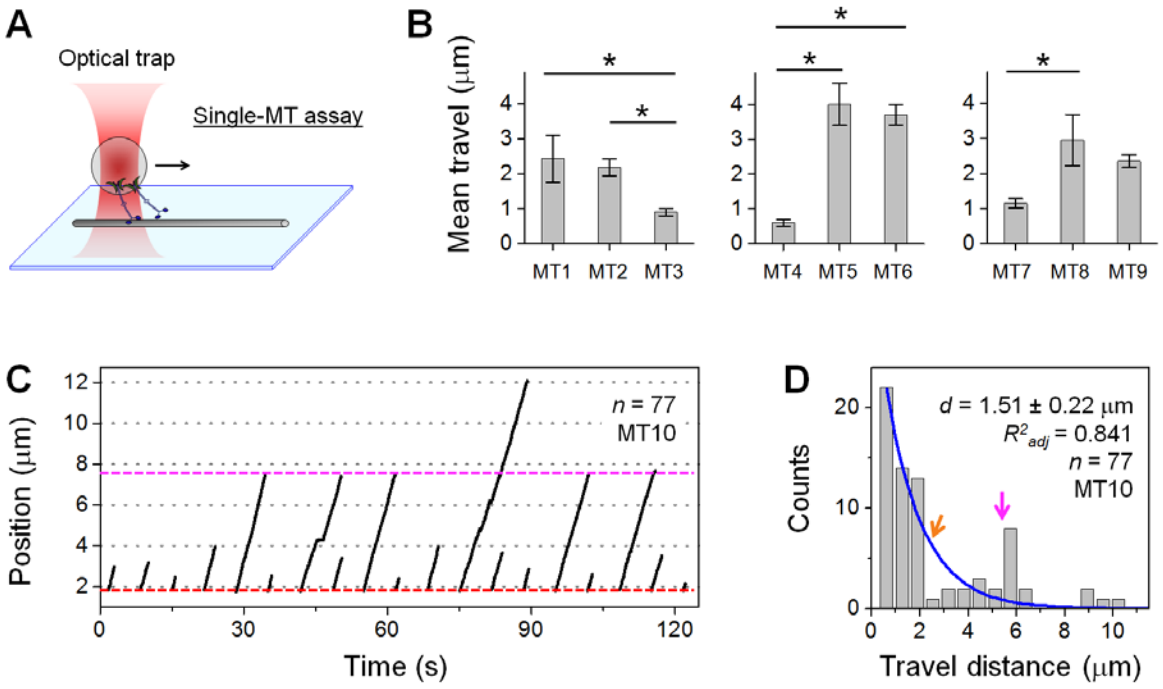

FIGURE 3.2. Single-microtubule (MT) measurements of cargo travel for few-kinesin transport. (*A*) Schematic of our single-MT assay (not to scale). An optical trap directs kinesin-coated beads to a unique position on a MT. (*B*) Mean travel distances of beads measured for individual MTs. MT1-3, 4-6, and 7-9 represent sets of three MTs; each set was measured in the same flow cell. Error bars, standard error. Asterisks, significant differences in cargo travel distance between MT pairs ($P < 0.02$, rank-sum test). (*C*) Example single-MT trajectories sharing the same initial travel position (red dashed line) on a single MT. Each trajectory represents a different bead trapped from the same bead population in the flow cell; the trajectories are offset with regard to their relative timing (x axis) in order to facilitate comparison. *n*, total number of trajectories measured for this MT. Magenta dashed line, MT position at which several beads disengage from transport. (*D*) Single-MT travel distribution corresponding to trajectories in (*C*).

Blue line, best fit to a single exponential decay. Mean travel distance (d ± standard error), goodness of fit (R_{adj}^2), and sample size (n trajectories) are indicated. Arrows, deviations from best fit (magenta, more counts; orange, fewer counts; see Materials and Methods in this chapter).

What is responsible for these travel variations? To address this question, we examined each of the 33 single-microtubule travel distributions. For 6/33 microtubules (18%), we observed unusual features indicating common unbinding sites on each microtubule (Figs. 3.2 *D*). For example, rather than the distribution being well approximated by the usual single exponential decay [5], we observed 11-fold more counts than expected for the travel distance of ~5.7 μm (magenta arrow, Fig. 3.2 *D*), and 6-fold fewer counts than expected for the travel distance of ~2.5 μm (orange arrow, Fig. 3.2 *D*). These substantial deviations reflect common unbinding sites on the microtubule: since each trajectory shared the same starting position on a microtubule (red line, Fig. 3.2 *C*), trajectories with the same travel distance must unbind at the same location along the microtubule (magenta arrow in Fig. 3.2 *D* and magenta line in Fig. 3.2 *C*). Note that when the common unbinding event is located near the initial travel position, the increase in counts biases the fitting toward a longer decay constant, resulting in an apparent reduction in counts in the travel distribution (orange arrow, Fig. 3.2 *D*). The locations of these unusual features differed between microtubules without apparent periodicity, the magnitudes of these unusual features diminished in travel distributions pooled from measurements using multiple microtubules.

Perhaps strikingly, despite the presence of more than one motor per cargo, the mean travel distance for 3/33 microtubules (9.1%) was substantially smaller than the average travel distance for a single kinesin (Figs. 3.2 *B*). For example, beads traveled 0.63 ± 0.05 μm (mean ± standard error, n = 64) along MT4, corresponding to a 37% reduction below single-kinesin travel [5] (Fig. 3.2 *B*). This reduction in mean travel distance cannot be simply explained by experimental variation in the kinesin-to-bead ratio or by a loss of motor activity, since the same population of beads gave rise to significantly longer mean travel distances for the two microtubules measured at later time points in the same flow cell (MT5 and MT6 in Fig. 3.2 *B*). Instead, it is consistent with local clustering of one or more unbinding sites near the initial travel position on the microtubule.

Together, these data support our hypothesis that microtubule defects influence cargo transport, for example by prompting kinesins to dissociate prematurely from the microtubule.

3C-iii. No significant effect of microtubule supertwist on cargo travel/unbinding

Next, we sought to control for the possibility that common unbinding sites were artifacts of microtubule supertwist (Fig. 3.3), the rotation of individual protofilaments along the microtubule axis. Since each kinesin typically tracks a single protofilament during transport [71], it is formally possible that the cargo travel may unbind at the interface between rotating protofilaments and the coverslip surface that supports the microtubule.

We tested this possibility by increasing the probability of each cargo encountering a microtubule/coverslip interface (Fig. 3.3 *A*). Previous studies reported that ~40% of taxol-stabilized microtubules (which we used thus far) have supertwist [5], whereas ~95% of GMPCPP microtubules (Materials and Methods in this chapter) have supertwist [5, 72]. We therefore generated GMPCPP microtubules for comparison with taxol-stabilized microtubules [60]. We used a single population of tubulin dimers to keep the biochemical makeup of these two types of microtubules constant. We also used the same kinesin/cargo preparation (Fig. 3.3 *A*) and altered the measurement order of the microtubule types for each set of pairwise comparisons. A total of six microtubule pairs were tested.

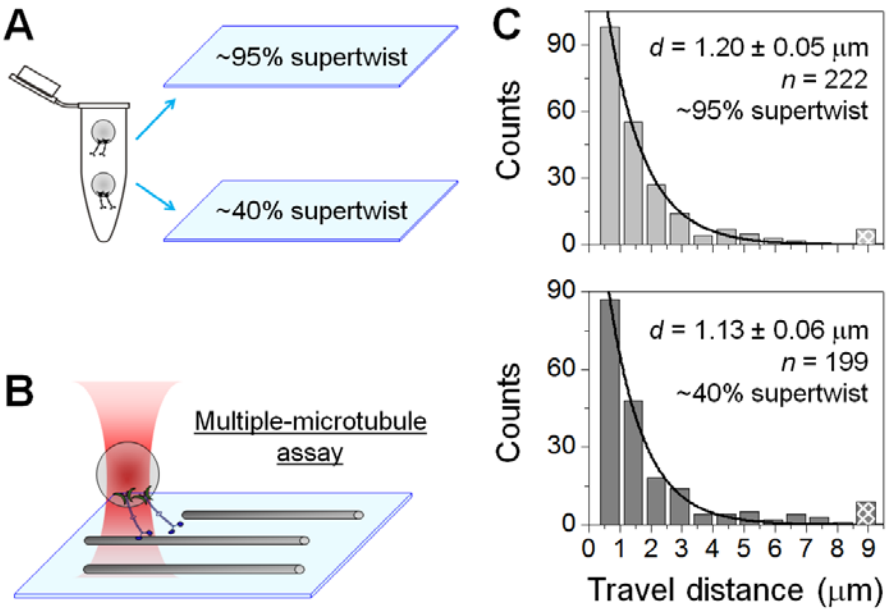

FIGURE 3.3. Pairwise comparisons of travel distance along two types of microtubule that differed in their respective likelihood of displaying supertwist (95% and 40%). (*A*-*B*) Experimental schematic (not to scale). We used the same kinesin/bead mixture to contrast transport between the two types of microtubules (*A*). We used the standard multiple-microtubule assay to minimize the influence of microtubule defects (*B*). (*C*) Distribution of few-kinesin travel along each microtubule type. Hatched bars at ~9 μm indicate travel distances that

exceeded our field of view. Solid line, best fit to a single exponential decay. Mean travel distance (d ± standard error) and sample size (n trajectories) are indicated. These distributions do not differ significantly from each other (P = 0.36, rank-sum test).

To isolate the effect of supertwist and to minimize the impact of microtubule defects on these comparisons, we employed the standard multiple-microtubule assay [5] (Fig. 3.3 *B*). We measured one and only one cargo trajectory for each microtubule and sampled ~200 microtubules to obtain the average travel distance along each microtubule type. The probability that each trajectory encounters the defect on a microtubule is low, and the locations of defects likely differ between microtubules. Thus, the key difference between the two microtubule types is the probability of a microtubule displaying supertwist (40% [73] vs. 95% [5, 74]).

We did not detect any significant difference in cargo travel between these two types of microtubules (Fig. 3.3 *C*). Note that to amplify the sensitivity of cargo travel to this potential surface effect, we used fewer motors per cargo here than in the experiments in Figure 3.2. Cargo transport remained in the few-motor range, with a mean travel distance longer than that resulting from transport by a single kinesin (>1.1 μm in Fig. 3.3 *C* vs. ~1 μm for the native bovine kinesin used in this study [5]). Our data demonstrate that microtubule supertwist does not contribute significantly to the travel variations and common unbinding events in our few-kinesin system.

3C-iv. Cargo unbinding occurs independently of the microtubule-immobilization method

To further investigate the possibility of surface effects, we used anti-tubulin antibody to elevate microtubules above the coverslip surface (Fig. 3.4 *A*), in addition to the polylysine-supported microtubules investigated thus far. We also employed a different surface-blocking agent (Pluronic F-127 for the antibody-based immobilization vs. casein for polylysine-based immobilization) to reduce non-specific interactions between motor-decorated beads and the coverslip surface. We measured few-motor travel along different taxol-stabilized microtubules using the same population of motor/bead complex in a single flow cell (Fig. 3.4 *B*).

We detected significant differences in travel distance between antibody-supported microtubules (asterisks, Fig. 3.4 *B*). For example, the rank-sum test returned a P-value of 0.0024 for travel along $MT_{antibody}2$ versus $MT_{antibody}3$ (asterisks, Fig. 3.4 *B*). One-way analysis of variance also revealed significant differences among the three single-microtubule travel distributions ($F(2, 187) = 7.57$, $P < 0.001$).

Data from antibody-supported microtubules also substantially deviated from the typical single exponential decay (Fig. 3.4 *B*). For example, for $MT_{antibody}2$, we observed 8.5-fold more counts than expected for the travel distance of ~5.5 μm (magenta arrow, Fig. 3.4 *B*). For $MT_{antibody}3$, we detected 3.4-fold fewer counts than the fitted value for the travel distance of ~2.3 μm (orange arrow, Fig. 3.4 *B*), as well as >11-fold more counts than the fitted values for travel distances of 3.9-5.5 μm (magenta arrows, Fig. 3.4 *B*). Taken together, these data demonstrate that cargo unbinding during few-motor transport is not specific to any particular microtubule immobilization method.

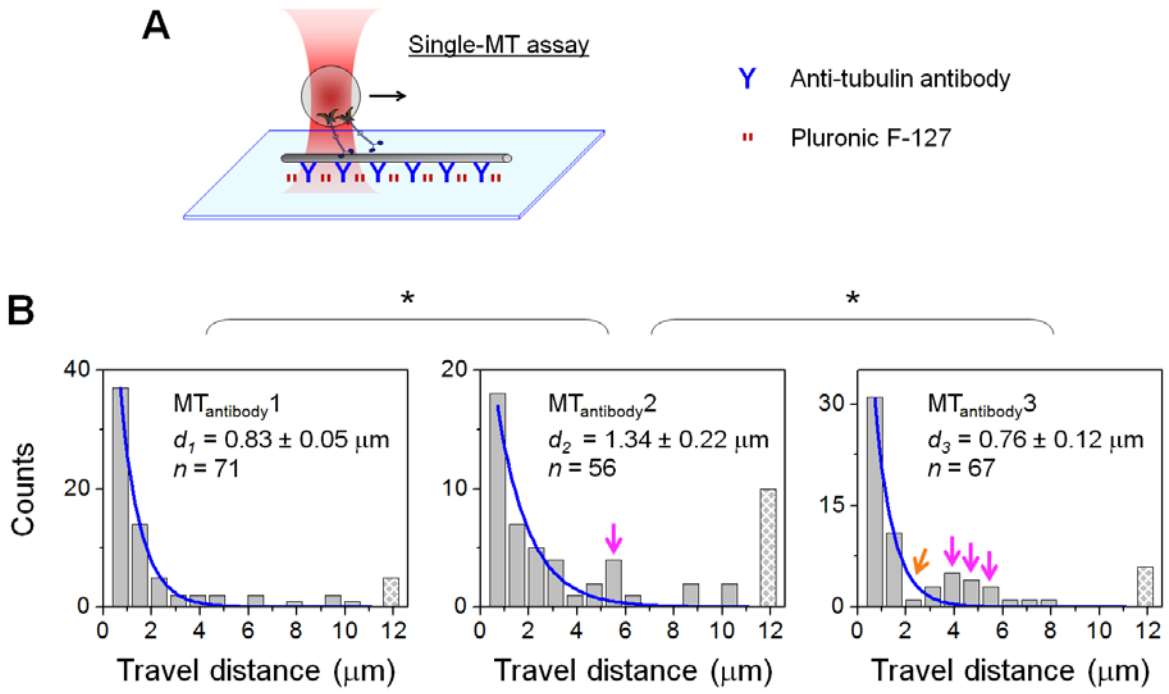

FIGURE 3.4. Measurements of cargo travel along antibody-immobilized microtubules (MTs). (*A*) Experimental schematic (not to scale). Anti-tubulin antibody was used to elevate the MT above the coverslip surface and Pluronic F-127 was used to reduce non-specific interactions between motor/bead complexes and the coverslip. (*B*) Single-MT travel distributions measured for three MTs in the same flow cell. Asterisks, significant differences in cargo travel distance between MT pairs ($P < 0.02$, rank-sum test). Blue line, best fit to a single exponential decay. Mean travel distance (d ± standard error) and sample size (n trajectories) are indicated. Hatched bars at 12 μm indicate cumulative counts of travel distance that exceeded our field of view. Arrows, substantial deviations between measurements and best-fitted values.

3C-v. Common pause locations on microtubules for many-motor transport

Next, we increased the motor-to-bead ratio by ~4-fold to reach the many-motor transport range (Materials and Methods). The resulting cargo travel distance increased significantly versus that of the few-motor system (>20 μm in Fig. 3.5 vs. the few μm range in Fig. 3.2), suggesting that unbinding events were substantially suppressed by the increase in motor number. We hypothesized that the extended travel in this many-kinesin system (Fig. 3.5 *A*-*B*) would expand the range of effects detectable by our assay as well as increase the number of defects encountered by each trajectory. This many-motor range may also shed light on the long-range transport of large cargos in vivo, such as the movement of mitochondria in neuronal processes and nuclear migration [5, 73, 75]. For consistency, we continued to use taxol-stabilized microtubules and polylysine-based immobilization as we did for experiments in Figure 3.2.

We found that the probability of cargo pausing during continuous transport increased from 2.7 ± 0.4% for few-kinesin transport to 13.2 ± 1.2% for many-kinesin transport (arithmetic mean ± standard error; n = 33 and 42 microtubules, respectively). This observation is consistent with previous findings (using multiple-microtubule assays) that pausing in kinesin-based transport occurs minimally for single kinesins [76-78] and more frequently for multiple motors [66, 69].

Interestingly, our single-microtubule study revealed common pause locations for 9/42 microtubules (Figs. 3.5 *A*-*B*). For example, seven trajectories paused at the same site on MT34 (~8 μm, Fig. 3.5 *A*), and 12 trajectories paused at a single site on MT35 (~16.4 μm, Fig. 3.5 *B*). Both of these pause counts were >4 standard deviations above the mean for each microtubule. The positions of these common pauses were relative to the position of our optical trap, and did not correspond to any underlying rotational pitch of the microtubule. The locations of these common pause sites also differed between microtubules (Fig. 3.5 *A*-*B*). Together, these findings are consistent with our hypothesis that microtubule defects influence kinesin-based transport, for example by triggering cargo pausing in many-kinesin transport.

3C-vi. Cargo trajectories during pausing reflect force-based interactions between motors

For all pauses, we observed that the cargo velocity gradually slowed to zero while entering a pause, and recovered to normal levels after the pause (~0.8 μm/s, Fig. 3.5). The initial slowdown indicates that the motors transporting these cargos experienced substantial force opposing their motion, as kinesins respond to forces opposing the direction of their travel by slowing [6, 7, 52]. Since we turned off the optical trap upon

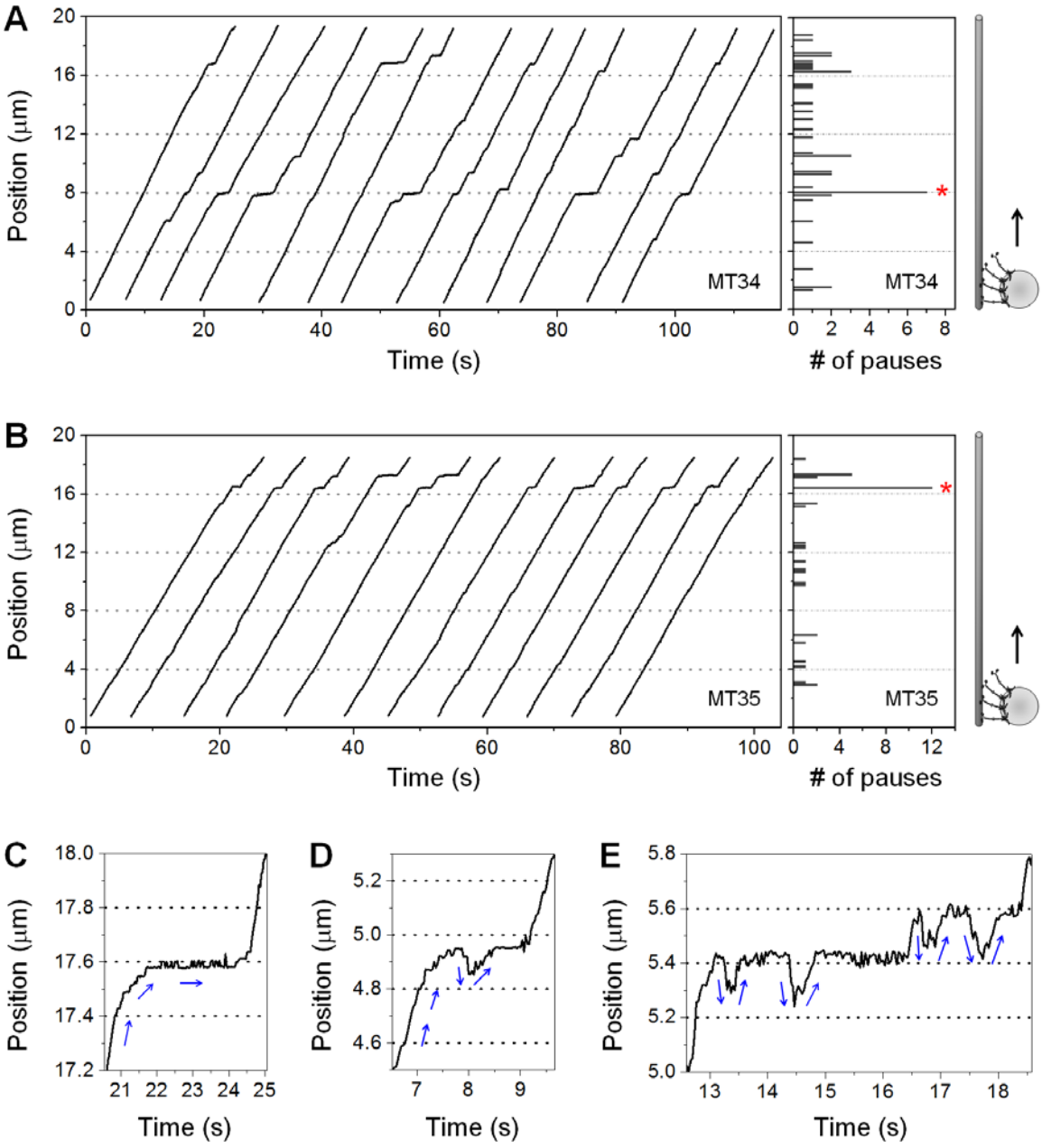

FIGURE 3.5. Single-microtubule (MT) measurements of cargo pausing during many-kinesin transport. (*A-B*) Example trajectories (left) and the corresponding distribution of pauses along the MT axis (right) measured for two MTs. Each trajectory represents a different bead trapped from the same bead population in a single flow cell; the trajectories are offset with regard to their relative timing (x axis) in order to facilitate comparison. Red asterisks indicate common pause locations (>4 standard deviations above the mean number of pauses for that MT). (*C-E*) Example trajectories exhibiting static (*C*) and dynamic (*D-E*) pausing. Blue arrows indicate the direction of cargo travel. Mean

cargo velocity (± standard error) during dynamic pausing (*D*-*E*) was 2.0 ± 0.4 μm/s (n = 11) during backward movement and 0.66 ± 0.16 μm/s (n = 11) during forward movement.

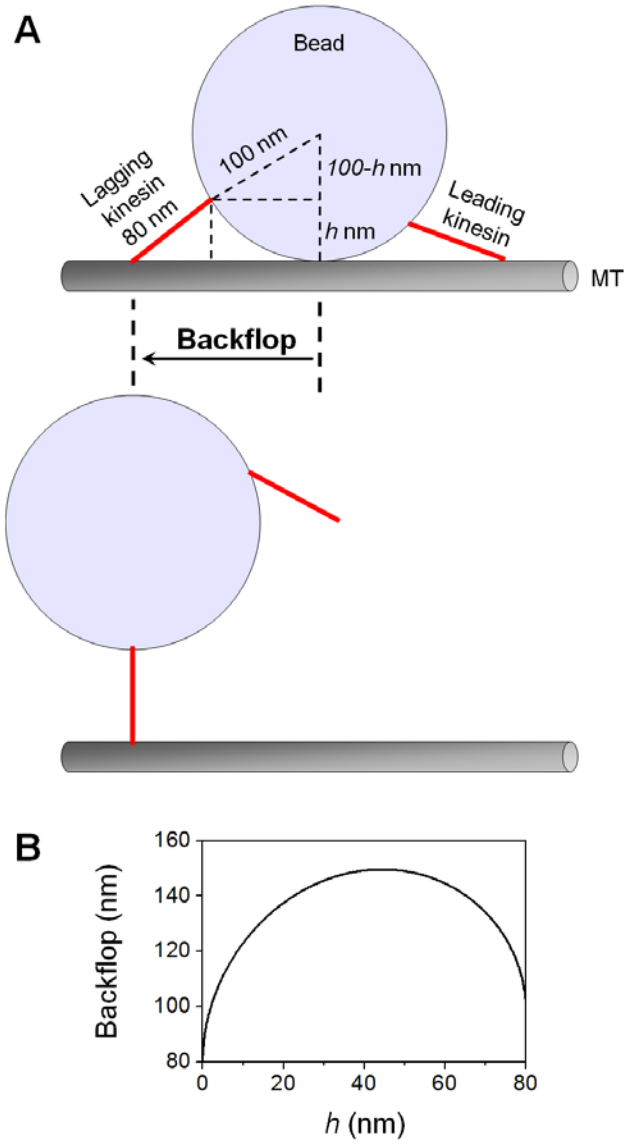

FIGURE 3.6. Estimated size of cargo back-flop, given kinesin's contour length (80 nm [36, 37]), (*A*) Schematic of cargo flopping back to the position of the lagging motor after the leading motor unbinds from the microtubule. Illustration is to scale. Red lines indicate kinesin motors. h is determined by the relative positions of motors binding the cargo; h ranges between 0 and 80 nm. (*B*) Estimated size of cargo back-flop, as determined by $\sqrt{80^2 - h^2} + \sqrt{h(200 - h)}$.

The backward excursion size may be larger than estimated here, since the lagging motor may extend beyond its contour length under forward load [52].

observation of directed bead motion, the source of opposing force must be internal to the team of motors transporting the same cargo: a subset of motors on the cargo paused on the microtubule and hindered other motors from pulling the cargo forward. The abrupt velocity recovery when exiting a pause is consistent with dissociation of the paused motors, which allows the motors to move forward without load at normal velocity.

We observed two types of cargo trajectories during pausing: static (Fig. 3.5 *C*) and dynamic (Fig. 3.5 *D-E*). During static pausing, which occurred with all 42 microtubules examined, cargo velocity remained unchanged at zero (Fig. 3.5 *C*). During dynamic pausing, which was observed for 10/42 microtubules, the cargo underwent substantial backward and forward movements while its net position remained approximately constant (backward and forward arrows, Fig. 3.5 *D-E*). Cargo velocity was 3-fold faster during backward movements than during forward movements (Fig. 3.5 *D-E*).

Backward movements are surprising, since only one type of motor was present to drive cargo transport. While it is formally possible that a bead dissociates from the microtubule briefly and rebinds, or that the bead rotates backward, allowing other motors to bind, neither scenario explains the asymmetry in cargo velocity during backward and forward movements (2.0 μm/s vs. 0.66 μm/s, Fig. 3.5 *D-E*). Instead, fast backward movements are consistent with cargo "flopping" back to the location of paused kinesins [37, 66] when the leading motor stochastically unbinds from the microtubule (Fig. 3.6). Slow forward movements are consistent with the rebinding of detached motors driving the cargo forward and being hindered by the paused motor(s) lagging behind. Occasionally, we detected somewhat slower backward movement (backward movement at ~17.5 s, Fig. 3.5 *E*) that may be due to successive unbinding of a few leading motors. The range of these backward movements is consistent with the flopping mechanism, given kinesin's contour length [36, 37] and our bead size (Fig. 3.6).

3C-vii. Surface effects are not responsible for cargo pausing in many-motor transport

Are surface effects responsible for pausing in many-motor transport? To address this possibility, we examined the off-axis position of cargos during pauses and during motion (Fig. 3.7). If a surface effect (for example microtubule supertwist) is the main cause of pausing, then beads should pause preferentially at the interface between the microtubule and its coverslip support. Extended travel in the many-kinesin system allowed us to determine the distribution of the off-axis positions for each bead trajectory

(Fig. 3.7 *A*). The range of off-axis position (~200 nm) is reasonable considering kinesin's contour length [36, 37] and our bead size (Fig. 3.8). Note that this approach was not

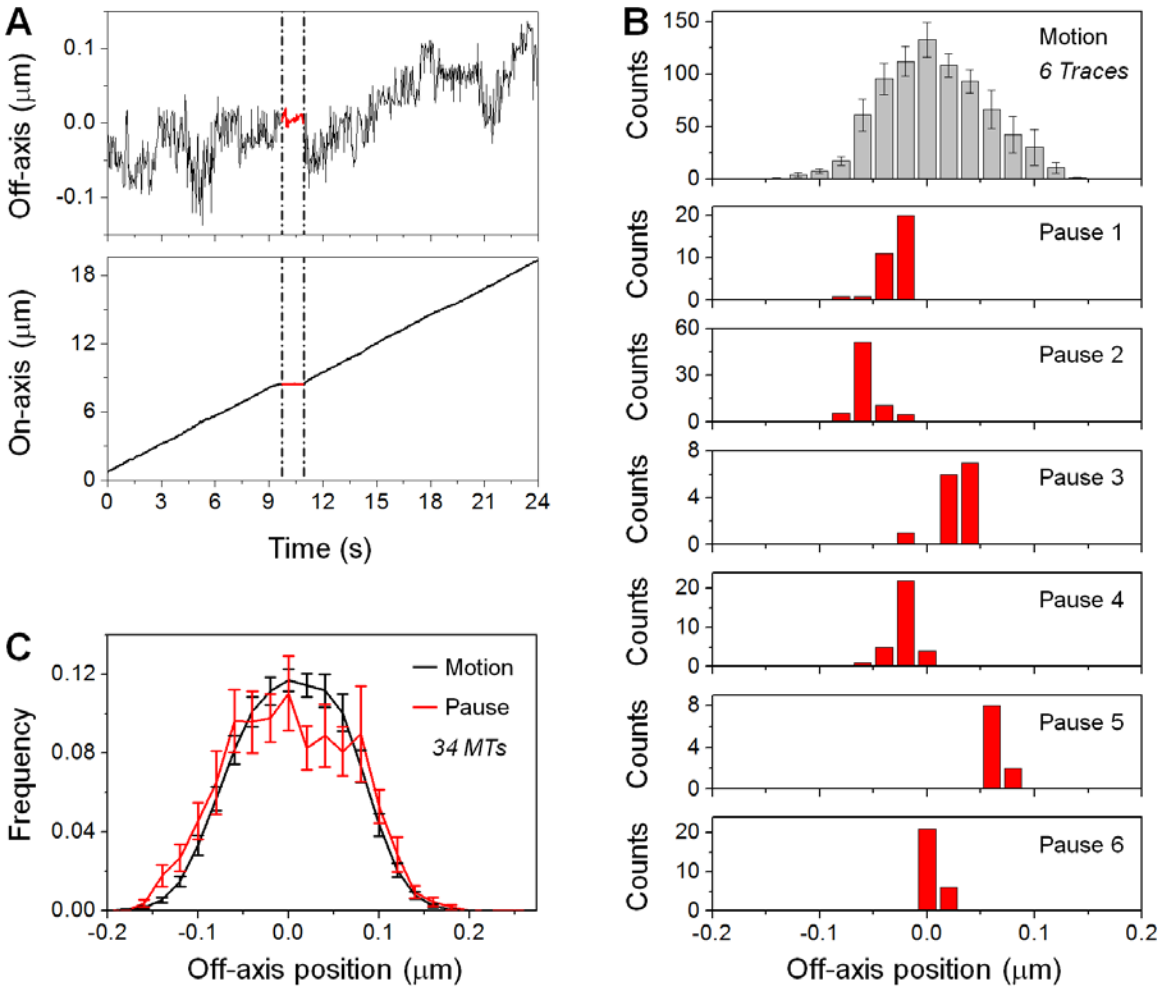

FIGURE 3.7. Distributions of off-axis positions of beads during pausing and during motion. (*A*) Example off-axis (top) and on-axis (bottom) positions for one bead trajectory. Vertical dash-dot lines indicate pausing. (*B*) Example distributions for six trajectories along the same microtubule. The distribution during cargo motion represents averages of all six trajectories; error bars, standard error. Distributions during cargo pausing were not averaged and represent individual trajectories. Pauses 1-3 shared the same on-axis location on the microtubule. Pause 6 corresponds to the off-axis trajectory shown in (*A*). (*C*) Normalized distributions averaged over 34 microtubules (MTs). Error bars, standard error.

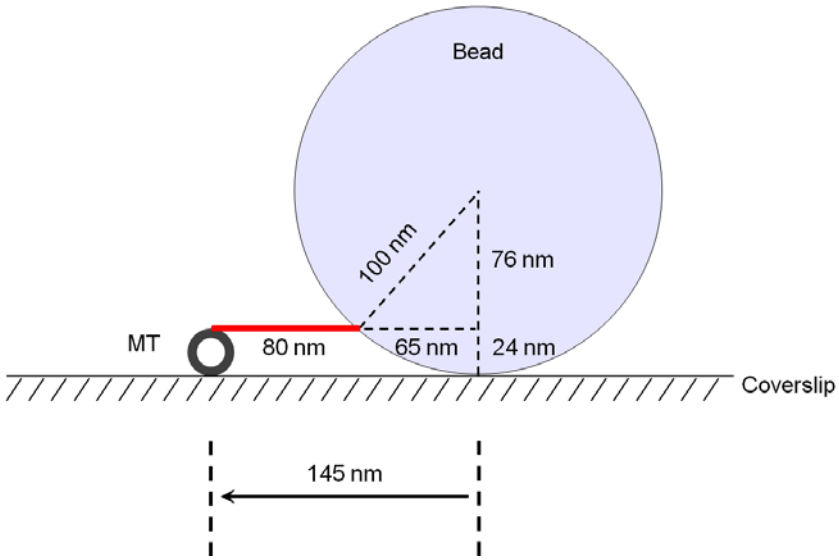

FIGURE 3.8. Possible range of off-axis cargo positions, given kinesin's contour length (80 nm [36, 37]) and our bead size (100 nm radius). Illustration is to scale. Red, kinesin. The range of off-axis positions observed in our study (~200 nm, Fig. 5 in the main text) is within this estimated range (290 nm) and is thus reasonable.

possible for the few-kinesin system because travel distances were too short to fully map the off-axis range of a microtubule. Some of the microtubules in our experiments underwent thermal motion relative to the coverslip support. Thus, to examine motor-based bead motion independent of thermal motion of the microtubule, we focused this analysis on the subset of 34 microtubules that were well anchored to the coverslip throughout the experiment.

We did not observe any tendency of beads to pause at the microtubule/coverslip interface (Fig. 3.7 *B*-*C*). For each microtubule, pauses did not occur at the same off-axis position (Fig. 3.7 *B*). For example, despite sharing a common on-axis location, pauses 1-3 differed significantly in their off-axis position (Fig. 3.7 *B*). Note that the constrained off-axis diffusion during pausing in Figure 3.7 *A* was not a general observation. When we pooled measurements from 34 microtubules, the distribution of off-axis positions during pausing was in excellent agreement with that during motion (red vs. black lines, Fig. 3.7 *C*). Both distributions were well described by a normal distribution (R_{adj}^2 = 0.95 and 0.99, respectively) that is centered about the mean off-axis position of the microtubule (0.3 ± 3.6 nm and 6.3 ± 1.6 nm, respectively). These analyses demonstrate that cargos did not preferentially pause at the microtubule/coverslip interface, indicating that surface effects

are not the main cause of pausing in our many-kinesin system. We repeated these results using antibody-elevated microtubules.

3C-viii. Pausing probability increases for microtubules with higher defect frequency

Next, we examined whether pausing probability was directly affected by the frequency of defects in microtubules. To isolate the effect of defect frequency on pausing, we used identical flow cells (polylysine-based) to harbor microtubules with different defect frequencies. We generated taxol-polymerized microtubules for comparison with taxol-stabilized microtubules (Materials and Methods). Arnal and Wade previously reported that the frequency of defects in a microtubule varies to some extent with microtubule-assembly conditions [37]. Specifically, the number of transitions in protofilament number within a microtubule is twice as high for taxol-polymerized microtubule as for the taxol-stabilized microtubules that we have described thus far [36]. We used a single population of tubulin dimers to keep the biochemical makeup of these two types of microtubules constant. We also used the same kinesin/cargo preparation and altered the measurement order of the microtubule types for each set of pairwise comparisons. Microtubule immobilization was achieved using the polylysine-based method. A total of 14 microtubule pairs were tested. Consistent with our observations with taxol-stabilized microtubules (Fig. 3.7), cargo pausing on individual taxol-polymerized microtubules did not occur at the same off-axis position, and surface effects were not the main cause of cargo pausing.

Importantly, we observed a significantly higher probability of pausing on microtubules with higher defect frequency (taxol-polymerized microtubules) for 4/14 pairwise comparisons (microtubule pairs 1, 8, 10, and 11, Fig. 3.9 *B*). We did not detect any instances in which a significantly higher pausing probability occurred for microtubules with lower defect frequency (taxol-stabilized microtubules). Overall, the paired-sample t-test indicated that pausing probabilities differed significantly between these two microtubule types ($P = 0.028$, Fig. 3.9 *B*). The mean pausing probability was 1.6 ± 0.3-fold larger for microtubules with a higher defect frequency (Fig. 3.9 *C*). When we calculated the ratio of pausing probability for each pairwise comparison, we uncovered an average 2.2 ± 0.6 higher likelihood of a trajectory pausing on taxol-polymerized microtubules (more defects) than on taxol-stabilized microtubules (fewer defects). These data indicate that microtubule defects were the dominant factor underlying cargo pausing in the many-motor system.

We observed similar trends in the number of pause locations along each microtubule axis. For 4/14 comparisons with significantly higher pausing probability for microtubules with more defects, the number of pause locations was more than 2-fold larger. We observed only one instance in which the number of pause locations was substantially (2-fold) higher for microtubules with lower defect frequency. Overall, the

paired-sample t-test demonstrated that the number of pause locations was substantially different between the two microtubule types (P = 0.055). The mean number of pause locations was 1.5 ± 0.3-fold larger for microtubules with higher defect levels. When we calculated the ratio of pause locations for each pairwise comparison, we detected an average of 2.0 ± 0.4 more pause locations on taxol-polymerized microtubules than on taxol-stabilized microtubules. These data are consistent with the previous finding that the frequency of defects in taxol-polymerized microtubules is twice that in taxol-stabilized microtubules [37].

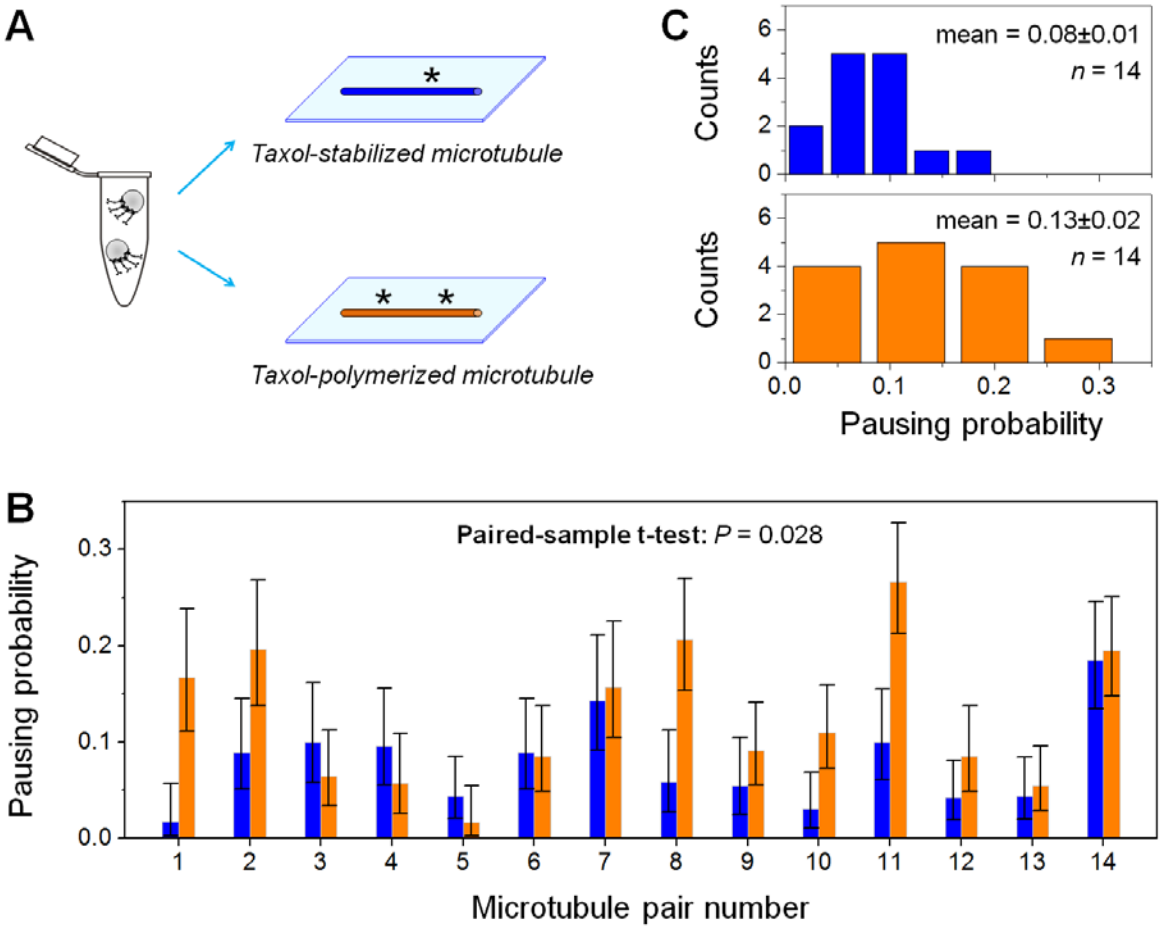

FIGURE 3.9. Probability of cargo pausing on microtubules with different defect frequencies. (*A*) Schematic of experimental setup (not to scale). A single population of kinesin-coated beads was introduced into two flow cells containing taxol-stabilized microtubules (blue) or taxol-polymerized microtubules (orange). Asterisks illustrate the relative defect frequencies as previously reported [60]. (*B*) Probability of a trajectory pausing on each microtubule. Error bars, standard error. (*C*) Distributions of pausing probability measured for each microtubule

type. Mean pausing probability (± standard error) and sample size (*n* microtubules) are indicated.

Taken together, our data demonstrate that cargo pausing is directly influenced by microtubule defects. As the number of defects in the microtubule increases, the probability that a cargo will pause along that microtubule also increases.

3D. Discussion

Here we used a single-microtubule assay to probe the functional importance of microtubule defects on kinesin-based transport in vitro. This approach differs from standard multiple-microtubule assays in that it specifies the microtubule for transport, thus yielding information about cargo transport as well as the "road condition" of the microtubule. Our data indicate that microtubule defects influence kinesin-based transport in vitro, prompting cargos to unbind from the microtubule (Fig. 3.2) or to pause during continuous motion (Fig. 3.5). Importantly, these effects were independent of the microtubule immobilization method; we observed cargo unbinding and pausing for both polylysine-supported microtubules (Figs. 3.2 and 3.5) and antibody-supported microtubules (Figs. 3.4).

We did not detect a significant role of surface effects on cargo unbinding (Figs. 3.3 and 3.4) or pausing (Figs. 3.7). We also observed significantly more cargo pausing on microtubules with more defects (Fig. 3.9), indicating that the main factor determining cargo pausing is microtubule defects, not experimental artifacts. Note that measurements from our few-motor study in Figure 3.3 do not conflict with a previous report of a somewhat shorter single-kinesin travel distance along GMPCPP microtubules than along taxol-stabilized microtubules [60]. Kinesin has a 3.7-fold higher binding affinity for GMPCPP microtubules than for taxol-stabilized microtubules [60]. Travel distance in the few-motor system is sensitive to both the binding and unbinding events of individual motors with the microtubule [40], and need not reflect the trend of single-motor travel.

How do microtubule defects cause cargo unbinding and pausing? Microtubule defects include missing tubulin dimers [79, 80] and changes in the number of protofilaments within a microtubule [40, 63]. Previous studies demonstrated that kinesins require successive tubulin dimers to sustain transport [62]. We thus propose that the main effect of a missing tubulin dimer is to prompt kinesin to unbind from the microtubule. Kinesins also tend to pause in crowded environments [59, 66, 81]. A change in protofilament number leads to the merging of two or more protofilaments into one "lane" when the transition occurs in the direction of kinesin transport. Kinesins that track merging protofilaments likely crowd into a "traffic jam" at the merging site. We therefore

propose that the main effect of protofilament merging is to cause a subset of motors to pause at the merging site, hindering cargo transport.

Our model accounts for our finding that the effects of microtubule defects strongly depend on the number of motors available for transport (Figs. 3.2 and 3.5). For the few-kinesin system, the number of motors available to create a traffic jam is limited, but each cargo is more sensitive to the unbinding of individual motors. The effect of individual motor unbinding is suppressed in the many-kinesin system, but more motors track the merging protofilaments and can contribute to a traffic jam. We are working on future methods to generate microtubules that preferentially express each of these two defect types.

The effects uncovered in our study may have physiological relevance in vivo. These local changes in transport (shorter travel distance or slower velocity) may have downstream consequences for cellular functions that rely on proper cargo transport. The magnitude of this impact remains unknown, since various microtubule-associated proteins decorate microtubules and may obscure these defects from cargo transport in vivo. However, there is evidence that the structure of microtubules is tightly regulated in cells. The microtubule-severing protein katanin targets and removes microtubule defects [66, 82], and the microtubule-associated proteins doublecortin and EB1 preferentially stabilize microtubules with 13 protofilaments [83-85]. Our study raises the intriguing possibility that an important function of these machineries may be to maintain “road conditions” for cargo transport in vivo.

Chapter 4. Effect of Microtubule Biochemical State on Kinesin-Based Transport [22]

4A. Introduction

Molecular motor-based transport is sensitive to the run length of cargos along microtubules. Because molecular motors often work in small teams to shuttle cargos in cells [22, 47, 57, 61, 64, 65, 86], understanding the key factors impacting multiple motor-based transport is crucial for understanding and ultimately harnessing transport regulation in cells. There is increasing evidence that the biochemical nature of tubulin plays a key role in regulating motor-based transport [79, 86-97]. In the current study, we examined the impact of the nucleotide state of the tubulin subunits within microtubules on multiple-kinesin based transport.

Our study was motivated by a previous finding that kinesin-1 preferentially binds

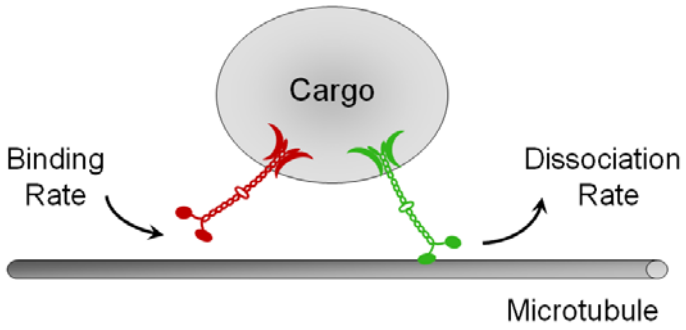

FIGURE 4.1. The run length of multiple-motor cargos is sensitive to both the binding and dissociation rates of individual motors for the microtubule. The illustration is not to scale. For simplicity, we depict two representative motors during cargo transport. During transport, the bound motor (green) can dissociate from the microtubule. The greater the dissociation rate, the smaller the number of motors linking the cargo to the microtubule, and the shorter the cargo's run length. At the same time, an unbound motor (red) can bind the microtubule and engage in transport. The greater the motor's binding rate, the faster the unbound motor rebinds the microtubule. This effect increases the net number of motors linking the cargo to the microtubule at any time, thereby increasing the overall run length of the cargo. Previous reports indicate a substantially higher (3.7x) binding affinity of kinesin-1 for GMPCPP

microtubules versus GDP microtubules [98]. In the current study, we examined the implication of such an increase in kinesin's binding affinity for the run length of multiple-kinesin cargos.

GTP-tubulin-rich microtubules [99]. Depending on the concentration of motors present in solution, the binding affinity of a single, cargo-free kinesin can be up to ~3.7x higher for GMPCPP microtubules (mimicking GTP-tubulin [100]) than for GDP microtubules [79]. This effect was proposed to underlie polarized transport in axons [101], by promoting preferential loading of kinesin-based cargos onto the axon initial segment, where microtubules are enriched in GTP-tubulin [79]. Because binding affinity is a key determinant of multiple-motor transport [79, 97] (Fig. 4.1), we anticipated that the run length of multiple-kinesin cargos would be significantly longer for GMPCPP microtubules than for GDP microtubules. Such a run-length increase in the kinesin-based anterograde direction has the potential to further promote polarized transport in axons.

Here, we used optical trap-based biophysical studies to test the hypothesis that the run length of multiple-kinesin cargos is enhanced for GTP-tubulin-rich microtubules. As in previous work [79], we used GMPCPP microtubules to model microtubules enriched with GTP-tubulin, as well as standard GDP microtubules as controls. We verified that GMPCPP microtubules are stable at room temperature without the stabilizing agent taxol (Fig. 4.2). Because the presence of an oligo-histidine tag has been shown to significantly increase the binding affinity of the end-binding protein EB1 for GMPCPP microtubules [102, 103], we focused on native kinesin motors lacking affinity purification tags. To purify the tagless, native kinesin motor, we employed the classic microtubule-affinity-based purification method [46], with the exception that 9S kinesin was eluted from the Mono-Q resin using a series of customized salt gradients to isolate the motor from other polypeptides in the 9S sucrose fractions [103, 104]. We used standard polystyrene beads as our in vitro cargos [46] to quantify multiple-kinesin run length, and controlled the range of motor number per cargo as we did previously [24, 26, 41, 105]. Note that binding of native kinesin-1 to the in vitro cargo relieves the motor from tail-mediated autoinhibition and enables motor-based cargo motility [24, 106].

Surprisingly, we did not detect a significant difference in the run lengths of multiple-kinesin cargos between GMPCPP microtubules and GDP microtubules. Our single-motor measurements also demonstrated similar dissociation rates and velocities for both microtubule types. Combined, our data suggest that kinesin has similar binding rates for both microtubule types. To test the validity of this surprising, biophysics-based finding, we biochemically probed the binding affinity of the native motor using a classical microtubule-affinity pulldown assay [41]. Our pulldown data confirmed that native kinesin-1 does not preferentially bind microtubules enriched in GTP-tubulin.

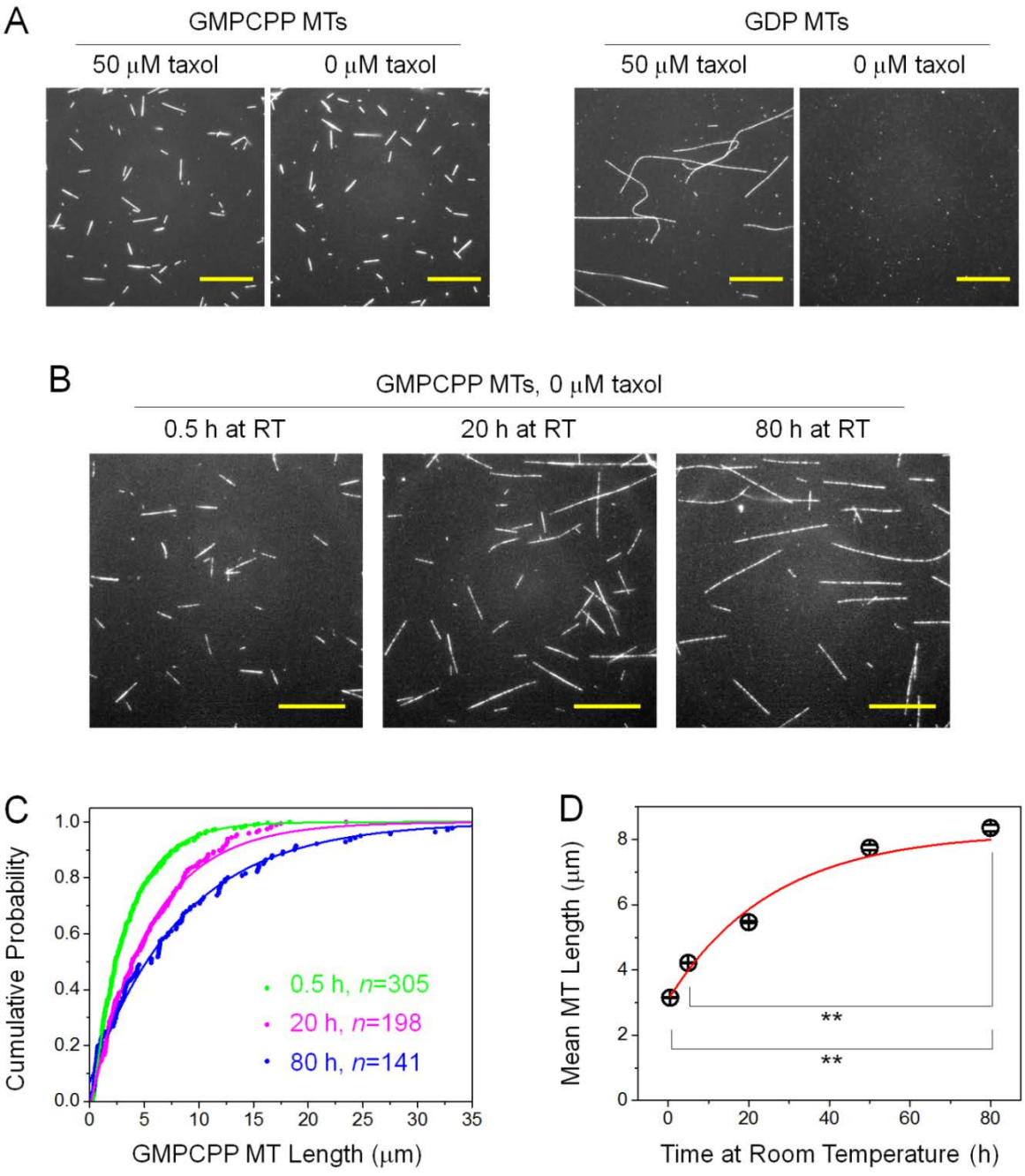

FIGURE 4.2. GMPCPP microtubules (MTs) are stable at room temperature without the stabilizing agent taxol. (*A*) Representative fluorescence images of GMPCPP MTs and GDP MTs in the absence and in the presence of taxol. MTs for each condition were imaged within 10 min of being moved from a 37 °C water bath to room temperature (RT). Scale bar, 20 μm. (*B*) Representative fluorescence images of taxol-free GMPCPP MTs that were kept at RT for the indicated time in the absence of taxol. Scale bar, 20 μm. (*C*)

Cumulative probability distributions of MT lengths corresponding to conditions in (B). *n*, sample size. Solid lines, best fits to $1\text{-}Ae^{-x/L}$, where *L* is the mean MT length. (*D*) Mean length of taxol-free GMPCPP MTs (scatters ± standard error) as a function of the time kept at RT. Red line, exponential growth trend. $^{**}P \leq 0.022$, rank-sum test.

4B. Materials and methods

4B-i. Proteins and reagents

Bovine brain tubulin, kinesin-1 and 9S kinesin were prepared as described in Chapter 2B-i. Rhodamine-labeled tubulin (TL590M) was purchased from Cytoskeleton Inc. Unless otherwise specified, chemicals were purchased from Sigma-Aldrich. GMPCPP was purchased from Jena Biosciences.

4B-ii. Microtubule preparation

Taxol-stabilized GDP microtubules were prepared as described in Chapter 2B-i.

To assemble GMPCPP microtubules, purified tubulin was diluted to 4 μM in PM buffer supplemented with 1 mM GMPCPP. The resulting tubulin solution contained 125x excess of GMPCPP (1 mM) to GTP (8 μM). Because the affinity of tubulin for GMPCPP is >1/8 of its affinity for GTP [107], we estimate that the resulting microtubules were enriched in GMPCPP tubulin (>15x excess over GDP tubulin). The tubulin solution was incubated at 37 °C for 0.5 h or 2.5 h for assembly. The shorter condition was used in tests of the stability of GMPCPP microtubules. The microtubules were then kept at room temperature and in a dark box for up to 80 h. The longer condition was used to achieve longer GMPCPP microtubules for motility measurements. With the exception of the stability test, GMPCPP microtubules were freshly prepared each day and used immediately following preparation.

For epifluorescence-based length quantification, both types of microtubules were fluorescently labeled at a ratio of 1:10 rhodamine-labeled tubulin:unlabeled tubulin.

4B-iii. Quantification of microtubule length

The length of microtubules was used as a readout for microtubule stability under different conditions. Measurements were carried out in standard flow cells that were prepared identically for different microtubule conditions. To construct each flow cell, we sandwiched a coverslip (22x40 mm, No. 1.5, Thermo Fisher Scientific) and a microscope

slide (25x75 mm, Thermo Fisher Scientific) using double-sided tape. The coverslip and the microscope slide were biologically clean. Kinesin was diluted to 65 nM in PMEE buffer (35 mM PIPES, 5 mM $MgSO_4$, 1 mM EGTA, 0.5 mM EDTA, pH 7.2) and then introduced to the flow cell for 10 min to undergo nonspecific binding to the flow-cell surface. Casein (5.55 mg/mL in PMEE buffer) was introduced to the flow cell for 10 min to wash out excess unbound motors and to block the flow-cell surface. Microtubules (GMPCPP or GDP) were diluted in PMEE buffer (supplemented with 0 μM taxol or 50 μM taxol as indicated), introduced to the flow cell for 10 min, and imaged at 100x magnification via epifluorescence microscopy (Eclipse Ti-E, Nikon; and iXon electron multiplier CCD, Andor). Images were exported from Nikon Elements as .tif files and imported into MatLab (MathWorks) for analysis. Microtubule length was quantified to ~10 nm resolution using Fluorescence Image Evaluation Software for Tracking and Analysis (FIESTA, version 1.05.0005) [106].

4B-iv. Optical trapping-based motility assay

In vitro motility experiments were carried out in flow cells, which were prepared identically for GDP and GMPCPP microtubules. Flow cells were constructed as were prepared as described in Chapter 3B-iii.

Flow cells with GDP microtubules were prepared as described in Chapter 3B-iii.

To make flow cells with GMPCPP microtubules, we used the same procedures as above, except that the GMPCPP microtubules were diluted to 40 nM and GTP was excluded from all buffers. Buffers contained 0 μM or 25 μM taxol as indicated.

For the multiple-motor measurements, kinesin (2.5-3.3 nM) was incubated with carboxylated polystyrene beads (4.5×10^6 particles/μL, 200 nm diameter, Polysciences) as described in Chapter 3B-iv. We verified that cargo transport was mediated by multiple kinesins, because the average cargo run length was substantially higher than that of the single-kinesin value. To eliminate potential variations in kinesin/bead ratio between preparations, we used the same kinesin/bead preparation to contrast between microtubule types and repeated our experiments 3-4 times for each set of pairwise comparisons.

For the single-motor studies, kinesin (0.1-0.17 nM) was incubated with carboxylated polystyrene beads (3.6×10^5 particles/μL, 500 nm diameter, Polysciences) in motility buffer for 10 min at room temperature, supplemented with an oxygen-scavenging solution and 1 mM ATP prior to motility measurements. At this motor/bead incubation ratio, ≤20% of the motor/bead complexes exhibited motility along microtubules, and >95% of the motile events were carried by a single kinesin [5, 101].

A single-beam optical trap was used to facilitate motility measurements as previously described [5]. We used a very weak trap power (<20 mW at fiber output),

such that the trap was sufficient for positioning individual beads but could not stall beads carried by a single kinesin [26]. We also turned off the optical trap upon observation of directed bead motion along the microtubule to enable cargo transport without external load.

Video recordings of bead motion (30 Hz) were particle-tracked to 10 nm resolution (1/3 pixel) using a template-matching algorithm as previously described [5, 26].

4B-v. Analysis of in vitro motility data

The run length of a motile bead was determined in the same way described in chapter 2B-v. For each experimental condition (kinesin/bead incubation ratio, microtubule type), the cumulative probability distribution of run length was fitted to the cumulative probability function of a single exponential distribution, $1-Ae^{-x/d}$. Mean run length and standard error for each distribution were determined from the best-fit decay constant *d* and uncertainty, respectively.

To evaluate bead velocity under no load, only portions of each trajectory >300 nm were used. For each microtubule type (GDP or GMPCPP), the cumulative probability distribution of single-kinesin velocity was fitted to the cumulative probability function of a Gaussian distribution, $\frac{1}{2}\left[1+erf\left(\frac{x-v}{A}\right)\right]$. Mean velocity and standard error for each distribution were determined from the best-fit mean *v* and uncertainty, respectively.

The association time of a single-kinesin bead with the microtubule was determined as the time between landing and dissociation. To account for human reaction time during manual shut-off of the optical trap, only trajectories >0.3 s were analyzed. For each microtubule type, the cumulative probability distribution of the association time was fitted to the cumulative probability function of a single exponential distribution, $1-Ae^{-x/t}$. Mean association time and standard error for each distribution were determined from the best-fit decay constant *t* and uncertainty, respectively.

4B-vi. Microtubule affinity pulldown assay

Kinesin (66 nM) was incubated with 1.1 μM GDP microtubules in PMEE buffer (supplemented with 25 μM taxol and 5 mM AMPPNP or 5 mM ATP as indicated) or ~1.7 μM GMPCPP microtubules in PMEE buffer (taxol-free, supplemented with 5 mM AMPPNP or 5 mM ATP as indicated). Assays using ATP were supplemented with an ATP-regenerating system (2 mM phosphocreatine and 70 μg/mL creatine phosphokinase) [26]. Kinesin/microtubule mixtures were identically incubated at 37 °C for 25 min, followed by centrifugation in a TLS55 rotor for 10 min at 170,000 x *g* at 25 °C. The

resulting pellets were dissolved in 40 uL 1x reducing SDS sample buffer (Thermo Fisher Scientific), heated to 80 °C for 10 min, and separated via SDS-PAGE (4-12% Bis-Tris protein gel, NuPAGE, Thermo Fisher Scientific). Gels were imaged in near infrared (700 nm) using a commercial scanner (Odyssey, Li-Cor Biosciences).

4B-vii. Statistical analysis

The rank-sum test was used to detect significant differences between two distributions of run-length measurements. Student's *t*-test was used to determine the significance of differences between two distributions of velocity measurements and between two sets of co-sedimentation measurements.

4C. Results and discussion

4C-i. The presence of taxol does not impact the motility of multiple-kinesin cargos along GMPCPP microtubules

We first controlled for the potential effect of taxol on cargo transport along GMPCPP microtubules (Fig. 4.3). Although taxol is not needed to stabilize GMPCPP microtubules, it is necessary to stabilize GDP microtubules (Fig. 4.2 A). Previous studies indicated that the presence of taxol does not influence the motility (run length or velocity) of single kinesins along GMPCPP microtubules [108], nor does taxol influence the multiple kinesin-based gliding velocity of GMPCPP microtubules in vitro [108]. However, these previous investigations used truncated kinesin-1 constructs, not the native kinesin-1 employed here. We carried out parallel motility experiments using identical, taxol-free preparations of GMPCPP microtubules and kinesin/bead complexes, while varying the taxol content in buffers used in flow-cell preparation and subsequent motility experiments (0 μM or 25 μM, Fig. 4.3).

We focused our investigations on transport by an average of ~2 kinesins per cargo, which matches the range reported for kinesin-based cargos in vivo [57, 64]. Although quantitative control over motor number per cargo remains an active area of research, we and others previously characterized the run length of cargos carried by exactly two kinesins (via DNA- or protein-based assembly; [27, 41, 43, 68, 69]). Specifically, we and others demonstrated that the average run length of two-kinesin cargos is ~1.7x longer than the single-kinesin value [41, 68]. Here, we used this known scaling of two-kinesin run length as a "scale bar", and empirically tuned the kinesin/bead ratio such that the resulting cargo run length displayed a similar increase from the single-kinesin value.

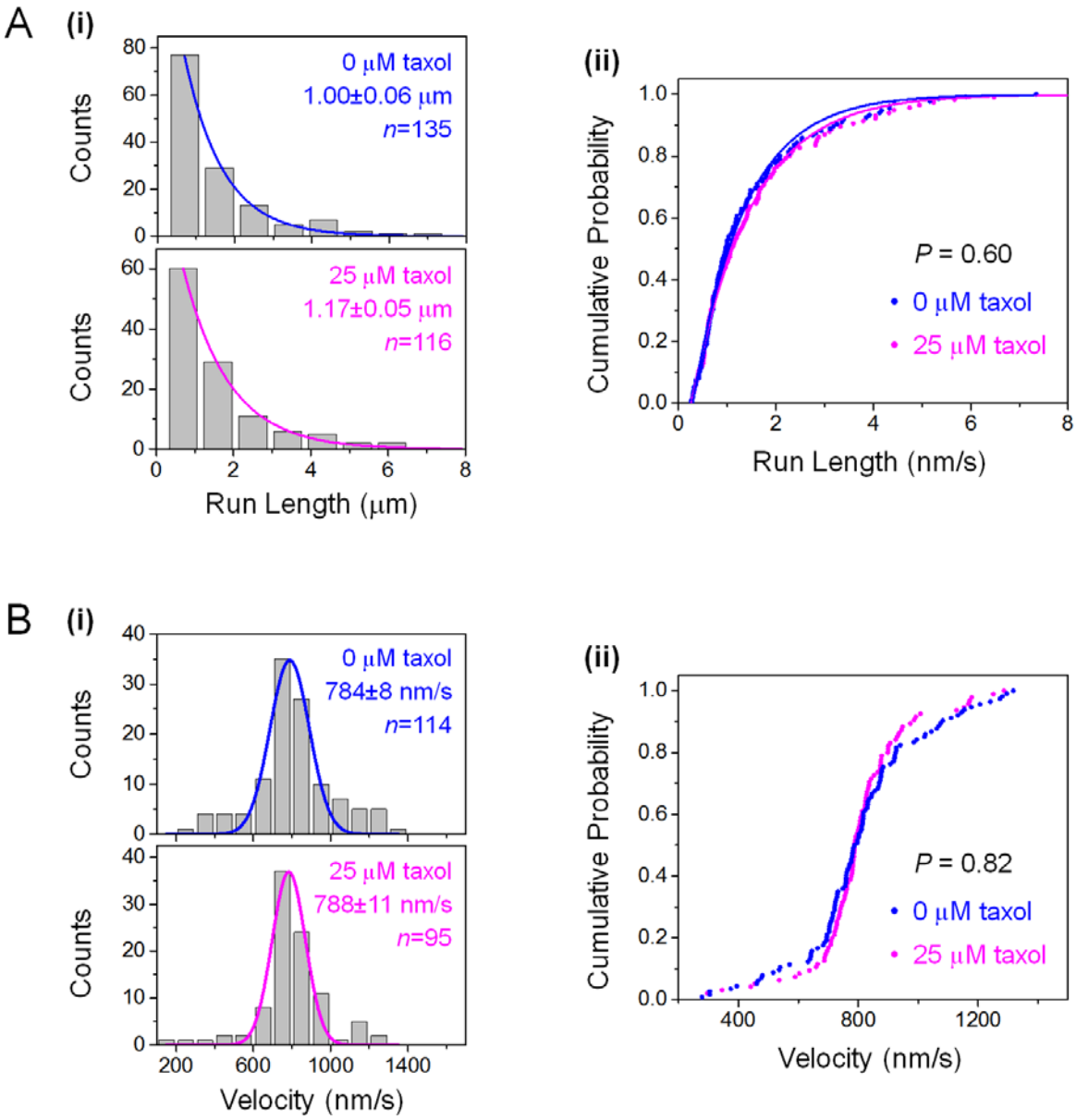

FIGURE 4.3. The presence of taxol in motility experiments does not influence the motility of multiple-kinesin cargos along GMPCPP microtubules. GMPCPP microtubules were assembled in the absence of taxol. Taxol concentrations during motility experiments are indicated. (*A*) Histograms (i) and cumulative probability distributions (ii) of cargo run length along GMPCPP microtubules, in the presence (blue) and the absence (magenta) of taxol. Solid lines, best fits to a single exponential distribution, $e^{-x/d}$. Mean run length (d ± standard error) sample size (n) are indicated. The run length distributions do not differ significantly from each other (P = 0.60, rank-sum test). (*B*) Histograms (i) and cumulative probability distributions (ii) of cargo velocity

along GMPCPP microtubules, in the presence (blue) and absence (magenta) of taxol. Solid lines, best fits to a Gaussian distribution. Mean velocity (± standard error) and sample size (*n*) are indicated. The velocity distributions do not differ significantly from each other ($P = 0.82$, Student's *t*-test).

We did not detect any significant effect of taxol on cargo run length along GMPCPP microtubules (Fig. 4.3 A). Although the mean run length along taxol-free GMPCPP microtubules was somewhat shorter than that in the presence of taxol (1 μm vs. 1.17 μm, Fig. 4.3 A(i)), this difference was not statistically significant ($P = 0.60$, rank-sum test, Fig. 4.3 A(ii)). The lack of difference in cargo run length was evident when we contrasted the cumulative probability distributions of the same measurements (Fig. 4.3 A(ii)). For longer run lengths, the cumulative probability distribution also highlighted subtle deviations from a single exponential (scatter vs. line, Fig. 4.3 A(ii)). Deviation from a single exponential is expected for multiple-motor measurements, whose distribution is better approximated by a sum of multiple single exponentials [28, 41]. Importantly for the current study, such deviation does not impact our ability to determine the significance of differences between measurements using the rank-sum test ($P = 0.60$, Fig. 4.3 A(ii)). We also did not detect any significant effect of taxol on the transport velocity of cargos along GMPCPP microtubules ($P = 0.82$, Student's *t*-test, Fig. 4.3 B). These results are in excellent agreement with previous studies of truncated kinesin-1 constructs in single-motor motility assays [68] or microtubule gliding assays [28].

Taken together, our data demonstrate that the presence of taxol in motility experiments does not influence kinesin-based motility on GMPCPP microtubules.

4C-ii. The run length of multiple-kinesin cargos does not differ significantly between GMPCPP and GDP microtubules

We next carried out parallel comparisons of multiple-kinesin run length along GMPCPP microtubules and GDP microtubules (Fig. 4.4). To eliminate potential variations in kinesin/bead ratio between preparations, we used a single kinesin/bead preparation for each set of pairwise comparisons between microtubule types. Because the presence of taxol does not impact kinesin-based cargo motility along GMPCPP microtubules (Fig. 4.3, and [109, 110]), we included taxol in our kinesin/bead preparations as well as in all buffers used in our motility experiments.

Surprisingly, we did not detect any significant difference in the run length of ~two-kinesin cargos between microtubule types ($P = 0.60$, rank-sum test, Fig. 4.4 A(i)). For this set of measurements, we used the same kinesin/bead ratio as in Fig 4.3 (~two-kinesin transport range). We speculated that more motors may be necessary to achieve our experiments. As a result, the associated cargo run length increased substantially (from

1.38 µm in Fig. 4.4 A(i) to 3.31 µm in Fig. 4.4 A(iii), GDP microtubules). The deviation of measurements from a single exponential at the longer run lengths became more pronounced (scatter vs. line, Fig. 4.4 A), again indicating an increase in the number of motors per cargo. At the highest kinesin/bead ratio, the average run length was 4.4x

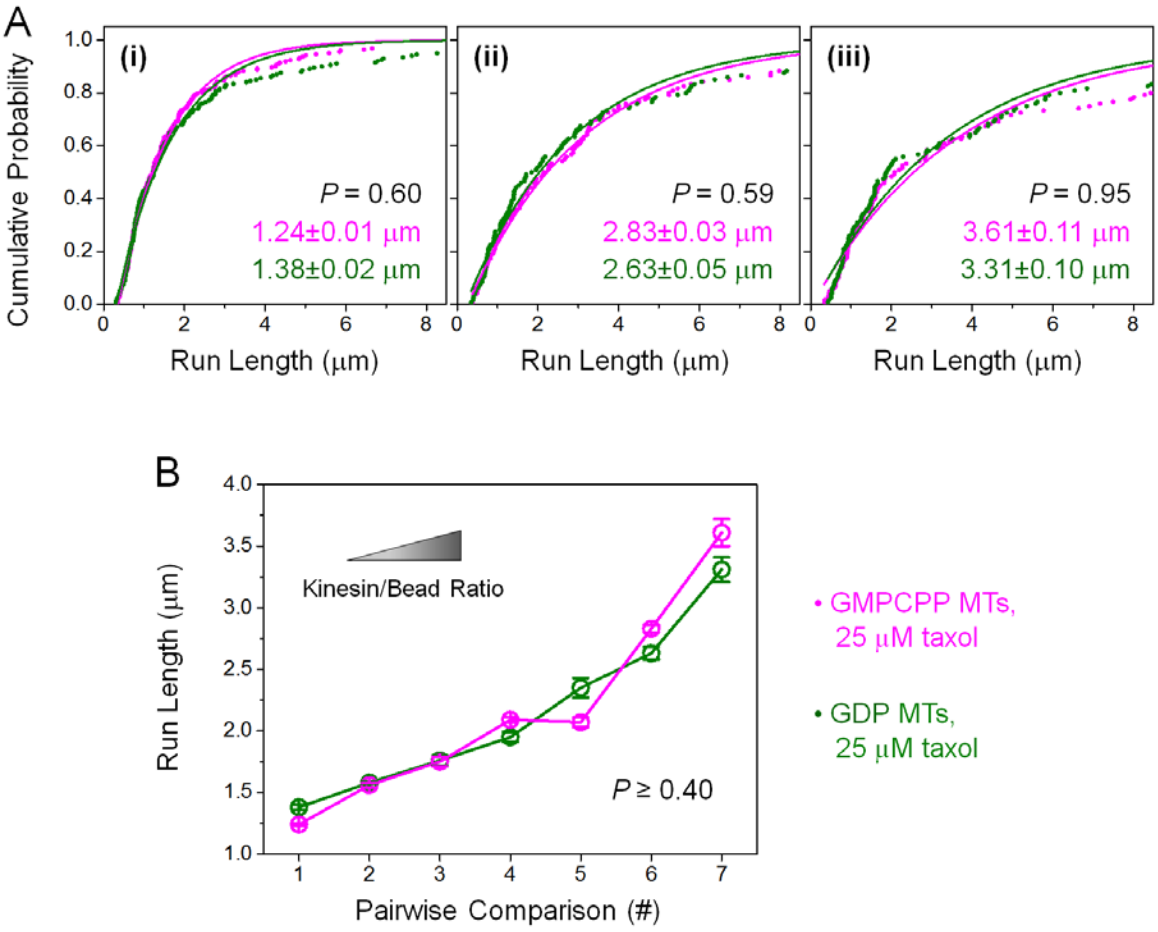

FIGURE 4.4. The run length of multiple-kinesin cargos does not differ significantly between GMPCPP and GDP microtubules (MTs). Taxol (25 µM) was present in buffers during motility experiments for both MT types. (*A*) Cumulative probability distributions of the run length of multiple-kinesin cargos, shown for three kinesin/bead ratios. Solid lines, best fits to $1\text{-}Ae^{-x/d}$. Mean run length (d ± standard error) and P-value (rank-sum test) are indicated (n = 119-222). (*B*) Average run length of multiple-kinesin cargos (± standard error), measured for seven kinesin/bead ratios (n = 89-222). Pairwise comparisons #1, #4, and #7 correspond to run-length measurements in (i), (ii), and (iii) of panel (*A*). The distributions in each set of pairwise comparisons do not differ significantly from each other ($P \geq 0.40$, rank-sum test).

longer than that of single-motor transport. This extended run length corresponds to transport mediated by ~3-4 motors per cargo, based on previous investigations of transport by a well-defined number of kinesin motors [27, 43, 69]. We did not further increase the kinesin/bead ratio, because the differential binding effect diminishes atthe difference in run length that we predicted. In principle, the more motors present on a cargo, the greater the cumulative effect of a change at the single-motor level (such as increased binding affinity) on overall cargo transport. To test this possibility, we increased the average number of motors per cargo by tuning up the kinesin/bead ratio in higher motor concentrations [27, 69]. Nonetheless, despite a substantial increase in the number of motors per cargo, we did not detect any significant difference in cargo run length between microtubule types (for example, Fig. 4.4 A). The mean run lengths for each pairwise comparison agreed well with each other (within 12%, Fig. 4.4 B). The corresponding distributions of run length also did not differ significantly from each other ($P \geq 0.40$, rank-sum test, Fig. 4.4 B). Thus, in contrast to our prediction, the run length of multiple-kinesin cargos is not significantly enhanced along GTP-tubulin-rich microtubules.

4C-iii. The dissociation rate of a single kinesin does not differ between GMPCPP and GDP microtubules

To understand the lack of difference in multiple-kinesin run length (Fig. 4.4), we sought to determine whether the dissociation rate of a single kinesin differs between microtubule types. The run length of multiple-motor cargos is sensitive to the motor's dissociation rate as well as its binding rate [32, 41, 43, 111] (Fig. 4.1). The null effect on multiple-motor run length in Figure 4.4 may reflect compensatory effects between changes in the motor's binding and dissociation rates for GTP-tubulin-rich microtubules. Whereas a substantial increase in the motor's binding rate can significantly improve multiple-motor run length, this effect may be countered by a similar increase in the motor's dissociation rate.

We carried out single-molecule measurements to determine the average association time between single-kinesin cargos and microtubules. We then used the reciprocal of this association time to determine the dissociation rate. We continued to use polystyrene beads as in vitro cargos, as in classic single-molecule experiments [5, 32]. To reach the single-motor range, we limited the kinesin/bead ratio such that <20% of the beads displayed motility along microtubules. We and others have previously demonstrated that, for a motile fraction <20%, most motile beads (>95%) are carried by a single kinesin [5, 105]. For consistency, we again included taxol in all buffers in our motility experiments for both microtubule types.

We did not detect any significant difference in kinesin's association time between microtubule types ($P = 0.50$, rank-sum test, Fig. 4.5 A). The mean association time remained ~1 s for both microtubule types (Fig. 4.5 A), giving rise to a dissociation rate of

~1 s^{-1} for both microtubule types (Fig. 4.5 B). It is important to note that kinesin's dissociation rate may be different in a multi-motor context, as associated motors on the cargo may influence the microtubule's interaction with dissociated motors on the same cargo. Nonetheless, our data indicate that the single-kinesin dissociation rate is not substantially influenced by the nucleotide state of tubulin. Thus, the lack of difference in multiple-kinesin run length (Fig. 4.4) is unlikely to result from compensatory changes in the motor's binding and dissociation rates for different microtubule types.

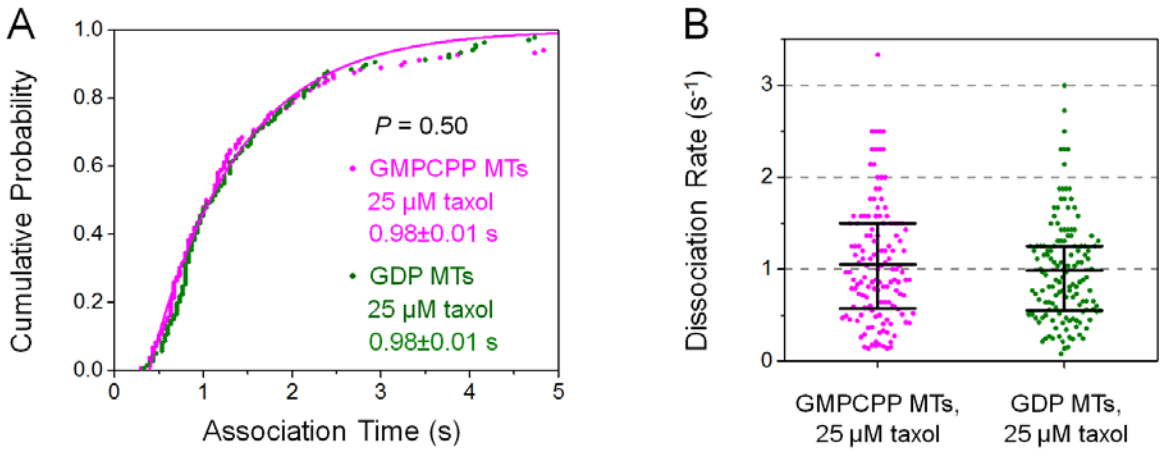

FIGURE 4.5. The dissociation rate of a single kinesin does not differ significantly between GMPCPP and GDP microtubules (MTs). Taxol (25 μM) was present in buffers during motility experiments for both MT types. (*A*) Cumulative probability distributions of the association time of single kinesins with GMPCPP MTs (n = 136) and GDP MTs (n = 138). Solid lines, best fits to $1-Ae^{-x/t}$. Mean association time (t ± standard error) is indicated. The two best-fit solid lines share the same average association time and thus overlap with each other. These distributions do not differ significantly from each other (P = 0.50, rank-sum test). (*B*) Dot plot of single-kinesin dissociation rate for each microtubule type, calculated as the reciprocal of the association time in (A). Horizontal bars indicate mean values and quartiles. These two distributions do not differ significantly from each other (P = 0.50, rank-sum test).

4C-iv. Comparison with theory suggests that the single-kinesin binding rate is similar for GMPCPP and GDP microtubules

We next referred to previous theoretical work [5] in order to examine the possibility that parameters other than single-motor dissociation rate underlie our null finding in Figure 4.4. Although this previous model does not consider force-based

interactions between individual motors, for kinesin-based transport, this model's predictions are in good agreement with results from stochastic simulations that include force-based interactions between motors [5] as well as with results from previous experimental studies employing GDP microtubules [28, 41].

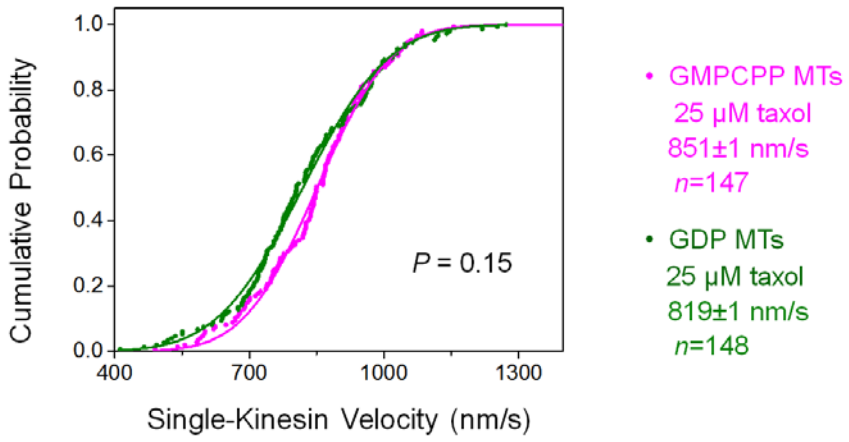

FIGURE 4.6. The velocity of single-kinesin cargos does not differ significantly between GMPCPP and GDP microtubules (MTs). Taxol (25 µM) was present in motility measurements for both MT types. Solid lines, best fits to the cumulative probability distribution of a Gaussian distribution. Mean velocity (± standard error) and sample size (*n*) are indicated. These two distributions do not differ significantly from each other (P = 0.15, Student's *t*-test).

Four key parameters are highlighted to impact cargo run length in previous theoretical work [111]: motor number, single-motor binding rate, single-motor dissociation rate, and single-motor velocity. Because we used the same kinesin/bead preparation to contrast between microtubule types, the number of motors available for transport did not differ between GMPCPP and GDP microtubules. We also detected very similar transport velocities of single kinesins along both microtubule types (P = 0.15, Student's *t*-test, Fig. 4.6), as did a previous single-motor study using a truncated kinesin dimer [41]. Note that we detected a modest (~7%) but significant velocity difference in our multiple-kinesin measurements (P = 0.004, Student's *t*-test, Fig. 4.7), consistent with previous multiple kinesin-based investigations of microtubule gliding velocities (~30% faster for GMPCPP vs. GDP microtubules) [28, 97] and suggesting a potential effect of motor number on cargo velocity.

Given that motor number, single-motor velocity, and single-motor dissociation rate are very similar between microtubule types, the binding rates of the motor should be very similar as well. However, this prediction is inconsistent with previous reports that kinesin preferentially binds GMPCPP versus GDP microtubules [80, 110]. It is possible that measurement uncertainties for individual parameters may combine to obscure a substantial effect of the motor's binding affinity on cargo run length. It is also possible that the force-based interaction between motors (not included in the theoretical model) could be altered by the nucleotide state of tubulin in microtubules. Lastly, although extensive in vitro studies suggest that this is unlikely [5, 48, 79], it is formally possible that polystyrene beads may alter the interactions between the motor and the microtubule in unexpected ways. Since it is challenging to completely rule out these potential concerns in biophysics-based assays, we next turned to a biochemistry-based assay.

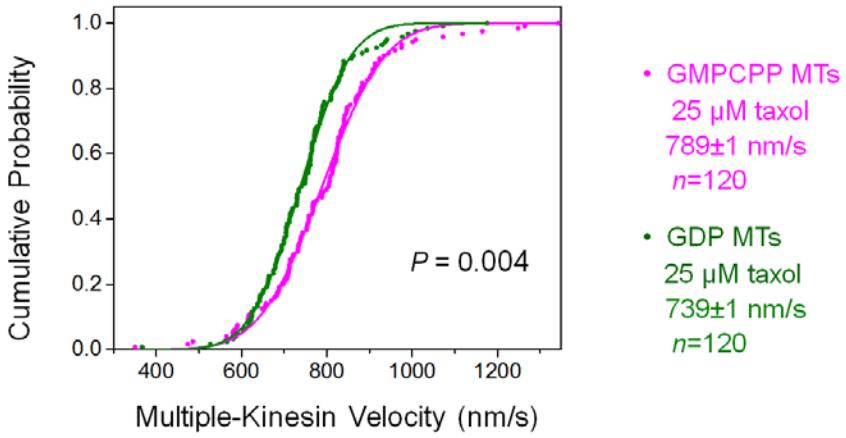

FIGURE 4.7. The velocities of multiple-kinesin cargos have a significant but small difference between GMPCPP and GDP microtubules (MTs). Taxol (25 µM) was present in motility measurements for both MT types. These velocity measurements correspond to run-length measurements in Figure 4.4 *A*(iii). Solid lines, best fits to the cumulative probability distribution of a Gaussian distribution. Mean velocity (± standard error) and sample size (*n*) are indicated. For both MT types, the velocities of multiple-kinesin cargos are somewhat lower than that of single-kinesin cargos shown in Figure 4. This reduction in velocity with increasing motor number per cargo is consistent with recent in vitro findings by ourselves [5] and others [66]. Mean velocity of multiple-kinesin cargos was 1.07x faster on GMPCPP MTs than on GDP MTs (P = 0.004, Student's t-test).

4C-v. Native kinesin-1 does not preferentially co-sediment with GTP-tubulin-rich microtubules

To overcome the uncertainties associated with our biophysical assays, we employed the classic microtubule affinity pulldown assay [48] to biochemically probe the binding of native kinesin-1 to microtubules (Fig. 4.8). Results from this co-sedimentation assay are bead-independent and free from considerations of force-based interaction between motors. Briefly, we incubated kinesins with microtubules, prior to pelleting the microtubules and quantifying the co-sedimentation of kinesin with pellets of different microtubule types. Note that kinesin's tail does not prevent the motor from binding microtubules [66, 107]. Because differential binding was most pronounced for 10-100 nM kinesin [107, 112], we used a similar dilute kinesin concentration in our co-sedimentation assay (67 nM). To further enable direct comparison with previous measurements of kinesin's binding affinity [106], we included taxol in co-sedimentation assays using GDP microtubules but not GMPCPP microtubules.

We examined the co-sedimentation of kinesins with microtubules at three microtubule concentrations (0.28, 0.37, and 1.1 μM, Fig. 4.8). For each microtubule concentration, we carried out parallel co-sedimentation assays that differed in the presence of ATP or the non-hydrolyzable ATP analog AMPPNP (for example, Fig. 4.8 A), in order to differentiate between relative contributions to kinesin/microtubule binding through kinesin's tail (independent of ATP, [79]) versus its motor domain (dependent on ATP). We carried out gel-based protein quantitation using infrared fluorescence of Commassie-stained gels. The subunits of our purified kinesin and tubulin proteins separated well on protein gels. The infrared fluorescence response of Coomassie blue is quantitative for protein content between 10 ng and 20 μg per band [97], which encompasses the range in protein content examined here (80-320 ng kinesin or 1-4 μg tubulin per lane, Fig. 4.8 A).

For each microtubule concentration tested, we did not detect any significant difference in kinesin signals between microtubule types in assays using AMPPNP (green solid circles vs. magenta solid circles, Fig. 4.8 B; $P > 0.57$, Student's *t*-test) or ATP (green open circles vs. magenta open circles, Fig. 4.8 B; $P > 0.20$, Student's *t*-test). In contrast, within each microtubule type, we detected substantially higher co-sedimentation of kinesin with microtubules in the presence of AMPPNP than in the presence of ATP (Fig. 4.8). For example, we detected >1.8x higher kinesin signal in the pellet of GDP microtubules in assays using AMPPNP versus ATP (green solid circles vs. green open circles, Fig. 4.8 B). Note that the presence of ATP does not completely eliminate the equilibrium association of kinesin with the microtubule through its motor domain. Thus, the majority of kinesin signal in assays using AMPPNP corresponds to the ATP-dependent binding of kinesin's motor domain to the microtubule. This observation is perhaps not surprising, as the native kinesin protein used in the current study is a holoenzyme, containing both the kinesin heavy chain and kinesin light chains. Previous work [79] demonstrated that kinesin light chains inhibit the association of kinesin's tail with the microtubule. Taken together, our co-sedimentation data again demonstrate that native kinesin-1 does not bind preferentially to GTP-tubulin-rich microtubules.

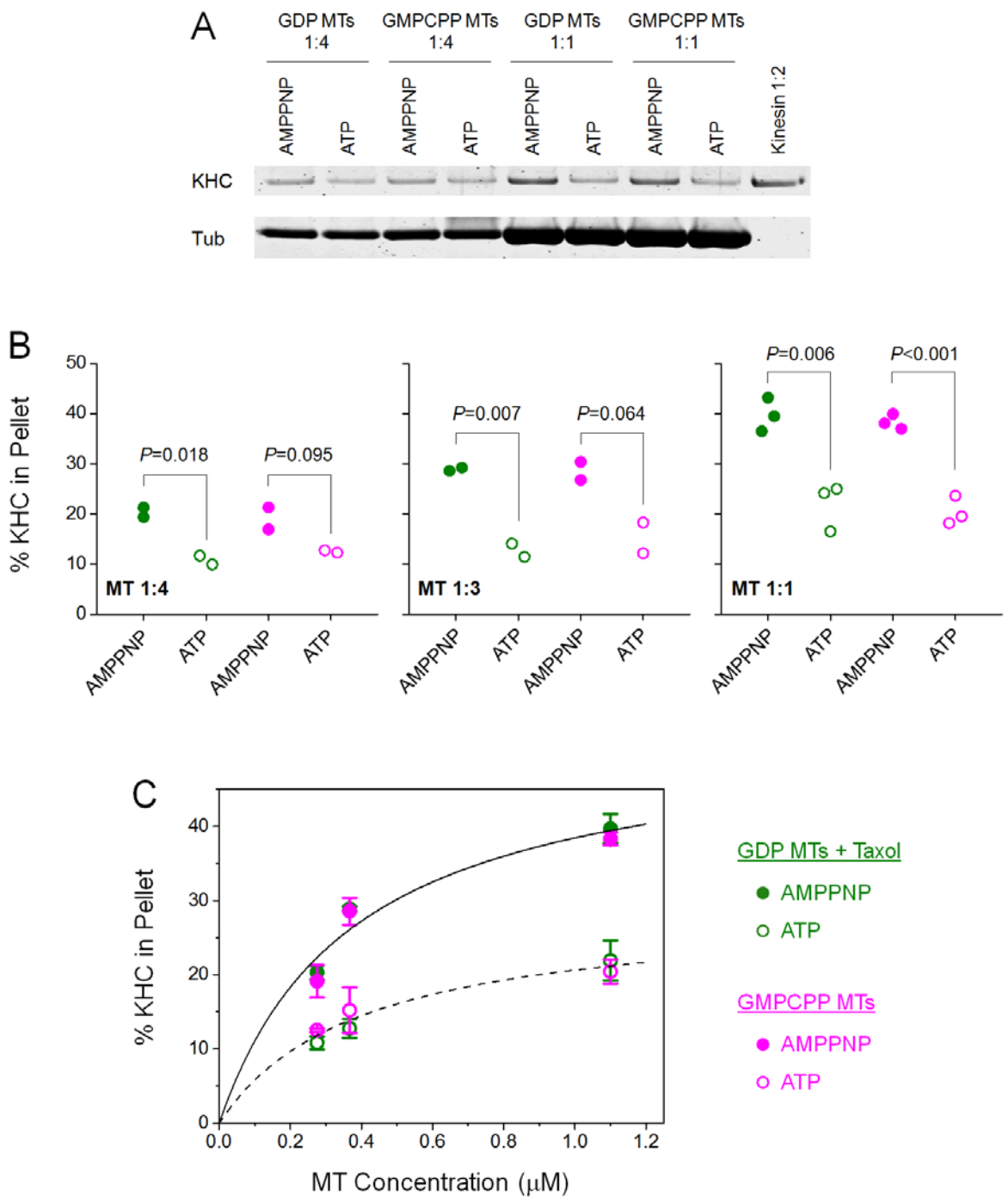

FIGURE 4.8. Native kinesin-1 does not preferentially co-sediment with GTP-tubulin-rich microtubules (MTs). Co-sedimentation was measured using bead-independent MT-affinity pulldown assays. Taxol (25 μM) was included in assays using GDP MTs. Assays using GMPCPP MTs were free of taxol. (*A*) Example co-sedimentation assays at two microtubule concentrations (1:1 and 1:4,

corresponding to 0.28 and 1.1 μM MT, respectively), and in the presence of 5 mM AMPPNP or 5 mM ATP as indicated. KHC, kinesin heavy chain; Tub, tubulin. Dilution of kinesin reference solution (1:2) corresponds to 50% of the input kinesin. (*B*) Dot plot of the fraction of KHC signal in the MT pellet, measured for three MT concentrations (1:4, 1:3, and 1:1; corresponding to 0.28, 0.37, and 1.1 μM MT, respectively). Green solid (or open) circle, assays using taxol-stabilized GDP MTs at 5 mM AMPPNP (or 5 mM ATP). Magenta solid (or open) circle, assays using taxol-free GMPCPP MTs at 5 mM AMPPNP (or 5 mM ATP). *P*-value is determined using Student's *t*-test. (*C*) Mean and standard error of KHC measurements in (B), as a function of MT concentration. Solid line, best fit of KHC signal in the presence of AMPPNP (averaged between MT types) to the Hill equation ($\theta = \frac{[L]^n}{K_d + [L]^n}$). Dashed line, best fit of KHC signal in the presence of ATP (averaged between MT types) to the Hill equation.

In summary, our biophysical and biochemical data indicate that the in vitro function of native kinesin-1 does not differ substantially between GMPCPP microtubules and GDP-microtubules (Figs. 4.3-4.7). We did not detect any difference in the co-sedimentation of native kinesin with the two microtubule types (Fig. 4.8), as reported previously for recombinant truncated kinesin [113, 114]. However, we do not rule out the possibility that the tubulin-nucleotide state of microtubules plays an important role in regulating kinesin-based transport in vivo. The native kinesin examined here contains important post-translational modifications (for example, phosphorylation [79, 115]) that are absent from recombinant proteins. The apparent discrepancy between the current study and previous investigations may reflect regulation of kinesin/microtubule interactions via post-translational modification of the motor. Future investigations will help shed light on the interplay between the motor's post-translational modifications and the microtubule's nucleotide-binding state for transport regulation in vivo.

Chapter 5. Effect of A Fluid Cargo Membrane on Kinesin-Based Transport [23]

5A. Introduction

In live cells, a cargo is often enclosed in a fluid lipid membrane and transported by a small team of ~two kinesins [23, 57, 64, 86], a scenario that is not captured in classical single-molecule investigations. To bridge this gap, several in vitro studies, including our own [41, 88], have begun to adapt single-molecule approaches to examine transport by a team of kinesins [27, 28, 43, 47, 66, 68, 69, 86]. While these investigations have revealed important emergent behaviors of small teams of kinesins, the cargos utilized in these and most in vitro studies still lack a physiologically relevant membrane. The use of model membranes to investigate motor-based transport [27, 43, 116-119] and the development of membrane-enclosed cargos that are directly compatible with optical trapping [119-122] have undergone important advances in recent years. Excitingly, a fluid lipid bilayer and a membrane-mimicking flexible linkage were recently demonstrated to impact cargo transport by two major molecular motors (the actin-based myosin Va [123] and the microtubule-based cytoplasmic dynein [121], respectively); the transport efficiency of kinesins was also demonstrated to differ for membrane-bound versus glass-anchored motors in a recent study using microtubule-gliding experiments [119]. Whether or how a fluid membrane impacts cargo transport by small teams of kinesins, however, has remained unclear.

A key experimental challenge in these investigations is that it is difficult to quantify the number of motors driving transport. Precise determination of motor number is fundamentally limited, as equilibrium binding of motors to cargos dictates that the total number of motors on a cargo is not well defined, even when the number of binding sites on the cargo is defined [69, 124]. Due to the three-dimensional nature of the cargo, the interface between the microtubule and the cargo surface is highly curved, in contrast to the flat geometry in microtubule-gliding experiments. As a result, when the cargo size exceeds the extension length of the motor (such as the ~0.5 μm diameter of the cargo optimized for optical trapping[8] vs. the ~0.08 μm length of the native kinesin motor [36, 37]), only a fraction of the motors present on the cargo surface are within reach of the microtubule to contribute to transport. For membrane-free cargos, this fraction depends non-trivially on Poisson statistics, cargo size, and motor length [5, 36, 37]. The presence of a fluid membrane further complicates the problem, as motors can in principle exploit diffusion to cluster near the microtubule, thereby increasing the fraction and thus the number of motors on the cargo that can contribute to transport.

For membrane-free cargos, “motile fraction” has served as a quantitative guide for motor number in classical single-molecule studies utilizing optical trapping [5]. Motile fraction, which indicates the probability that a cargo undergoes directed motion along the microtubule, is directly sensitive to the number of motors driving cargo transport [5]. The greater the motor number, the larger the motile fraction. In contrast to motor number, motile fraction is readily tuned and measured in experiments, particularly when an optical trap is used to confine individual cargos to the vicinity of the microtubule for interaction

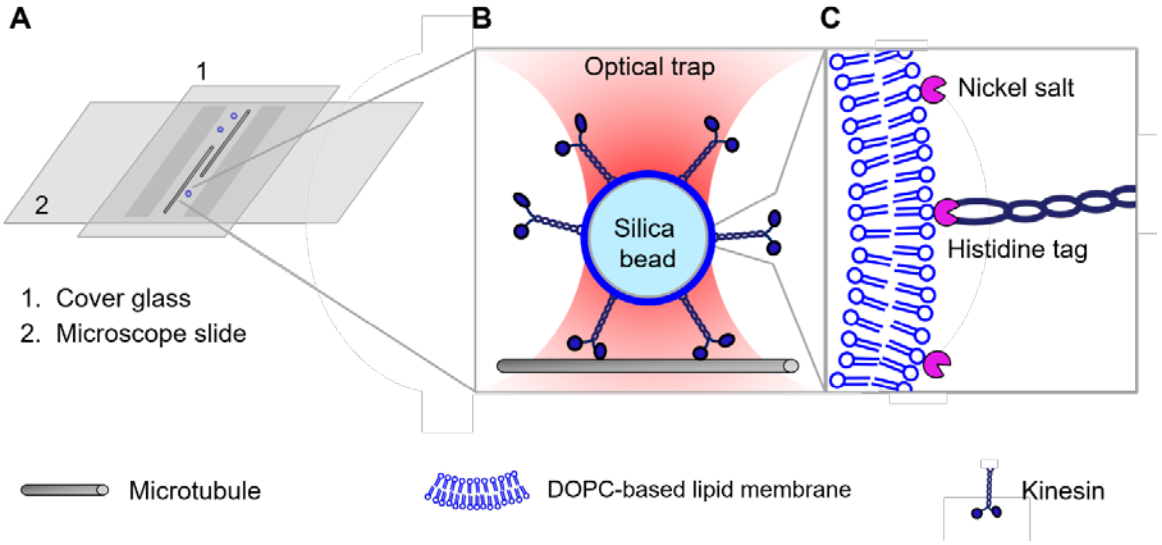

FIGURE 5.1. Experimental schematic. Illustration not to scale. (*A*) Optical trapping-based experiments were carried out in flow chambers, identically for membrane-enclosed cargos (panels b-c) and standard membrane-free cargos (not shown). The flow chamber was constructed by adhering a cover glass and a microscope slide together using two thin strips of double-sided Scotch tape. Microtubules were immobilized on the cover-glass surface; kinesin/cargo complexes were freely dispersed in solution in the flow chamber. (*B*) A single-beam optical trap was used to confine individual cargos to the vicinity of a microtubule to reduce the initial interaction distance between the microtubule and kinesins on the cargo. The trap was turned off upon observation of directed cargo motion along the microtubule, eliminating external load. For the membrane-enclosed cargos illustrated here, a silica bead supports a DOPC-based lipid bilayer, ensuring compatibility with the optical trap and matching the size of membrane-enclosed and membrane-free cargos for direct comparison. (*C*) Polyhistidine-tagged kinesins were specifically recruited to membrane-enclosed cargos via a nickel-functionalized lipid incorporated in the bilayer membrane.

[5, 6]. A motile fraction of ≲0.3 has served as a quantitative guide for reaching the single-molecule range in optical trapping-based investigations [5]. We recently extended the range of this quantitative guide and experimentally determined the one-to-one correspondence between motile fraction and motor number for a range of higher motile fractions [6]. Our recent work indicates that motile fractions of 0.3-0.8 encompass transport by a single kinesin through physiologically relevant transport by a small team of ~two kinesins [26].

In the current study, we applied motile fraction to tune the number of motors driving membrane-enclosed cargos at the start of transport. We used a single-beam optical trap to determine the motile fraction of membrane-enclosed cargos, as we did for standard membrane-free cargos. We also matched the size of our membrane-enclosed cargos to that of our membrane-free cargos, in order to preserve the one-to-one correspondence between motile fraction and motor number determined in our recent study [21]. Note that although membrane-bound motors can exploit diffusion to cluster near the microtubule, this clustering requires the cargo to break its rotational symmetry with respect to the microtubule. Because the optical trap acts as a frictionless bearing and the cargo rotates freely within the trap [26], clustering cannot take place before the cargo demonstrates directed motion along the microtubule, and thus clustering cannot not impact motile fraction. We experimentally accessed six motile fractions and contrasted the transport of membrane-enclosed versus membrane-free cargos at each motile fraction to isolate the impact of the fluid membrane from that of motor number. Our data demonstrate that a fluid cargo membrane significantly enhances the transport velocity of cargos carried by small teams of kinesin motors.

5B. Materials and methods

5B-i. Materials

Bovine brain tubulin was purified over a phosphocellulose column as previously described [45]. Recombinant kinesin protein (human K560, polyhistidine-tagged) was purified as previously described [26]. Lipids 1,2-dioleoyl-sn-glycero-3-phosphocholine (DOPC), 1,2-dioleoyl-sn-glycero-3-[(N-(5-amino-1-carboxypentyl)iminodiacetic acid)succinyl] (nickel salt) (DGS-NTA(Ni)), and 1,2-dioleoyl-sn-glycero-3-phosphoethanolamine-N-(lissamine rhodamine B sulfonyl) (ammonium salt) (rhodamine PE) were purchased from Avanti Polar Lipids, Inc. (Alabaster, AL, USA). Silicon beads (0.5 μm in diameter) were purchased from Bangs Laboratories, Inc. (Fishers, IN, USA). Carboxylated polystyrene beads (0.5 μm in diameter) were purchased from Polysciences, Inc. (Warrington, PA, USA). Chemicals were purchased from Sigma-Aldrich (St. Louis, MO, USA).

5B-ii. Microtubule preparation

Microtubules was prepared and diluted as described in Chapter 2B-ii.

5B-iii. Preparation of membrane-enclosed cargos

Membrane-coated cargos were prepared as previously described [45, 122, 125, 126] with modifications. A lipid mixture of 95% DOPC, 5% DGS-NTA(Ni), and 0.05% rhodamine PE was dried under vacuum at room temperature overnight. The dried lipid film was resuspended to a stock concentration of 4 mM in HNa100 buffer (pH 7.0, 20 mM HEPES, 100 mM NaCl, 1 mM EGTA, 1 mM dithiothreitol) via five freeze-thaw cycles, in which the lipid solution was flash frozen in a liquid nitrogen bath, followed by thawing in hand and vortexing briefly. The stock lipid solution was flash frozen in 100-µL aliquots and kept at -20 ºC until use. Silica beads (0.5 µm in diameter, Bangs Laboratories) were bath-sonicated in methanol, resuspended in 1 N KOH, bath-sonicated again, washed seven times in nanopure water, and bath-sonicated prior to use. Aliquots of lipid stock were diluted in an equal volume of HNa100 to 2 mM, and passed through a mini-lipid extruder (30-nm polycarbonate membrane, Avanti Polar Lipids) 21 times to create small unilamellar liposomes [121]. Immediately after extrusion, lipids were incubated with freshly washed silica beads for 30 min at room temperature in a dark box, with occasional gentle tapping to prevent bead sedimentation. The resulting membrane-enclosed cargos were washed four times in HNa100, resuspended in casein solution (5.55 mg/mL) in PMEE buffer (pH 7.2, 35 mM PIPES, 5 mM $MgSO_4$, 1 mM EGTA, 0.5 mM EDTA) for 30 min at room temperature in a dark box, and kept at 4 ºC for use within two days.

5B-iv. Preparation of motor/cargo complexes

Recombinant kinesin was incubated with membrane-enclosed cargos or carboxylated polystyrene beads (membrane-free cargos) as described in Chapter 3B-iv The concentration of membrane-enclosed cargos and the concentration of membrane-free cargos were kept constant at 3.38×10^5 particles/µL and 3.25×10^5 particles/µL, respectively. These cargo concentrations were empirically determined to optimize the number of isolated cargos in our field of view for optical trapping (data not shown). The concentration of kinesin was empirically varied to give rise to a range of motile fractions, as previously described [5, 119].

5B-v. Motile fraction and transport measurements

Motile fraction and cargo transport were measured in flow chambers using a single-beam optical trap, imaged via differential interference microscopy, and video-recorded at 30 Hz as previously described [123]; identical conditions were employed for membrane-enclosed cargos and membrane-free cargos. Briefly, we used a custom constructed single-beam optical trap [5, 8] to locally confine kinesin/cargo complexes to the neighborhood of the microtubule, and scored the fraction of cargos that demonstrated directed motility along the microtubule ("motile fraction"). To limit interference from external load, we used a very low trap power (<20 mW at fiber output) such that the optical trap was sufficient to position individual cargos but could not stall cargos carried by a single kinesin [26]. Upon observation of directed motion along the microtubule, we turned off the optical trap to enable cargo transport in the absence of external load.

5B-vi. Data analysis

Cargo trajectories were particle-tracked to 10 nm resolution (1/3 pixel) using a template-matching algorithm as previously described [127].

The run length of a motile cargo was determined as the net displacement of the cargo along the microtubule between binding and dissociation as described in Chapter 2B-v.

The association time of individual kinesin/cargo complexes with the microtubule was determined as the time between landing and dissociation. To account for human reaction time during manual shut-off of the optical trap, only trajectories >0.3 s were analyzed. The cumulative probability distribution of the association time was fitted to the cumulative probability function of a single exponential distribution, $1-Ae^{-x/t}$. Mean association time and standard error for each distribution were determined from the best-fit decay constant t and uncertainty, respectively.

Pausing during continuous cargo motion was identified without operator bias using Bayesian statistics-based automatic software [8] that parses each cargo trajectory into a series of segments of constant velocity. To evaluate cargo velocity under no load, only portions of each trajectory >300 nm were analyzed. A pausing event was identified when the velocity fell below 100 nm/s for at least 0.5 s. The frequency of pausing was determined as the number of pauses per second. The cumulative probability distribution of pause duration was fitted to the cumulative probability function of a single exponential distribution, $1-Ae^{-x/p}$. Unless specified as the arithmetic mean, mean pause duration and standard error were determined from the best-fit decay constant p and uncertainty, respectively.

The velocity of each trajectory was determined as the average velocity of its non-pausing segments, weighted by the corresponding segmental durations. Mean velocity and standard error for each experimental condition (motile fraction and cargo type) were

determined as the arithmetic mean and the associated standard error of the individual cargo velocities, respectively.

5B-vii. Statistical analysis

One-way analysis of variance (ANOVA) was used to determine significant differences between multiple distributions of pause frequency or velocity measurements. The rank-sum test was used to detect significant differences between two distributions of measurements of pause duration or run length. Welch's *t*-test was used to determine the significance of differences between two distributions of velocity measurements.

5C. Results and discussion

We used an optical trap to determine the impact of a fluid cargo membrane on kinesin-based transport in vitro (Fig. 5.1). We employed traditional polystyrene beads as our membrane-free cargos [21, 28, 128]. For membrane-enclosed cargos, we employed a DOPC-based lipid bilayer to model the fluid cellular membrane [21, 26, 28, 121], and used a silica core to control cargo size and to ensure compatibility with optical trapping [5, 119] (Fig. 5.1). Note that the silica core does not influence the fluidity of our model membrane [120] but minimizes deformation of the supported membrane during kinesin-based transport [5]. Importantly, the presence of a lipid membrane does not significantly impact the refractive index or the physical size of the membrane-coated cargo [122, 129], and thus does not impact optical trapping or the one-to-one correspondence between motile fraction and motor number determined in our recent study [130]. For each cargo type, we empirically tuned the input ratio of kinesins to cargos to achieve six motile fractions and measured 120-200 trajectories per motile fraction. Using these measurements, we characterized three key transport characteristics (run length, pause, and velocity) for membrane-enclosed cargos and membrane-free cargos under otherwise identical conditions. We used cumulative probability distributions, as opposed to histograms, to better illustrate potential difference or agreement between two sets of measurements (for example, Fig. 5.2 A). As detailed below, these key transport characteristics critically impact the distance and speed of cargo delivery in vivo, and are likely sensitive to changes in inter-motor interactions associated with a fluid cargo membrane.

5C-i. Cargo run length is similar between membrane-enclosed and membrane-free cargos across six motile fractions

We first examined the impact of a fluid membrane on cargo run length (Fig. 5.2). Extended run length is important for achieving transport across large spatial distances in cells. Previous studies of membrane-free cargos revealed that run length increases as motor number increases [27, 28, 41, 43, 66, 68, 69]. Here we used the motile fraction to match the number of motors driving each cargo type at the start of transport. For membrane-free cargos, this motor number remains unchanged during transport as the motors are uniformly and statically anchored on the cargo surface [5]. For membrane-enclosed cargos, however, the number of motors driving the cargo can in principle increase during transport as the motors exploit diffusion to cluster near the microtubule. We thus anticipated that, at the same motile fraction, the run length of membrane-enclosed cargos would be significantly longer than that of membrane-free cargos.

For membrane-free cargos and consistent with previous studies, we found that run length increased gradually but significantly with increasing motile fraction (Fig. 5.2). In the single-molecule range (motile fraction ~0.3), the mean run length was 1.60 μm (black line, Fig. 5.2 A(i)), in excellent agreement with previous reports of single-kinesin run length for a similar recombinant construct [5, 43, 69]. At a motile fraction of 0.8, cargo run length was significantly longer than that at a motile fraction of 0.3 (p=0.028, rank-sum test) and agreed well with that expected for a small team of kinesins linked to membrane-free cargos [27, 28, 41, 43, 66, 68, 69].

Contrary to our expectation, at none of the six motile fractions was run length significantly longer for membrane-enclosed cargos versus membrane-free cargos (Fig. 5.2; $p \geq 0.21$, rank-sum test). Note that at the highest motile fraction examined (0.8), although the average run length for membrane-enclosed cargos was somewhat higher than that for membrane-free cargos (2.48 μm vs. 2.04 μm, Fig. 5.2 A(iii)), this difference was not statistically significant (p=0.28, rank-sum test). Our data suggest that in the physiologically relevant few-kinesin range, a fluid membrane does not substantially impact the number of kinesins driving transport. We do not rule out the possibility of a subtle increase in motor number for membrane-enclosed cargos, but the effect is not sufficient to significantly increase run length.

Our finding is surprising, as diffusion within the fluid membrane ought to significantly enhance the number of kinesins driving membrane-enclosed cargos. The timescale required for a kinesin to explore the cargo surface to come within reach of the microtubule (~0.56 s using a diffusion constant of 1.4 $\mu m^2/s$, reference [27]) is substantially shorter than the mean association time between the membrane-enclosed cargo and the microtubule (2.67-4.78 s depending on motile fraction, data not shown); the single kinesin also has a significant, >5-fold faster associated rate than dissociation rate for the microtubule [26, 43, 120]. However, the area on the cargo directly accessible to the microtubule may not remain constant during transport. A cargo can “tumble” as individual motors stochastically bind to and unbind from the microtubule [66, 116, 117]. With each tumble, a different portion of the cargo surface would be exposed to the microtubule, and the clustering process would start afresh. We thus speculate that, although the fluid membrane can promote motor clustering, its effect on run length is

limited by stochastic tumbling of the cargo during transport. In principle, stochastic tumbling may be less frequent for larger sized cargos. However, because the timescale of motor diffusion scales quadratically with cargo size, the effect of motor clustering will also be more limited. Owing to the spherical symmetry of cargos used in most in vitro studies, direct observation of tumbling remains difficult. Future developments, such as anisotropic labeling of spherical particles, will empower investigations into the extent of cargo tumbling and its impact on the clustering of membrane-bound motors during transport.

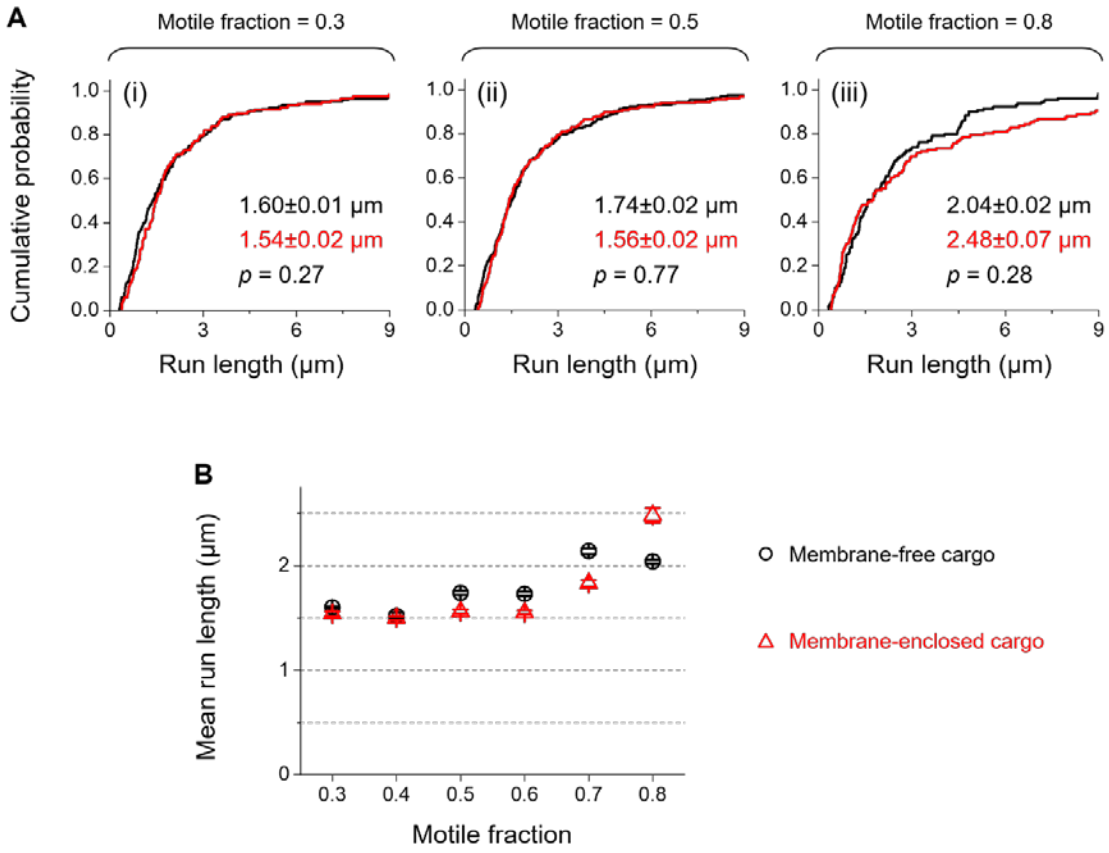

FIGURE 5.2. Run length does not differ between membrane-enclosed cargos (red) and membrane-free cargos (black). (*A*) Cumulative probability distributions of cargo run length at three motile fractions. Mean run length (± standard error) and *p*-value (rank-sum test) are indicated (n=117-197). The two distributions measured at each motile fraction do not differ significantly from each other ($p \geq 0.27$, rank-sum test). (*B*) Mean run length (± standard error) at six motile fractions (n=117-197). The two mean run lengths determined at each motile fraction do not differ significantly from each other ($p \geq 0.21$, rank-sum test).

5C-ii. Membrane-enclosed cargos pause similarly to membrane-free cargos across six motile fractions

We next examined the impact of a fluid membrane on cargo pausing (interruptions during continuous motion). In vivo, pauses delay the delivery of cargos to target destinations, but can also contribute to cargo sorting at the pause site [131]. The mechanism underlying single-motor pausing has remained unclear. When functioning in a small team, the paused motor lags behind and pulls against moving motors via their common cargo. This force-based interaction is delayed for membrane-enclosed cargos, because the attachment point of the motor to the cargo can "slide" within the membrane to alleviate force in the direction parallel to the cargo surface [66, 120]. A delayed interaction between motors can potentially increase the likelihood that the paused motor stochastically resumes motion before the cargo stops, thereby reducing the sensitivity of cargo transport to pausing of individual motors.

We did not detect a substantial difference in pausing frequency between cargo types (Fig. 5.3 A). For both membrane-enclosed and membrane-free cargos, the number of pauses per unit time remained relatively low and did not change appreciably with increasing motile fraction ($p \geq 0.41$, ANOVA). Averaging across six motile fractions, we determined a mean pausing frequency of 0.040 ± 0.006 s^{-1} for membrane-enclosed cargos, in good agreement with a mean pausing frequency of 0.035 ± 0.005 s^{-1} for membrane-free cargos (Fig. 5.3 A).

We also did not detect a significant difference in pausing duration between cargo types (Fig. 5.3 B-C). Due to the low pausing frequency (Fig. 5.3 A), the number of pauses that we measured was limited for each cargo type at each motile fraction (n=11-48 pauses). Despite this limitation, our data indicate that the associated arithmetic mean duration of pauses agreed well between cargo types at each motile fraction, and remained approximately constant across motile fractions for each cargo type (Fig. 5.3 B). To increase the statistical power of our analysis, we combined measurements from all motile fractions for each cargo type (Fig. 5.3 C). These combined data again revealed similar pausing durations between cargo types (p=0.23, rank-sum test), giving rise to a mean duration of 1.53 ± 0.01 s for membrane-enclosed cargos and 1.69 ± 0.01 s for membrane-free cargos (Fig. 5.3 C). These mean durations are in good agreement with the single-motor pausing duration previously reported for a similar kinesin construct [132].

Our data suggest that individual kinesins pause asynchronously when functioning in small teams. The low frequency of single-kinesin pausing (~0.040 s^{-1} at motile fraction ~0.3, Fig. 5.3 A) corresponds to an extended interval of ~25 s between successive pauses, which is >5-fold longer than the average association time of our cargos with the microtubule (2.7-4.8 s depending on motile fraction, data not shown). When motors are not synchronized with each other, the probability that two or more motors pause at the same time is low. In this scenario, the frequency of cargo pausing is largely approximated by the frequency of single-motor pausing, which is in good agreement with our observations (Fig. 5.3 A).

Further, our data indicate that the fluid membrane does not alter the sensitivity of a cargo to single-kinesin pausing. While sliding of motors within the membrane may delay the force-based interference between the paused motor and the moving motors, the timescale of this delay is substantially shorter than the typical duration of single-kinesin pausing (~1.6 s, Fig. 5.3 C). It is possible that the fluid membrane is effective in limiting the sensitivity of the cargo to significantly shorter single-motor pauses. Future identification of factors that significantly reduce single-kinesin pausing duration will help shed light on this intriguing possibility.

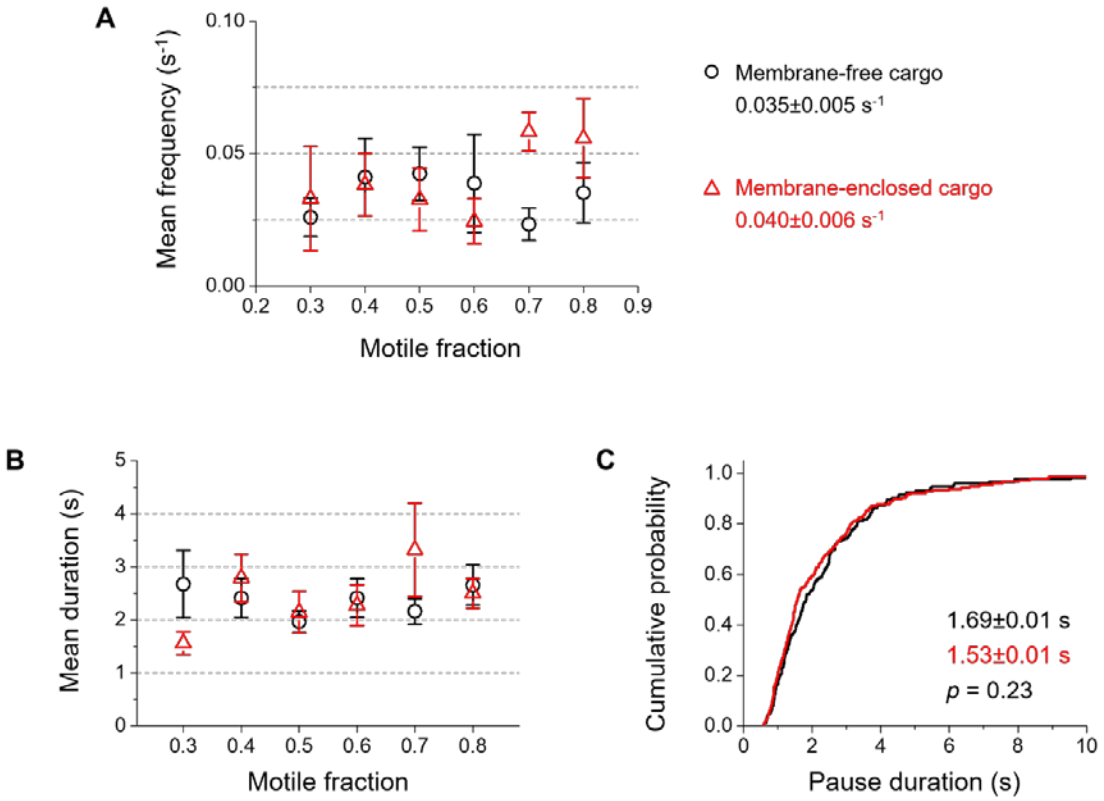

FIGURE 5.3. Pausing does not differ between membrane-enclosed (red) and membrane-free (black) cargos. Arithmetic mean (*A*) frequency (n=4-5 experiments) and (*B*) duration (n=11-48 pauses) of pauses at six motile fractions. (*C*) Cumulative probability distribution of pause duration, pooled from measurements at all six motile fractions ($n \geq 175$ pauses). Mean pause duration (±standard error) is indicated. These two distributions do not differ significantly from each other (p=0.23, rank-sum test).

5C-iii. Membrane-enclosed cargos move faster than membrane-free cargos at higher motile fractions

We next examined the impact of a fluid membrane on cargo velocity. The velocity of a single motor is not typically uniform within a population of kinesins [120, 133]. During transport by a small team of kinesins, the faster motors lead the cargo and the slower motors lag behind; force-based interactions between motors tend to prompt the lagging kinesin to dissociate prematurely from the microtubule [134], causing the cargo to tumble forward to the position of the leading motor. Sliding of motors within the lipid membrane delays force-based interactions between motors and enables the leading kinesin to move forward further before the lagging motor dissociates. We thus predicted that, when transported by small teams of kinesins, membrane-enclosed cargos would move faster than membrane-free cargos under otherwise identical conditions.

For membrane-free cargos, we detected a significant change in the distribution of cargo velocity with increasing motile fraction (p=3×10^{-8}, ANOVA) (left, Fig. 5.4 A). In the single-motor range (motile fraction ~0.3), the distribution of cargo velocity demonstrated a subpopulation of slow runs, with 26% of cargos demonstrating at a speed lower than 0.6 μm/s (top, Fig. 5.4 B). Heterogeneity in single-kinesin velocity has been previously observed for the same motor construct [133, 135]. Here, we found that the fraction of the slow runs increased substantially with increasing density of motors on the cargo. For example, at a motile fraction of 0.8, 56% of cargos moved slower than 0.6 μm/s (top, Fig. 5.4 B). The median velocity of these slow runs (<0.6 μm/s) remained largely constant at different motile fractions (top, Fig. 5.4 C), as did the median velocity of cargos faster than 0.6 μm/s (top, Fig. 5.4 D). Together, our data demonstrate a significant, 19% reduction in median velocity at a motile fraction of 0.8 versus a motile fraction of 0.3 (p=9x10^{-8}, Welch's t-test). This observation is consistent with previous reports of reduced cargo velocities at higher motor densities [28, 66],

In contrast, the velocity distribution of membrane-enclosed cargos did not change significantly with motile fraction (p=0.80, ANOVA). Irrespective of motor density, majority of the cargos (≥70%) moved faster than 0.6 μm/s (right, Fig. 5.4 A) and the median velocity of these fast runs remained approximately constant (bottom, Fig. 5.4 D). Interestingly, the median velocity of slow runs was somewhat higher for higher motile fraction, increasing from 0.34±0.03 μm/s at a motile fraction of 0.3 to 0.51±0.03 μm/s at a motile fraction of 0.8 (bottom, Fig. 5.4 C). However, as the fraction of slow runs was limited (<30%), velocity change in slow runs did not significantly impact cargo velocity (including both slow and fast runs), which remained approximately constant across motile fractions, with <5% variation (right, Fig. 5.4 A)

At a motile fraction of 0.3 (~single motor range), the velocity distribution of membrane-enclosed cargo did not differ significantly from that of the membrane-free case (p=3.7x10^{-9}, Welch's t-test, Fig. 5.5 A(i)). Both cargo types moved at a similar median velocity of ~0.7 μm/s (Fig. 5.5 A(i)), in good agreement with the previously

reported single-motor velocity of similar kinesin constructs [66, 69, 133]. This observation is expected, because a fluid membrane should not impact the intrinsic function of the motor at the single-molecule level.

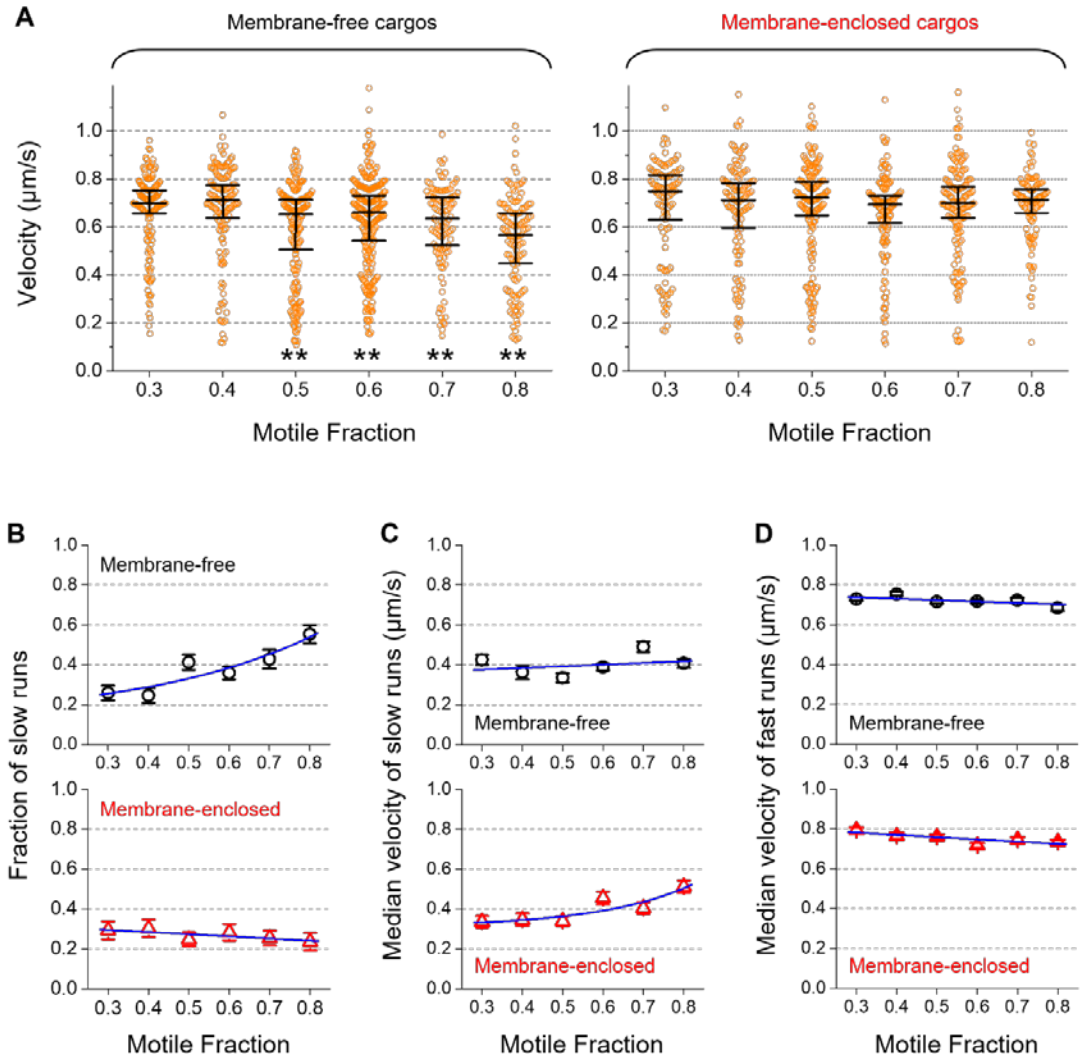

FIGURE 5.4. The change in velocity distribution with motile fractions differ between cargo types. (*A*) Dot plot of velocity measurements for each experimental conditions (n=97-208). Horizontal bars, median values and 30/70 percentiles. **, significant difference from measurements at a motile fraction of 0.3 (p<0.005, Welch's t-test). (*B-C*) Fraction and median velocity of cargos moving slower than 0.6 μm/s. (d) Median velocity of cargos moving faster than 0.6 μm/s. Error bars in (*B-D*), standard error. Blue lines, guides to the eye.

At higher motile fractions, the velocity distribution of membrane-enclosed cargos differed significantly from that of the membrane-free cargos (for example, $p \leq 0.004$, Welch's *t*-test, Fig. 5.5 A(ii-iii)); the velocity of membrane-enclosed cargos was substantially faster than the membrane-free case (as indicated by positive values in Fig. 5.5 B). We did not detect any indication of membrane-free cargos moving faster than membrane-enclosed cargos at any motile fraction, as the velocity difference between the two cargo types did not fell significantly below zero (Fig. 5.5 B). At a motile fraction of 0.8, the mean velocity of membrane-enclosed cargos demonstrated a significant, 0.15

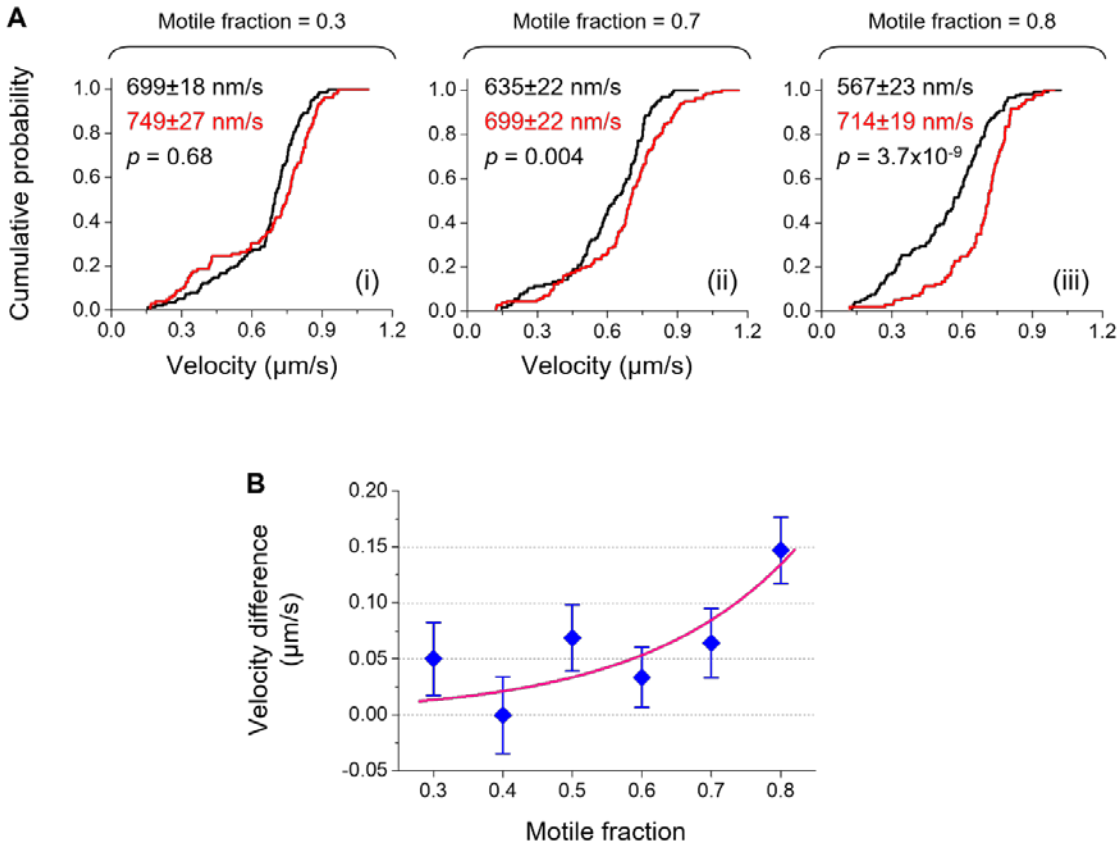

FIGURE 5.5. Membrane-enclosed cargos (red) move faster than membrane-free cargos (black) at higher motile fractions. (*A*) Cumulative probability distributions of velocity at three motile fractions. Median velocity (± standard error) and *p*-value (Welch's *t*-test) are indicated (n=97-139). (*B*) The difference in the median velocity of two cargo types at each motile fraction. A positive value indicates that membrane-enclosed cargos move faster than membrane-free cargos. Pink line, guide to the eye.

±0.03 μm/s increase over the membrane-free velocity (p=3.7x10^{-9}, Welch's t-test, Fig. 5.5 A(iii) and Fig. 5.5 B).

Our data are consistent with the model that a fluid membrane delays force-based interactions between kinesins: a membrane-enclosed cargo tumbles forward a larger distance than does a membrane-free cargo upon dissociation of the lagging motor. Under otherwise identical conditions, coupling motors via a fluid membrane reduces the sensitivity of the cargo to the subpopulation of slow motors, via lowering the fraction of slow runs (Fig. 5.4 B) and improving the median velocity of these slow runs (Fig. 5.4 C). In this model, the effect of the membrane on velocity is smaller for cargos with less-fluid membranes. We are working to develop new cargos with altered membrane fluidity to test this possibility. Additionally, because the mobility of the motor's attachment point on the cargo surface is limited by the length of the motor, it will be interesting to explore how the effect of membrane can be modulated by the length of the motor's tail domain. We note that the exact mechanism underlying the slowing velocity of membrane-free cargos is not fully understood. In addition to force-based interactions between motors discussed here, non-mechanical interactions (for example the physical spacing of motors on the microtubule) can also influence velocity for membrane-free cargos [43, 69]. It is possible that a delay in force-based interactions may also impact non-mechanical interactions as well as force-based interactions between motors, further contributing to the observed velocity increase of membrane-enclosed cargos versus membrane-free cargos. Such an enhanced velocity is likely important for the timely delivery of cargos in cells.

Our finding is perhaps surprising, as a recent study using microtubule-gliding experiments revealed a slower transport velocity for kinesins anchored atop a fluid lipid membrane versus a traditional glass surface [69]. However, a key difference between studies is that the interface between the cargo and the microtubule is highly curved in optical-trapping experiments (Fig. 5.1) but flat in microtubule-gliding experiments [136]. Sliding of the motor's attachment point within the cargo membrane alleviates the component of force parallel to the cargo surface, but not the component of force perpendicular to the cargo membrane. In vivo, the curvature of the cargo/microtubule interface can differ between cargo types. Our study raises the exciting possibility that the impact of a fluid membrane combines nontrivially with cargo geometry to control kinesin-based transport.

5D. Future direction

A future direction will be to characterize the effect of a fluid membrane on kinesin-based transport at lower ATP levels. Kinesins are nanomachines that will use the energy from ATP hydrolysis to step directionally along the microtubule [4]. The lower ATP level reduces the motor's dissociation rate without impacting its association rate with the microtubule, making it less likely for the cargo to stochastically

flopping/tumbling during transport. Because we speculated that the lack of effect of a membrane on the run length reflects stochastic tumbling of cargos during transport, a reduction in this stochastic tumbling ought to improve the probability of motors clustering near the cargo/microtubule interface and to enhance the run length of membrane-enclosed cargos over that of membrane-free cargos.

I have carried out the initial measurements for this new direction. I reduced the ATP level in my experiments from the saturating level to 0.01 mM, leading to a >5-fold reduction in the motor's dissociation rate [7] (Aim 1b in my advancement proposal). Preliminarily, I observed an increased run length and pausing frequency for membrane-enclosed cargos at the lower ATP. In particular, an increase in pausing frequency is encouraging, as it may reflect a higher density of motors traffic jamming at the cargo/microtubule interface. Future investigations will include control experiments using membrane-free cargos, where motor clustering is not a possibility.

Chapter 6. Effect of membrane cholesterol on kinesin-based transport [25]

6A. Introduction

Cholesterol is a small lipid molecule and a structural component of cell membranes in cells. There are increasing evidence indicating an association between membrane cholesterol and aging/neurodegeneration [137-140] where defects in molecular-motor-based transport have emerged as a common early theme. Recent studies investigating the cellular cargo phagosome (Fig. 6.1) have uncovered an intriguing correlation between the motility of this cellular cargo and its membrane cholesterol. Specifically, the motility of phagosomes is initially bidirectional (moving both in the direction of and the opposite of kinesin-based transport) but switches to minus-ended motion (moving in the opposite direction of kinesin) after some time [86, 141, 142]. Associated with this apparent reduction in kinesin-based transport is a significant, two-fold increase in membrane cholesterol [86]. Based on these in vivo data, we hypothesized that membrane cholesterol impairs kinesin-based transport.

To test our hypothesis, we used a fluid, DOPC-based lipid membrane to model the cellular membrane in vitro. We supported this membrane atop a silica core to ensure compatibility with optical trapping and we recruited kinesin onto our membrane-enclosed cargos as we did in our recent study [23]. We systematically varied the molar fraction of cholesterol in our membrane composition to range between 5-50% [117-120, 143]. Over this range of membrane cholesterol, the resulting membranes demonstrate microscopic uniformity at room temperature (our experimental condition) [144] with its lipid/motor diffusion reduced in a cholesterol-dosage-dependent manner [120, 144, 145].

To mimic the crowded “road” conditions along microtubules in cells, we used tau

FIGURE 6.1. Illustration of phagosome formation. Phagosome is a cellular cargo that is formed, when the cell engulfs a foreign particle into a membranous compartment. Molecular motors such as kinesins are membrane-bound to drive phagosomal motion in cells

as our model microtubule-associated protein. Tau is a small protein that is enriched in neurons [142, 146]. In vitro decoration of microtubules with tau has been shown to prompt kinesin to dissociate prematurely from the microtubule [47, 146], which in turn impairs multiple-kinesin travel [42, 47] and velocity [42]. However, how kinesin-based transport is maintained in the presence of high tau levels, particularly in healthy neurons, remains an important open question. Here we employed a decoration ration of 1 tau per 5.5 tubulin dimer, which is approximately twice the physiological level of tau decoration in cells The resulting level of tau decoration of the microtubule is within the physiological level of tau decoration in cells [110, 146], which has been demonstrated to strongly inhibit kinesin-based transport in vitro, including the probability of cargo binding to tau-decorated microtubules [47, 110, 147].

We examined the effect of membrane cholesterol on the transport of both membrane-enclosed cargos and traditional membrane-free cargos along tau-free microtubules and tau-decorated microtubules. We focused our study on the probability of kinesin-based cargo binding to microtubules, quantified using a single-beam optical trap to position individual cargo near the microtubule and to score the percentage of cargos that demonstrated binding and directed motion along the microtubule. The probability of cargo binding to microtubules is important because the cargo must bind to the microtubule prior to carrying out any transport process. We had previously demonstrated that the binding probability range of 30-80% encompass transport by a single kinesin through physiologically relevant transport by a small team of ~two kinesins [26]. Our data demonstrate that, in the absence of tau, membrane cholesterol did not significantly alter the probability of cargo binding to microtubules. In contrast, in the presence of tau, coupling via a fluid membrane significantly promoted cargo binding to the microtubule; this effect was countered by membrane cholesterol.

6B. Materials and methods

6B-i. Materials

Bovine brain tubulin was purified over a phosphocellulose column as previously described [45]. Recombinant human kinesin-1 (full-length KIF5A heavy chain, polyhistidine-tagged) was purified as previously described [148]. Recombinant human tau 23 (htau23), bovine brain tubulin, and bovine brain conventional kinesin were purified as previously described [47]. Htau23 was flash frozen in 1x PM buffer (100 mM PIPES, 1 mM $MgSO_4$, 2 mM EGTA, pH 6.9). Lipids were purchased from Avanti Polar Lipids, Inc. (Alabaster, AL, USA). Silicon beads (0.5 μm in diameter) were purchased from Bangs Laboratories, Inc. (Fishers, IN, USA). Carboxylated polystyrene beads (0.5 μm in diameter) were purchased from Polysciences, Inc. (Warrington, PA, USA). Cholesterol and chemicals were purchased from Sigma-Aldrich (St. Louis, MO, USA).

6B-ii. Microtubule preparation

Taxol-stabilized microtubules were polymerized by incubating 12 μM tubulin in 1x PM buffer (supplemented with 22 μM taxol and 1.1 mM GTP) for 20 min at 37 °C, diluted to 960 nM in PMEE buffer (supplemented with 20 μM taxol and 1 mM GTP), then incubated for 20 min at 37 °C with an equal volume of PMEE buffer (pH 7.1, supplemented with 20 μM taxol and 1 mM GTP) containing 0 nM or 368 nM htau23. The prepared microtubules (bare or decorated with htau23) were anchored to coverslip surfaces preincubated with poly-L-lysine as previously described [4, 47]. This concentration of microtubules was empirically determined to maintain sufficient numbers of isolated and parallel microtubules (~3-5 microtubules) extending across our field of view (20 μm × 20 μm, imaged at 100× magnification) (data not shown). The concentration of tau used here corresponds to a 1:5.5 ratio of bound tau to tubulin dimer, calculated using a previously developed model and binding parameters for htau23 [146].

6B-iii. Preparation of membrane-enclosed cargos and motor/cargo complexes

Membrane-coated cargos were prepared as described in Chapter 5B-iii. Lipid composition was DOPC-based and was tuned to contain 0%, 25%, and 50% cholesterol.

Motor/cargo complexes were prepared as described in Chapter 5B-iv.

6B-iv. Motile fraction and transport measurements

Motile fraction and cargo transport were measured in flow chambers as described in Chapter 5B-v. Identical motor/cargo preparations were used in parallel experiments for both bare microtubules and tau-decorated microtubules.

6B-v. Data analysis and statistical analysis

Cargo trajectories were and analyzed as described in Chapter 5B-vi.

6C. Results and discussion

6C-i. Membrane cholesterol does not influence the probability of cargo binding to tau-free microtubules

We first examined the effect of membrane cholesterol on cargo transport in the absence of tau (0 tau, Fig. 6.2 *A*). We matched the size of our membrane-enclosed cargos to that of our membrane-free cargos, in order to preserve the one-to-one correspondence between motile fraction and motor number determined in our recent study [21]. We tuned the density of motors during motor/cargo incubation to achieve similar binding probability for both membrane-free cargos (rigid, 0 tau, Fig. 6.2 *A*) and cholesterol-free membrane-enclosed cargos (0% cholesterol, 0 tau, Fig. 6.2 *A*). We then increased the cholesterol content, to 25% and 50%. We did not detect a significant change in the probability of cargo binding to microtubules (0 tau, Fig. 6.2 *A*). We repeated this observation for a range of five motor densities on the cargo (open circles, Fig. 6.2 *B*). Taken together, our data demonstrate that, in the absence of tau, cholesterol does not significantly influence the binding probability of kinesin-based cargos to microtubules.

6C-ii. Membrane cholesterol does not influence the probability of cargo binding to tau-free microtubules

We next examined the effect of membrane cholesterol on cargo transport in the absence of tau (1 tau : 5.5 tubulin, Fig. 6.2 *A*). We verified that the presence of tau significantly limits the probability of membrane-free cargos binding to microtubules (rigid, Fig. 6.2 *A*). This observation is in excellent agreement with previous reports that tau impairs the interaction between kinesins and microtubules [47, 110, 147]. In contrast, we detected a significantly smaller effect of tau when the motors are coupled together via a fluid membrane (0% cholesterol, Fig. 6.2 *A*) ($p < 0.01$, Kolmogorov–Smirnov test). Excitingly, this “rescue” effect is diminished with increasing membrane cholesterol. At 50% cholesterol, the membrane-enclosed cargo demonstrated similar probability of binding to the microtubule the membrane-free cargos. These observations again repeated for a range of five motor densities on the cargo (Fig. 6.2 *B*).

Taken together, our data demonstrate that a fluid membrane promotes cargo binding in the presence of tau, this effect is diminished by membrane cholesterol. We are in the process of analyzing cargo run length and velocity associated with each experimental condition. Preliminarily, the main effect of membrane cholesterol is to limit cargo/microtubule binding interaction.

Our data suggest that the kinesin’s ability to search and to avoid local roadblocks on the microtubule is strongly determined by the mobility of the motor’s attachment point the microtubule surface is limited. For the membrane-enclosed case, the attachment point of the motor on the cargo is mobile, which helps to increase the search area of the motor.

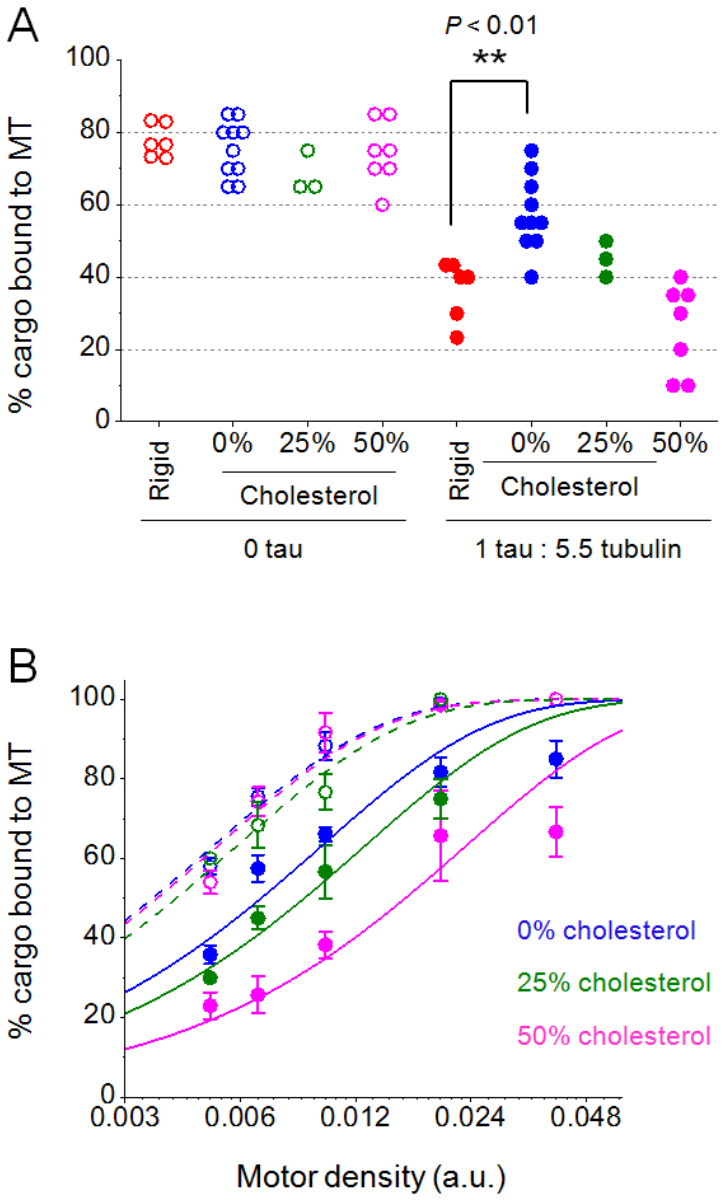

FIGURE 6.2. The probability of kinesin-based cargos binding to and moving along tau-free microtubules and tau-decorated microtubules. (*A*) Measurements of cargo binding probability at an example motor density. Rigid, membrane-free cargos. 0-50% cholesterol, membrane-enclosed cargos. Asterisks, significantly higher binding probability for membrane-enclosed cargos (0% cholesterol) than for membrane-free cargos (rigid). (*B*) Measurements of cargo binding probability for five motor densities. Error bar, standard error of the mean. Open circles, tau-free microtubules. Solid circles, tau-decorated microtubules.

to the cargo surface. For the membrane-free case, the attachment point of the motor to the cargo is immobile and the ability of individual motors to search and explore An increase in search area is likely beneficial for the motor to avoid local roadblocks such as tau. Cholesterol limits the mobility of the attachment point, which would be consistent with the collapse back to the membrane-free case observed in our study.

6D. Future direction

Our study here highlights an exciting, novel role of the cargo membrane in the regulation of kinesin-based transport. A future direction will be to characterize how cholesterol influences the effect of tau on membrane-coupled kinesins at lower ATP levels. Previous work from the Xu lab demonstrated that reduced ATP levels increase team kinesin run length despite the presence of tau on microtubules [42]. Our previous study was carried out using rigid cargos without a membrane. It will be very interesting to understand whether or how the rescue effect at low ATP might persist/amplify for membrane-enclosed cargos, and how such effect maybe further tuned by membrane cholesterol level.

References

1. Vale, R.D., *The molecular motor toolbox for intracellular transport.* Cell, 2003. **112**(4): p. 467-80.

2. Saxton, W.M. and P.J. Hollenbeck, *The axonal transport of mitochondria.* J Cell Sci, 2012. **125**(Pt 9): p. 2095-104.

3. Mandelkow, E. and E.M. Mandelkow, *Kinesin motors and disease.* Trends Cell Biol, 2002. **12**(12): p. 585-91.

4. Schnitzer, M.J. and S.M. Block, *Kinesin hydrolyses one ATP per 8-nm step.* Nature, 1997. **388**(6640): p. 386-90.

5. Block, S.M., L.S. Goldstein, and B.J. Schnapp, *Bead movement by single kinesin molecules studied with optical tweezers.* Nature, 1990. **348**(6299): p. 348-52.

6. Svoboda, K. and S.M. Block, *Force and velocity measured for single kinesin molecules.* Cell, 1994. **77**(5): p. 773-84.

7. Schnitzer, M.J., K. Visscher, and S.M. Block, *Force production by single kinesin motors.* Nat Cell Biol, 2000. **2**(10): p. 718-23.

8. Neuman, K.C. and S.M. Block, *Optical trapping.* Rev Sci Instrum, 2004. **75**(9): p. 2787-809.

9. Ashkin, A., et al., *Observation of a single-beam gradient force optical trap for dielectric particles.* Opt Lett, 1986. **11**(5): p. 288.

10. Ashkin, A., J.M. Dziedzic, and T. Yamane, *Optical Trapping and Manipulation of Single Cells Using Infrared-Laser Beams.* Nature, 1987. **330**(6150): p. 769-771.

11. Ashkin, A., *Acceleration and trapping of particles by radiation pressure.* Phys Rev Lett, 1970. **24**.

12. Chu, S., et al., *Three-dimensional viscous confinement and cooling of atoms by resonance radiation pressure.* Phys Rev Lett, 1985. **55**(1): p. 48-51.

13. Chu, S., et al., *Experimental observation of optically trapped atoms.* Phys Rev Lett, 1986. **57**(3): p. 314-317.

14. Chu, S., *Nobel Lecture: The manipulation of neutral particles.* Rev Mod Phys, 1998. **70**.

15. Block, S.M., *Making light work with optical tweezers.* Nature, 1992. **360**(6403): p. 493-5.

16. Simpson, N.B., et al., *Optical tweezers with increased axial trapping efficiency.* Journal of Modern Optics, 1998. **45**(9): p. 1943-1949.

17. O'Neil, A.T. and M.J. Padgett, *Axial and lateral trapping efficiency of Laguerre-Gaussian modes in inverted optical tweezers.* Optics Communications, 2001. **193**(1-6): p. 45-50.

18. Neuman, K.C., et al., *Characterization of photodamage to Escherichia coli in optical traps.* Biophys J, 1999. **77**(5): p. 2856-63.

19. Ashkin, A., *Forces of a single-beam gradient laser trap on a dielectric sphere in the ray optics regime.* Biophys J, 1992. **61**(2): p. 569-82.

20. Visscher, K., M.J. Schnitzer, and S.M. Block, *Single kinesin molecules studied with a molecular force clamp.* Nature, 1999. **400**(6740): p. 184-9.

21. Clancy, B.E., et al., *A universal pathway for kinesin stepping.* Nat Struct Mol Biol, 2011. **18**(9): p. 1020-7.

22. Li, Q., S.J. King, and J. Xu, *Native kinesin-1 does not bind preferentially to GTP-tubulin-rich microtubules in vitro.* Cytoskeleton (Hoboken), 2017. **74**(9): p. 356-366.

23. Li, Q., et al., *A fluid membrane enhances the velocity of cargo transport by small teams of kinesin-1.* J Chem Phys, 2018. **148**.

24. Liang, W.H., et al., *Microtubule Defects Influence Kinesin-Based Transport In Vitro.* Biophys J, 2016. **110**(10): p. 2229-40.

25. Li, Q., et al., *Cholesterol influences the effect of tau on membrane-coupled kinesins.* In preparation.

26. Li, Q., et al., *Quantitative Determination of the Probability of Multiple-Motor Transport in Bead-Based Assays.* Biophys J, 2016. **110**(12): p. 2720-2728.

27. Furuta, K., et al., *Measuring collective transport by defined numbers of processive and nonprocessive kinesin motors.* Proc Natl Acad Sci U S A, 2013. **110**(2): p. 501-6.

28. Beeg, J., et al., *Transport of beads by several kinesin motors.* Biophys J, 2008. **94**(2): p. 532-41.

29. Walcott, S., et al., *Smooth muscle heavy meromyosin phosphorylated on one of its two heads supports force and motion.* J Biol Chem, 2009. **284**(27): p. 18244-51.

30. Korn, C.B., et al., *Stochastic simulations of cargo transport by processive molecular motors.* J Chem Phys, 2009. **131**(24): p. 245107.

31. King, S.J. and T.A. Schroer, *Dynactin increases the processivity of the cytoplasmic dynein motor.* Nat Cell Biol, 2000. **2**(1): p. 20-4.

32. Ori-McKenney, K.M., et al., *A cytoplasmic dynein tail mutation impairs motor processivity.* Nat Cell Biol, 2010. **12**(12): p. 1228-34.

33. Jamison, D.K., et al., *Two kinesins transport cargo primarily via the action of one motor: implications for intracellular transport.* Biophys J, 2010. **99**(9): p. 2967-77.

34. Jannasch, A., et al., *Kinesin-8 is a low-force motor protein with a weakly bound slip state.* Biophys J, 2013. **104**(11): p. 2456-64.

35. Nicholas, M.P., L. Rao, and A. Gennerich, *An improved optical tweezers assay for measuring the force generation of single kinesin molecules.* Methods Mol Biol, 2014. **1136**: p. 171-246.

36. Hirokawa, N., et al., *Submolecular domains of bovine brain kinesin identified by electron microscopy and monoclonal antibody decoration.* Cell, 1989. **56**(5): p. 867-78.

37. Scholey, J.M., et al., *Identification of globular mechanochemical heads of kinesin.* Nature, 1989. **338**(6213): p. 355-7.

38. Vallee, R.B., et al., *Microtubule-associated protein 1C from brain is a two-headed cytosolic dynein.* Nature, 1988. **332**(6164): p. 561-3.

39. Sakakibara, H., et al., *Inner-arm dynein c of Chlamydomonas flagella is a single-headed processive motor.* Nature, 1999. **400**(6744): p. 586-90.

40. Klumpp, S. and R. Lipowsky, *Cooperative cargo transport by several molecular motors.* Proc Natl Acad Sci U S A, 2005. **102**(48): p. 17284-9.

41. Xu, J., et al., *Tuning multiple motor travel via single motor velocity.* Traffic, 2012. **13**(9): p. 1198-205.

42. Xu, J., et al., *Interplay between velocity and travel distance of kinesin-based transport in the presence of tau.* Biophys J, 2013. **105**(10): p. L23-5.

43. Norris, S.R., et al., *A method for multiprotein assembly in cells reveals independent action of kinesins in complex.* J Cell Biol, 2014. **207**(3): p. 393-406.

44. Ando, D., et al., *Cooperative protofilament switching emerges from inter-motor interference in multiple-motor transport.* Sci Rep, 2014. **4**: p. 7255.

45. Sloboda, R.D. and J.L. Rosenbaum, *Purification and assay of microtubule-associated proteins (MAPs).* Methods Enzymol, 1982. **85 Pt B**: p. 409-16.

46. Schroer, T.A. and M.P. Sheetz, *Two activators of microtubule-based vesicle transport.* J Cell Biol, 1991. **115**(5): p. 1309-18.

47. Vershinin, M., et al., *Multiple-motor based transport and its regulation by Tau.* Proc Natl Acad Sci U S A, 2007. **104**(1): p. 87-92.

48. Xu, J., et al., *Casein kinase 2 reverses tail-independent inactivation of kinesin-1.* Nat Commun, 2012. **3**: p. 754.

49. Yajima, J., et al., *Direct long-term observation of kinesin processivity at low load.* Curr Biol, 2002. **12**(4): p. 301-6.

50. Driver, J.W., et al., *Productive cooperation among processive motors depends inversely on their mechanochemical efficiency.* Biophys J, 2011. **101**(2): p. 386-95.

51. Jamison, D.K., J.W. Driver, and M.R. Diehl, *Cooperative responses of multiple kinesins to variable and constant loads.* J Biol Chem, 2012. **287**(5): p. 3357-65.

52. Andreasson, J.O., et al., *Examining kinesin processivity within a general gating framework.* Elife, 2015. **4**.

53. Kerssemakers, J., et al., *The distance that kinesin-1 holds its cargo from the microtubule surface measured by fluorescence interference contrast microscopy.* Proc Natl Acad Sci U S A, 2006. **103**(43): p. 15812-7.

54. Kon, T., K. Sutoh, and G. Kurisu, *X-ray structure of a functional full-length dynein motor domain.* Nat Struct Mol Biol, 2011. **18**(6): p. 638-42.

55. Kobayashi, T., et al., *Inhibition of dynein ATPase by vanadate, and its possible use as a probe for the role of dynein in cytoplasmic motility.* Biochem Biophys Res Commun, 1978. **81**(4): p. 1313-8.

56. Firestone, A.J., et al., *Small-molecule inhibitors of the AAA+ ATPase motor cytoplasmic dynein.* Nature, 2012. **484**(7392): p. 125-9.

57. Hendricks, A.G., et al., *Motor coordination via a tug-of-war mechanism drives bidirectional vesicle transport.* Curr Biol, 2010. **20**(8): p. 697-702.

58. Barak, P., et al., *Quantitative optical trapping on single organelles in cell extract.* Nat Methods, 2013. **10**(1): p. 68-70.

59. Chretien, D., et al., *Lattice defects in microtubules: protofilament numbers vary within individual microtubules.* J Cell Biol, 1992. **117**(5): p. 1031-40.

60. Arnal, I. and R.H. Wade, *How does taxol stabilize microtubules?* Curr Biol, 1995. **5**(8): p. 900-8.

61. Vitre, B., et al., *EB1 regulates microtubule dynamics and tubulin sheet closure in vitro.* Nat Cell Biol, 2008. **10**(4): p. 415-21.

62. Schaap, I.A., P.J. de Pablo, and C.F. Schmidt, *Resolving the molecular structure of microtubules under physiological conditions with scanning force microscopy.* Eur Biophys J, 2004. **33**(5): p. 462-7.

63. Schaedel, L., et al., *Microtubules self-repair in response to mechanical stress.* Nat Mater, 2015. **14**(11): p. 1156-63.

64. Shubeita, G.T., et al., *Consequences of motor copy number on the intracellular transport of kinesin-1-driven lipid droplets.* Cell, 2008. **135**(6): p. 1098-107.

65. Kural, C., et al., *Kinesin and dynein move a peroxisome in vivo: a tug-of-war or coordinated movement?* Science, 2005. **308**(5727): p. 1469-72.

66. Conway, L., et al., *Motor transport of self-assembled cargos in crowded environments.* Proc Natl Acad Sci U S A, 2012. **109**(51): p. 20814-9.

67. Helenius, J., et al., *The depolymerizing kinesin MCAK uses lattice diffusion to rapidly target microtubule ends.* Nature, 2006. **441**(7089): p. 115-119.

68. Rogers, A.R., et al., *Negative interference dominates collective transport of kinesin motors in the absence of load.* Phys Chem Chem Phys, 2009. **11**(24): p. 4882-9.

69. Derr, N.D., et al., *Tug-of-war in motor protein ensembles revealed with a programmable DNA origami scaffold.* Science, 2012. **338**(6107): p. 662-5.

70. Miller, R.H. and R.J. Lasek, *Cross-bridges mediate anterograde and retrograde vesicle transport along microtubules in squid axoplasm.* J Cell Biol, 1985. **101**(6): p. 2181-93.

71. Parness, J. and S.B. Horwitz, *Taxol binds to polymerized tubulin in vitro.* J Cell Biol, 1981. **91**(2 Pt 1): p. 479-87.

72. Ray, S., et al., *Kinesin follows the microtubule's protofilament axis.* J Cell Biol, 1993. **121**(5): p. 1083-93.

73. Hyman, A.A., et al., *Structural changes accompanying GTP hydrolysis in microtubules: information from a slowly hydrolyzable analogue guanylyl-(alpha,beta)-methylene-diphosphonate.* J Cell Biol, 1995. **128**(1-2): p. 117-25.

74. Can, S., M.A. Dewitt, and A. Yildiz, *Bidirectional helical motility of cytoplasmic dynein around microtubules.* Elife, 2014. **3**: p. e03205.

75. Nitzsche, B., F. Ruhnow, and S. Diez, *Quantum-dot-assisted characterization of microtubule rotations during cargo transport.* Nat Nanotechnol, 2008. **3**(9): p. 552-6.

76. Fridolfsson, H.N. and D.A. Starr, *Kinesin-1 and dynein at the nuclear envelope mediate the bidirectional migrations of nuclei.* J Cell Biol, 2010. **191**(1): p. 115-28.

77. Narayanareddy, B.R., et al., *A biophysical analysis of mitochondrial movement: differences between transport in neuronal cell bodies versus processes.* Traffic, 2014. **15**(7): p. 762-71.

78. Wilson, M.H. and E.L. Holzbaur, *Nesprins anchor kinesin-1 motors to the nucleus to drive nuclear distribution in muscle cells.* Development, 2015. **142**(1): p. 218-28.

79. Nakata, T., et al., *Preferential binding of a kinesin-1 motor to GTP-tubulin-rich microtubules underlies polarized vesicle transport.* J Cell Biol, 2011. **194**(2): p. 245-55.

80. Vale, R.D., et al., *Tubulin GTP hydrolysis influences the structure, mechanical properties, and kinesin-driven transport of microtubules.* J Biol Chem, 1994. **269**(38): p. 23769-75.

81. Yildiz, A., et al., *Kinesin walks hand-over-hand.* Science, 2004. **303**(5658): p. 676-8.

82. Seitz, A. and T. Surrey, *Processive movement of single kinesins on crowded microtubules visualized using quantum dots.* EMBO J, 2006. **25**(2): p. 267-77.

83. Leduc, C., et al., *Molecular crowding creates traffic jams of kinesin motors on microtubules.* Proc Natl Acad Sci U S A, 2012. **109**(16): p. 6100-5.

84. Davis, L.J., et al., *The importance of lattice defects in katanin-mediated microtubule severing in vitro.* Biophys J, 2002. **82**(6): p. 2916-27.

85. Diaz-Valencia, J.D., et al., *Drosophila katanin-60 depolymerizes and severs at microtubule defects.* Biophys J, 2011. **100**(10): p. 2440-9.

86. Rai, A., et al., *Dynein Clusters into Lipid Microdomains on Phagosomes to Drive Rapid Transport toward Lysosomes.* Cell, 2016. **164**(4): p. 722-34.

87. Weaver, C., et al., *Endogenous GSK-3/shaggy regulates bidirectional axonal transport of the amyloid precursor protein.* Traffic, 2013. **14**(3): p. 295-308.

88. Rai, A.K., et al., *Molecular adaptations allow dynein to generate large collective forces inside cells.* Cell, 2013. **152**(1-2): p. 172-82.

89. Verhey, K.J. and J. Gaertig, *The tubulin code.* Cell Cycle, 2007. **6**(17): p. 2152-2160.

90. Janke, C., *The tubulin code: Molecular components, readout mechanisms, and functions.* J Cell Biol, 2014. **206**(4): p. 461-472.

91. Wang, Z. and M.P. Sheetz, *The C-terminus of tubulin increases cytoplasmic dynein and kinesin processivity.* Biophys J, 2000. **78**(4): p. 1955-64.

92. Cai, D., et al., *Single molecule imaging reveals differences in microtubule track selection between Kinesin motors.* PLoS Biol, 2009. **7**(10): p. e1000216.

93. Uchimura, S., et al., *Key residues on microtubule responsible for activation of kinesin ATPase.* EMBO J, 2010. **29**(7): p. 1167-75.

94. Alper, J.D., et al., *The Motility of Axonemal Dynein Is Regulated by the Tubulin Code.* Biophys J, 2014. **107**(12): p. 2872-2880.

95. Sirajuddin, M., L.M. Rice, and R.D. Vale, *Regulation of microtubule motors by tubulin isotypes and post-translational modifications.* Nature Cell Biology, 2014. **16**(4): p. 335-+.

96. Garnham, C.P., et al., *Multivalent Microtubule Recognition by Tubulin Tyrosine Ligase-like Family Glutamylases.* Cell, 2015. **161**(5): p. 1112-23.

97. Morikawa, M., et al., *X-ray and Cryo-EM structures reveal mutual conformational changes of Kinesin and GTP-state microtubules upon binding.* EMBO J, 2015. **34**(9): p. 1270-1286.

98. McKenney, R.J., et al., *Tyrosination of alpha-tubulin controls the initiation of processive dynein-dynactin motility.* EMBO J, 2016. **35**(11): p. 1175-85.

99. Feizabadi, M.S., et al., *Microtubule C-Terminal Tails Can Change Characteristics of Motor Force Production.* Traffic, 2015. **16**(10): p. 1075-1087.

100. Nirschl, J.J., et al., *alpha-Tubulin Tyrosination and CLIP-170 Phosphorylation Regulate the Initiation of Dynein-Driven Transport in Neurons.* Cell Rep, 2016. **14**(11): p. 2637-52.

101. Hyman, A.A., et al., *Role of GTP hydrolysis in microtubule dynamics: information from a slowly hydrolyzable analogue, GMPCPP.* Mol Biol Cell, 1992. **3**(10): p. 1155-67.

102. Kunwar, A., et al., *Stepping, strain gating, and an unexpected force-velocity curve for multiple-motor-based transport.* Curr Biol, 2008. **18**(16): p. 1173-83.

103. Maurer, S.P., et al., *GTPgammaS microtubules mimic the growing microtubule end structure recognized by end-binding proteins (EBs).* Proc Natl Acad Sci USA, 2011. **108**(10): p. 3988-93.

104. Zhu, Z.Q.C., et al., *Interactions between EB1 and microtubules: Dramatic effect of affinity tags and evidence for cooperative behavior.* J Biol Chem, 2009. **284**(47): p. 32651-32661.

105. Gelles, J., B.J. Schnapp, and M.P. Sheetz, *Tracking kinesin-driven movements with nanometre-scale precision.* Nature, 1988. **331**(6155): p. 450-3.

106. Friedman, D.S. and R.D. Vale, *Single-molecule analysis of kinesin motility reveals regulation by the cargo-binding tail domain.* Nat Cell Biol, 1999. **1**(5): p. 293-7.

107. Coy, D.L., et al., *Kinesin's tail domain is an inhibitory regulator of the motor domain.* Nature Cell Biology, 1999. **1**(5): p. 288-292.

108. Carter, B.C., G.T. Shubeita, and S.P. Gross, *Tracking single particles: a user-friendly quantitative evaluation.* Phys Biol, 2005. **2**(1): p. 60-72.

109. LaPointe, N.E., et al., *Effects of eribulin, vincristine, paclitaxel and ixabepilone on fast axonal transport and kinesin-1 driven microtubule gliding: implications for chemotherapy-induced peripheral neuropathy.* Neurotoxicology, 2013. **37**: p. 231-9.

110. McVicker, D.P., L.R. Chrin, and C.L. Berger, *The nucleotide-binding state of microtubules modulates kinesin processivity and the ability of Tau to inhibit kinesin-mediated transport.* J Biol Chem, 2011. **286**(50): p. 42873-80.

111. Kunwar, A., et al., *Mechanical stochastic tug-of-war models cannot explain bidirectional lipid-droplet transport.* Proc Natl Acad Sci U S A, 2011. **108**(47): p. 18960-5.

112. Huang, T.G. and D.D. Hackney, *Drosophila kinesin minimal motor domain expressed in Escherichia coli. Purification and kinetic characterization.* J Biol Chem, 1994. **269**(23): p. 16493-501.

113. Seeger, M.A. and S.E. Rice, *Microtubule-associated protein-like binding of the kinesin-1 tail to microtubules.* J Biol Chem, 2010. **285**(11): p. 8155-62.

114. Luo, S., N.B. Wehr, and R.L. Levine, *Quantitation of protein on gels and blots by infrared fluorescence of Coomassie blue and Fast Green.* Anal Biochem, 2006. **350**(2): p. 233-8.

115. Wong, Y.L. and S.E. Rice, *Kinesin's light chains inhibit the head- and microtubule-binding activity of its tail.* Proc Natl Acad Sci U S A, 2010. **107**(26): p. 11781-6.

116. Feng, Q., et al., *Motor reattachment kinetics play a dominant role in multimotor-driven cargo transport.* bioRxiv 2017. **180778**.

117. Leduc, C., et al., *Cooperative extraction of membrane nanotubes by molecular motors.* Proc Natl Acad Sci U S A, 2004. **101**(49): p. 17096-101.

118. Herold, C., et al., *Long-range transport of giant vesicles along microtubule networks.* Chemphyschem, 2012. **13**(4): p. 1001-6.

119. McIntosh, B.B., E.L. Holzbaur, and E.M. Ostap, *Control of the initiation and termination of kinesin-1-driven transport by myosin-Ic and nonmuscle tropomyosin.* Curr Biol, 2015. **25**(4): p. 523-9.

120. Grover, R., et al., *Transport efficiency of membrane-anchored kinesin-1 motors depends on motor density and diffusivity.* Proc Natl Acad Sci U S A, 2016. **113**(46): p. E7185-E7193.

121. Pyrpassopoulos, S., H. Shuman, and E.M. Ostap, *Method for Measuring Single-Molecule Adhesion Forces and Attachment Lifetimes of Protein-Membrane Interactions.* Methods Mol Biol, 2013. **1046**: p. 389-403.

122. Galneder, R., et al., *Microelectrophoresis of a bilayer-coated silica bead in an optical trap: application to enzymology.* Biophys J, 2001. **80**(5): p. 2298-309.

123. Neumann, S., T.J. Pucadyil, and S.L. Schmid, *Analyzing membrane remodeling and fission using supported bilayers with excess membrane reservoir.* Nat Protoc, 2013. **8**(1): p. 213-222.

124. Driller-Colangelo, A.R., et al., *Cargo rigidity affects the sensitivity of dynein ensembles to individual motor pausing.* Cytoskeleton, 2016. **73**(12): p. 693-702.

125. Tsuda, Y., et al., *Torsional rigidity of single actin filaments and actin-actin bond breaking force under torsion measured directly by in vitro micromanipulation.* Proc Natl Acad Sci U S A, 1996. **93**(23): p. 12937-42.

126. Popchock, A.R., et al., *The mitotic kinesin-14 KlpA contains a context-dependent directionality switch.* Nat Commun, 2017. **8**: p. 13999.

127. Block, S.M., *Constructing optical tweezers.* Cells: A Laboratory Manual, 1998. **II**(7).

128. Petrov, D.Y., et al., *Studying molecular motor-based cargo transport: What is real and what is noise?* Biophys J, 2007. **92**(8): p. 2953-2963.

129. Kochy, T. and T.M. Bayerl, *Lateral diffusion coefficients of phospholipids in spherical bilayers on a solid support measured by 2H-nuclear-magnetic-resonance relaxation.* Phys Rev E, 1993. **47**(3): p. 2109-2116.

130. Bayerl, T.M. and M. Bloom, *Physical properties of single phospholipid bilayers adsorbed to micro glass beads. A new vesicular model system studied by 2H-nuclear magnetic resonance.* Biophys J, 1990. **58**(2): p. 357-62.

131. Erickson, R.P., et al., *How Molecular Motors Are Arranged on a Cargo Is Important for Vesicular Transport.* Plos Comput Biol, 2011. **7**(5).

132. Zajac, A.L., et al., *Local cytoskeletal and organelle interactions impact molecular-motor- driven early endosomal trafficking.* Curr Biol, 2013. **23**(13): p. 1173-80.

133. Belyy, V., et al., *The mammalian dynein-dynactin complex is a strong opponent to kinesin in a tug-of-war competition.* Nat Cell Biol, 2016. **18**(9): p. 1018-24.

134. Hoeprich, G.J., et al., *Kinesin's neck-linker determines its ability to navigate obstacles on the microtubule surface.* Biophys J, 2014. **106**(8): p. 1691-700.

135. Reddy, B.J.N., et al., *Heterogeneity in kinesin function.* Traffic, 2017. **18**(10): p. 658-671.

136. Uppulury, K., et al., *How the interplay between mechanical and nonmechanical interactions affects multiple kinesin dynamics.* J Phys Chem B, 2012. **116**(30): p. 8846-55.

137. Wood, W.G., et al., *Brain membrane cholesterol domains, aging and amyloid beta-peptides.* Neurobiol Aging, 2002. **23**(5): p. 685-94.

138. Shinitzky, M., *Patterns of lipid changes in membranes of the aged brain.* Gerontology, 1987. **33**(3-4): p. 149-54.

139. Abramov, A.Y., et al., *Membrane cholesterol content plays a key role in the neurotoxicity of beta-amyloid: implications for Alzheimer's disease.* Aging Cell, 2011. **10**(4): p. 595-603.

140. Marquer, C., et al., *Increasing membrane cholesterol of neurons in culture recapitulates Alzheimer's disease early phenotypes.* Mol Neurodegener, 2014. **9**: p. 60.

141. Blocker, A., et al., *Microtubule-associated protein-dependent binding of phagosomes to microtubules.* J Biol Chem, 1996. **271**(7): p. 3803-11.

142. Vieira, O.V., R.J. Botelho, and S. Grinstein, *Phagosome maturation: aging gracefully.* Biochem J, 2002. **366**(Pt 3): p. 689-704.

143. Nelson, S.R., K.M. Trybus, and D.M. Warshaw, *Motor coupling through lipid membranes enhances transport velocities for ensembles of myosin Va.* Proc Natl Acad Sci U S A, 2014. **111**(38): p. E3986-95.

144. Filippov, A., G. Oradd, and G. Lindblom, *The effect of cholesterol on the lateral diffusion of phospholipids in oriented bilayers.* Biophys J, 2003. **84**(5): p. 3079-86.

145. Benda, A., et al., *How to determine diffusion coefficients in planar phospholipid systems by confocal fluorescence correlation spectroscopy.* Langmuir 2003. **19**: p. 4120-4126.

146. Ackmann, M., H. Wiech, and E. Mandelkow, *Nonsaturable binding indicates clustering of tau on the microtubule surface in a paired helical filament-like conformation.* J Biol Chem, 2000. **275**(39): p. 30335-43.

147. Dixit, R., et al., *Differential regulation of dynein and kinesin motor proteins by tau.* Science, 2008. **319**(5866): p. 1086-9.

148. Smith, T.E., et al., *Single-molecule inhibition of human kinesin by adociasulfate-13 and -14 from the sponge Cladocroce aculeata.* Proc Natl Acad Sci U S A, 2013. **110**(47): p. 18880-5.